A NEW METHOD FOR NUCLEAR STRUCTURE MEASUREMENT OF NEUTRON DEFICIENT NUCLEI

By

Ralph Ryan Christopher Clement

A DISSERTATION

Submitted to
Michigan State University
in partial fulfillment of the requirements
for the degree of

DOCTOR OF PHILOSOPHY

Department of Physics and Astronomy

2003

ABSTRACT

A NEW METHOD FOR NUCLEAR STRUCTURE MEASUREMENT OF NEUTRON DEFICIENT NUCLEI

By

Ralph Ryan Christopher Clement

A new method for nuclear structure measurement of neutron deficient nuclei was developed. With the new experimental opportunities offered by the recently completed upgrade to the NSCL a program of measurements of neutron deficient nuclei was started to address current uncertainties in astrophysical reaction rates. In these experiments a new experimental technique was developed using the (p,d) transfer reaction in inverse kinematics. This technique is suitable for studying short lived, $\Delta t < 1\ ns$, excited states that decay by gamma-ray emission and will be presented herein. This technique along with the S800 spectrograph, and the new segmented germanium array (SeGA), were used to study one particular rare isotope of interest, ^{33}Ar. This isotope is a good test of technique and provided the first measurement of the astrophysically important states of interest for calculating the ^{32}Cl(p,γ)^{33}Ar reaction rate. The results of this study yielded the first ^{33}Ar gamma-ray level scheme with observed levels up to 3.819(4) MeV. The precise measurement of the first two excited states allowed for a test of the isobaric multiplet mass equation (IMME). The measurement of the $\frac{5}{2}^+$ state at 3.819(4) MeV provided insight into the dominant contribution to the ^{32}Cl(p,γ)^{33}Ar reaction at rp process temperatures. The details of these measurements and their implications are discussed.

In addition, an improved mass model was developed in order to address uncertainties for heavy, proton rich nuclei. One-proton and two-proton separation energies were calculated for proton rich nuclei in the region A = 41 – 75. The method is based on Skyrme Hartree-Fock calculations of Coulomb displacement energies of mirror nuclei

in combination with the experimental masses of the neutron rich mirror nucleus. The implications for the proton drip line and the astrophysical rp process are discussed. This is done within the framework of a detailed analysis of the sensitivity of rp process calculations in type I X-ray burst models on nuclear masses. The remaining mass uncertainties, in particular for some nuclei with $N = Z$, still lead to large uncertainties in calculations of X-ray burst light curves. A list of nuclei was identified for which improved mass data would be most important.

I dedicate this work to Ruth and Kim for believing in me.

ACKNOWLEDGMENTS

Acknowledgements for a process that has spanned so many years and so much work seems impossible. There are so many people to thank due to the sheer magnitude of this project, which includes three masters degrees, six experiments I ran and/or analyzed, participation in many other experiments, countless tests (both on equipment and in the classroom), eight gas handling systems and associated software, a custom power supply, and this thesis—not to mention "life" was going on this whole time. Hence, I am positive that no matter how big the list and how hardy the thanks, I will leave someone out; or as happens so frequently, not properly assign credit where credit is due. Therefore, before I begin thanks to those people who I will call out by name, please accept my sincerest apologies and heartfelt gratefulness to those that have made this final part of my academic career a success. Let me end this paragraph by giving credit to an organization that taught me discipline, self respect, pride, teamwork, commitment, and the value of hard work. I owe the United States Marine Corps a debt of gratitude I can't put into words. Semper Fidelis.

Figure 1: The Few, The Proud, The Marines!

I would like to begin by thanking the members of my thesis committee: Dr. Brad Sherrill, Dr. Tim Beers, Dr. Thomas Glasmacher, Dr. SD (Bhanu) Mahanti, and Dr. Gary Westfall. I have been very fortunate to have had the opportunity to work with these individuals as they are all fabulous people. I was pressed for time at the very end

and the committee was exceptionally understanding and flexible—thank you! I would also like to thank Dr. Hendrik Schatz, as he definitely belongs in this list. Hendrik, thank you for the extra opportunities and guidance you provided. Finally, I think it would be appropriate to give a special thanks to my advisor, Dr. Brad Sherrill—your stability is amazing.

I would also like to thank my collaborators. Experimental Nuclear Physics is definitely a team sport and I would to thank the following collaborators, in alphabetical order: Dr. Daniel Bazin, Professor Walter Benenson, Professor Alex Brown, Dr. Aurthur Cole, Dr. Barry Davids, Christian Dinca, Michael Famiano, Ron Fox, Nathan Frank, Chris Freigang, Dr. Alexandra Gade, Professor Thomas Glasmacher, Katie Miller, Professor Dave Morrissey, Dr. Wil Mueller, Heather Olliver, Professor Werner Richter, Dr. Peter Santi, Professor Hendrik Schatz, Professor Brad Sherrill, Dr. Mathias Steiner, Dr. Andreas Stolz, Russ Terry, Dr. Alexander Volya, Mark Wallace, John Yurkon, and the rest of the NSCL staff.

I would like to conclude my acknowledgements by thanking those people closest to my heart. I offer special thanks to my friends—you know who you are. I might have wound up in the looney bin if you were not around, and I want to say thank you for keeping me sane! Finally, I would like to thank my family. I started college feeling alone and empty and I finished college because I was loved—thank you all! I must give the lion share of this credit to Kim, my wife. The world is a better place because you love me! I would also like to thank Dave (Dad) and Karen Clement; Louis and Linda Wiederman; Tracey, Logan, and Victoria (Baby) Huffman; Jeff, Sierra, and Austin Wiederman; Maxine Kilkoin (Grandma Florida); Merry (Mom) Porter; Ralph (Grampa) and Ruth (Grandma) Clement, and Thor–I miss you.

Contents

List of Figures

List of Tables

Chapter 1

Nuclear Astrophysics

1.1 Introduction

One of the challenges of modern science is to understand the chemical history of the universe. Meeting this challenge requires a combination of observation, models and input data. The universe began with the creation of a few light elements and stars or other nuclear processes produced all subsequent elements. This thesis addresses methods to obtain the necessary nuclear data for understanding the creation of the elements. The results of this thesis are primarily relevant to understanding the astrophysical *rp* process. The *rp* process contributes energy and nucleosynthesis in hydrogen-rich thermonuclear runaways where the temperatures and densities can support proton captures beyond oxygen [3]. This chapter will serve to provide an astrophysical motivation, by means of a short survey of some of the relevant astrophysics, for the results presented in subsequent chapters.

1.2 Origin of the Elements

The temporal evolution of our universe and its formation is fundamentally linked to nuclear processes. Today, we often model the creation of our universe as a cataclysmic

explosion called the Big Bang. It is out of this violence that creation of the elements begins. In particular, the nature of nuclei and their interactions in explosive stellar environments pose interesting, fundamental and often difficult questions for scientists. It is in thermonuclear run-away scenarios that we seek to discover the origin of many of the elements heavier than lithium.[1] As an example, Fig. 1.1 schematically shows the reaction paths of three of the major isotope production processes overlaid on a chart of the nuclides with theoretically calculated drip lines. The r and rp process, rapid neutron capture and rapid proton capture respectively, occur when conditions allow neutron/proton captures to occur faster than competing disintegration process, such as β-decay, thereby creating a path of increasing A. The s process is the slow neutron capture process, and therefore it tends to follow the line of β stability.

1.2.1 Big Bang Nucleosynthesis

Big bang nucleosynthesis (BBN) is responsible for the creation of the first elements, and although BBN is not the subject of this thesis it serves as a good illustration of the issues of nucleosynthesis. Elements began forming less than one second after the big bang (BB). The nuclei produced by BBN include: neutrons, protons, deuterons, tritons, helium, lithium and beryllium.

Current theoretical modeling of BBN is currently described as undergoing a "precision era. [8]" The theory's single free parameter beyond its assumed physics can be expressed as the primordial baryon-to-photon ratio. The current range [9] for the baryon-to-photon ratio from the recent Wilkinson Microwave Anisotropy Probe (WMAP) results is: $\eta = 6.5^{+0.4}_{-0.3} \times 10^{-10}$. An example of a nuclear reaction network used for these calculations can be seen in Fig. 1.2. As noted in [9], the agreement between BBN calculations and observations is a triumph for the standard big bang

[1] Some nuclei may have been formed beyond lithium prior to the formation of stars. The results of models of this pre-stellar production give results that are orders of magnitude lower than stellar. Therefore, we will ignore those production mechanisms.

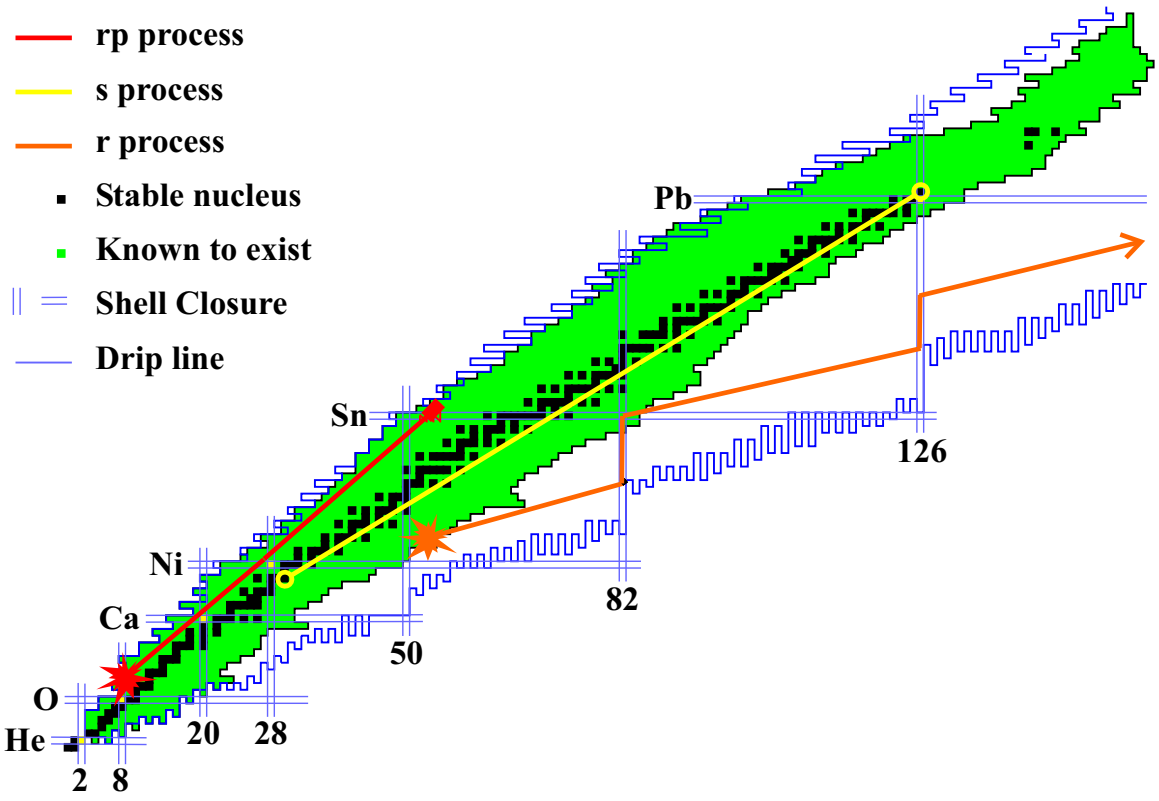

Figure 1.1: Chart of the nuclides showing three of the major astrophysical nuclear synthesis processes. The r and rp processes are explosive processes, while the s process is a stellar burning process. Note: Images in this dissertation are presented in color.

model.

1.2.2 Stars: The Cauldrons of the Cosmos [1]

Since the time of the Big Bang, astrophysical nucleosynthesis has been predominantly the domain of Stars. Stars, in all of the forms we have found them, from our own Sun to space-time singularities created by the final collapse of massive stars known as black holes, are one of nature's richest physics laboratories[2].

During the 1940's, a concept began that envisioned stars as responsible for the continuing synthesis of elements beyond the Big Bang. E.M. Burbidge, G.R. Burbidge, W.A. Fowler and F. Hoyle published the culmination of this visionary idea in 1957

[2]We are loosely including in the class of stellar objects called stars objects which include the "ashes," e.g.: White Dwarfs, Neutron Stars, and Black Holes.

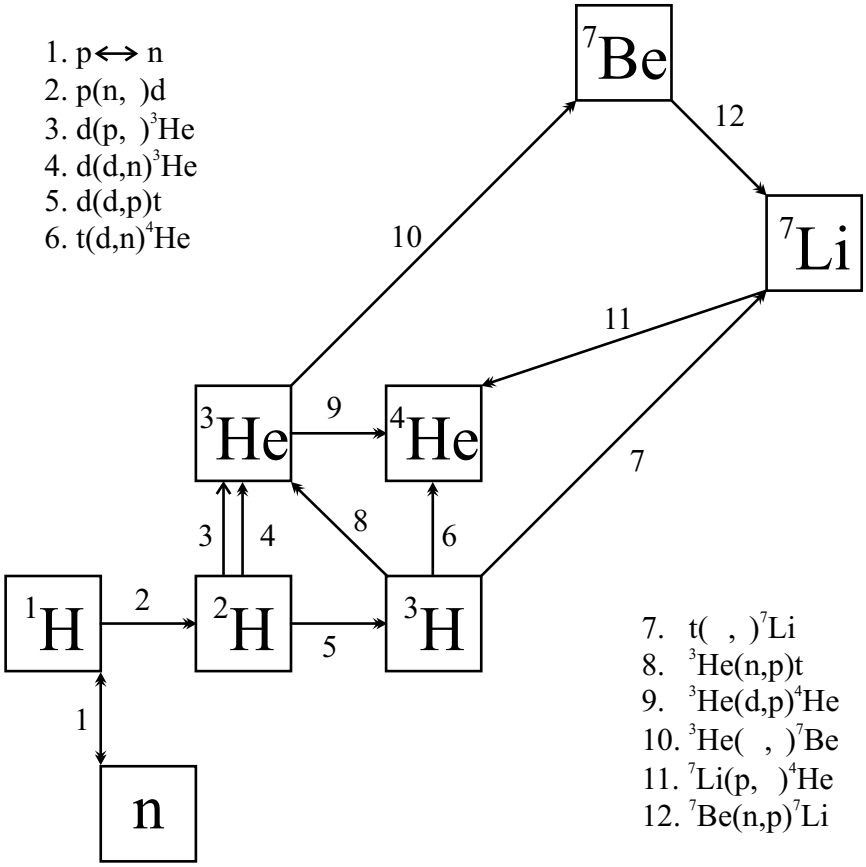

Figure 1.2: The reaction network for standard BBN

with the publication [10] of Synthesis of the Elements in Stars. Independently, the same year, A.G.W. Cameron also announced his work on stellar synthesis. This initial work led to the postulation of many element synthesis scenarios. We will give a rough outline of some of these scenarios in the following subsections[3].

Stellar Burning

The majority of the life of a star is spent burning hydrogen. Stars in this phase of their evolution are called main sequence stars. The two main processes that dominate during this time, depending on the mass of the star, are called the pp chain and the carbon-nitrogen-oxygen (CNO) cycle. Stars of low mass, like our Sun, process

[3]In the mentioned work, [10], several process were defined. These processes, as well as those more recently under investigation, include the α, s, r, x, and p processes.

hydrogen via the pp chain in a predominantly radiative core. Larger mass stars, like Betelgeuse, which have hotter cores process hydrogen via the temperature sensitive CNO cycle in a predominantly convective core. The theoretical mass transition point between the two cycles a star will use to burn hydrogen is at about 1.2 solar masses[4] [11].

An overall contraction phase transitions the star out of the main sequence. It is during this phase that the star changes more rapidly as it nears the end of its evolution. It is during these final set of phases that we find our next major nucleosynthesis process in the s process. The s process is one of the two processes responsible for the majority of elements with a mass number (A) greater than 60. The s process requires silicon (Si) through iron (Fe) group elements as seed nuclei and can synthesize nuclei up to bismuth (Bi). There are two main potential sites for the s process. The first one occurs in the helium burning cores of massive stars ($M_{star} \geq 10 M_{\odot}$). Once a 1-3 $M_{\odot}$ star has come to a phase known as the asymptotic giant branch (AGB) we find our next possible site, which is located in a thermally pulsating helium shell. In either scenario, the defining characteristic of the s process is synthesis of nuclei close to the valley of β stability where neutron capture time scales are longer than corresponding β decays.

The final fate of a star is, in large part, dependent on its mass and mass loss at the surface. We may distinguish roughly two groups during these last phases as well. The cut-off for the transition from one group to the other is $M_{star} \simeq 8 M_{\odot}$[5]. Stars with masses below 8 solar masses will end their lives as a white dwarf star. Stars with 8 solar masses or greater have a different fate - one that we will explore in the next section.

[4]One solar mass is equal to the mass of our own Sun, which is approximately equal to 1.989×10^{33} g and is usually symbolically denoted as $M_{\odot}$.

[5]This result is model dependent and depends on several assumptions including mass loss. Mass loss is important as models with no mass loss give the transition to be $\sim 4 M_{\odot}$.

Explosive Burning

In astrophysical scenarios where thermonuclear runaway can occur we find the last two nucleosynthesis processes we will discuss, the r and rp processes. Examples for sites of thermonuclear explosions, or those with similar extreme physical conditions, include novae, supernovae, accreting neutron stars, neutron star collisions, black hole-neutron star collisions and coalescing black holes.

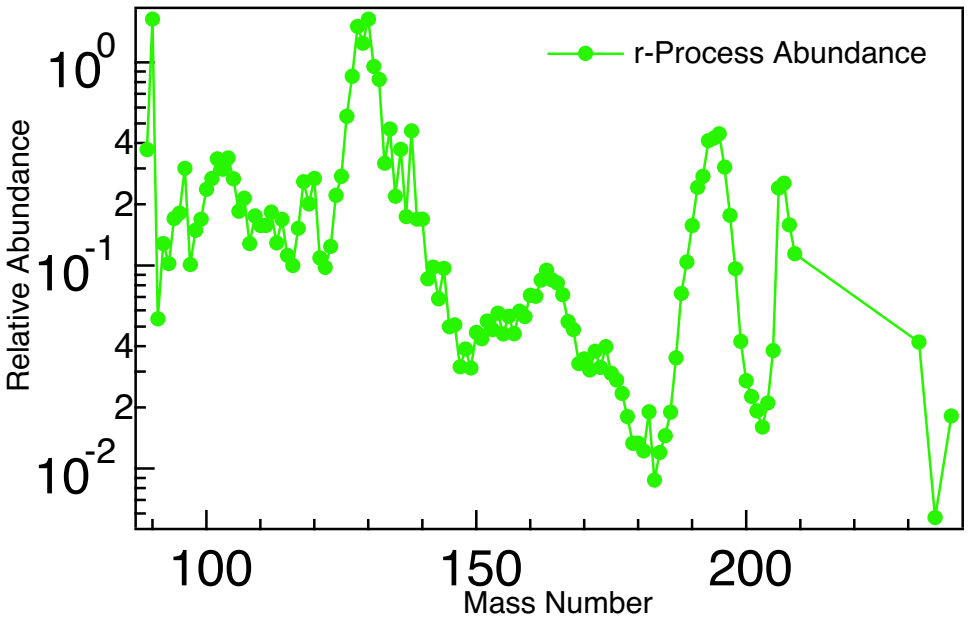

Figure 1.3: Calculated relative r process abundances from Bernd Pfeifer 2002. Mass numbers shown from A=89 to 238.

The defining characteristic, as well as what distinguishes the r process from the s process, is the rate of capture of neutrons in relation to the competing β decay process. In the r process, the rate of neutron captures exceeds the β decay rate so that very neutron rich isotopes may be reached. The astrophysical site of the r process is unknown [12], though it is thought that the r process is responsible for roughly half of all nuclei above the iron group. The nuclei identified as r process nuclei are shown in Fig. 1.3, whereas, for comparison, the abundances from the Sun are shown in Fig. 1.4. r process nuclei include the nucleochronometers ^{232}Th, ^{238}U and ^{235}U. In reference [12], the authors suggest several possible scenarios and group them into three

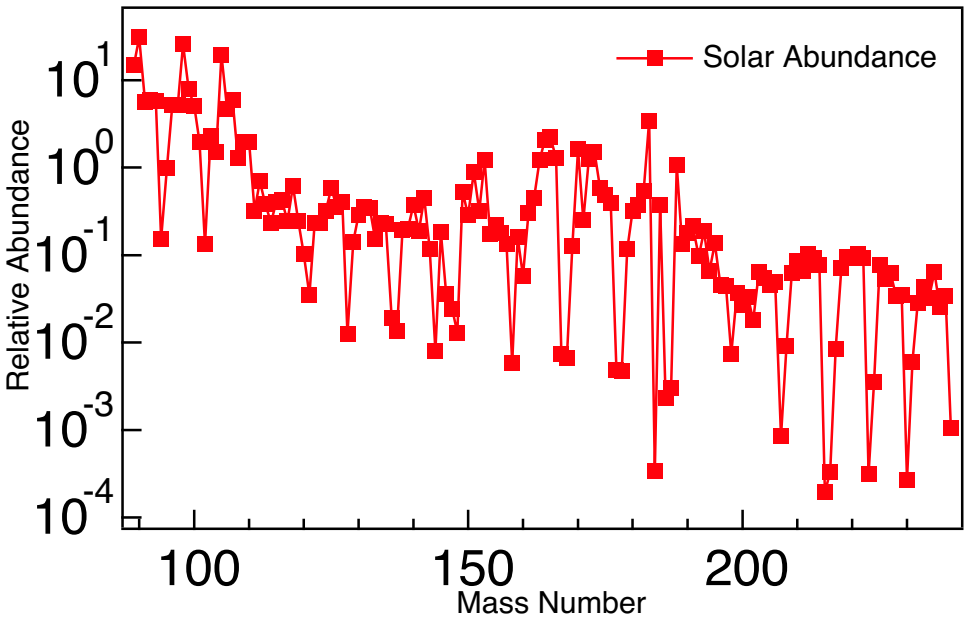

Figure 1.4: Solar abundances from Anders & Grevesse '89 normalized to Si. Mass numbers shown from A=89 to 238.

broad categories. These categories are: Primary, Secondary and Primordial. Primary, or direct, production sites include, but are not limited to, neutron star and neutron star-black hole collisions. Secondary r process sites require seed nuclei from which to proceed. An example of a secondary sites include the helium and carbon zones of stars during a supernovae explosion. Table 1.1 shows the evolutionary stages of a 25 $M_{\odot}$ star ending in a supernovae explosion. Note the changes in the timescales and densities[6] for the various burning scenarios. Finally, primordial r process nucleosynthesis occurs in certain inhomogeneous BBN scenarios.

The rp or rapid proton capture process may be responsible for a significant portion of neutron deficient nuclei from neon thru tellurium. Similar to the r process, the rp process proceeds by capturing new nucleons, in this case protons, faster than the competing β decay can transmute a given isotope, in many cases until the proton drip line is reached. The primary astrophysical site of the rp process is a binary star system, known as an X-ray binary, in which a neutron star accretes material from a

[6]For comparison the density of a Uranium nucleus is approximately equal to 3×10^{14} g/cm^3

Burning Stage	Time Scale	T_9(K)	ρ(g/cm^3)
H	7×10^6 y	0.006	5
He	5×10^5 y	0.23	700
C	600 y	0.93	2×10^5
Ne	1 y	1.7	4×10^6
O	1/2 y	2.3	1×10^7
Si	1 day	4.1	3×10^7
Core Collapse	Seconds	8.1	3×10^9
Core Bounce	Millisec	34.8	3×10^{14}
Explosive	$< 10\ s$	1.2 - 7.0	

Table 1.1: Evolutionary Stages of a 25 Solar Mass Star [1]

non-degenerate companion star. We will begin describing this scenario in more depth in the following sections.

1.3 X-Ray Binaries

1.3.1 Introduction

The class of X-ray binaries includes binary star systems that release X-ray luminosities up to the Eddington limit $\sim 10^{38} \frac{M_{star}}{M_\odot} erg\ s^{-1}$. There are many X-ray binaries known to astronomers since their discovery in 1962 [11]; examples include Sco X-1 and Cen X-3.

The accreting neutron star binary system is one proposed site of the *rp* process, though it is not the only one [13]. A typical X-ray binary is composed of a main sequence star and a 1.4 $M_\odot$, 10 km radius neutron star. The outer layer of the main sequence companion star has crossed an equipotential surface known as the Roche Lobe and has formed what is formally know as a semidetached system. The Roche Lobe is defined as the gravitational equipotential surface that contains the inner Lagrangian point, the point between both stars where a test mass would feel no gravitational force. A two dimensional slice of a semidetached system shows the Roche Lobe contour to have the shape of a "figure 8". A cartoon example of such a

system is shown in Fig. 1.5. The material that has crossed the boundary may now flow toward the neutron star. As our system is comprised of two gravitationally bound stars rotating about the center of mass, the out flowing gas cannot flow directly onto the neutron star surface. Also, as neutron stars frequently have strong magnetic fields, the ionized gas is directed to the magnetic poles from the Alfven radius on. As the material falls inward, at speeds that can approach half the speed of light, the outer atmosphere of the neutron star it becomes hot and dense as potential energy is converted to kinetic and thermal energy. The energy radiation of the matter, which one may roughly view as blackbody radiation, carries away about half of the gravitational energy before it reaches the neutron star surface. It is the luminosity of this accreting matter that gives it its steady state X-ray character. Typical systems for which the rp process is thought to be active are characterized by accretion rates of $10^{-8}/10^{-10} M_{\odot}/yr$, orbital periods of 0.01–100 days and orbital separations of 0.001–1 AU's.

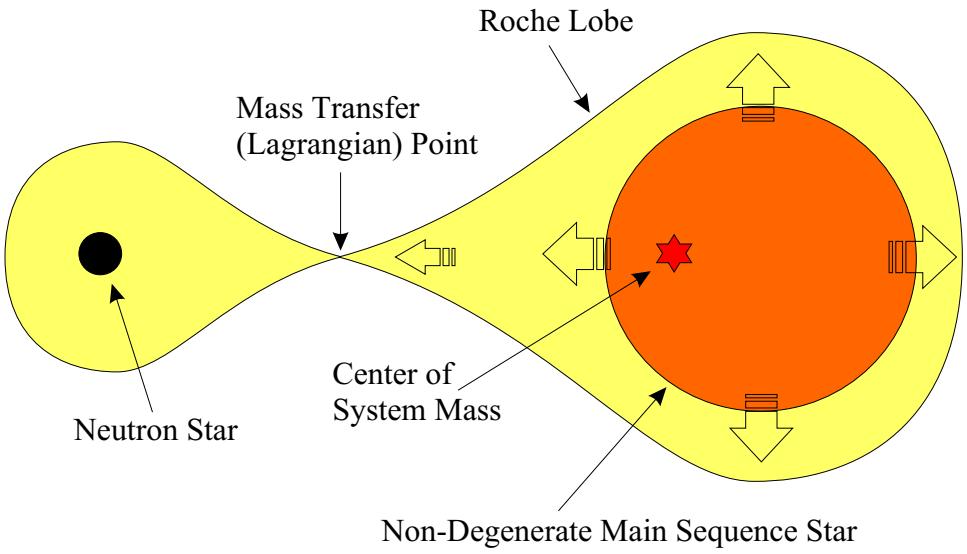

Figure 1.5: One of the ways a star can fill its Roche Lobe is during an expansion phase, denoted by the arrows. Other methods by which stars may have the boundaries of their atmospheres located beyond their Roche Lobe include orbit degradation by mechanisms, which can include tidal friction and/or gravitational radiation.

The evolution of such a system is dependent on several parameters, which include, but are not limited to, the temperature of the neutron star surface, the composition

of the infalling material from the non-degenerate companion star, the rate at which the material accumulates, mass of the neutron star and the crust composition of the neutron star. Due to the extreme conditions with which the accreted nuclei are plunged, we can break out of the stable burning process mentioned above and, under the right conditions, have thermonuclear runaways. One such thermonuclear runaway scenario, i.e. explosive burning, is the *rp* process, which is the subject of the next section.

1.3.2 *rp* process

The defining characteristic of the *rp* process, or rapid proton capture process, is a sequence of proton captures that occur faster than competing β decays. Unless seed nuclei are present, the *rp* process will begin with the break out of the CNO cycle via the reactions $^{15}O(\alpha,\gamma)^{19}Ne$ [14] and $^{18}Ne(\alpha,p)^{21}Na$ at temperatures greater than approximately 0.3 and 0.6 GigaKelvin, respectively, and can continue to the Sn-Sb-Te cycle [15]. An example of the extreme physical conditions present during this process is illustrated in Table 1.2, which only shows two of the possible parameter values during an X-ray burst. Temperature and density are in general related by the system's equation of state (EOS). A detailed discussion of the temperature/density relationship is given in [3]. A typical X-ray burst releases 10^{36}–10^{38} erg/s over a duration of 10–100 s with a reoccurrence of hours to days. Currently there are approximately 230 X-ray binaries known. In addition, there are two types of X-ray bursters observed, Type I and Type II. Type I bursts are the most common and are characterized by the burst energy proportionality with the duration of inactivity preceding the burst. The less common Type II bursts are characterized by the proportionality of the burst energy to the duration of inactivity following the burst.

The observation shown in Fig. 1.6 gives a sense of the observed output and duration of an X-ray burst. The figure shows the sharp rise accompanying the thermonu-

Physical Parameter	Value
Temperature ($[T_9]$=GigaKelvin)	1
Density ($[\rho]$=gm/cm^3)	10^6

Table 1.2: The extreme physical conditions necessary for an *rp* process [3].

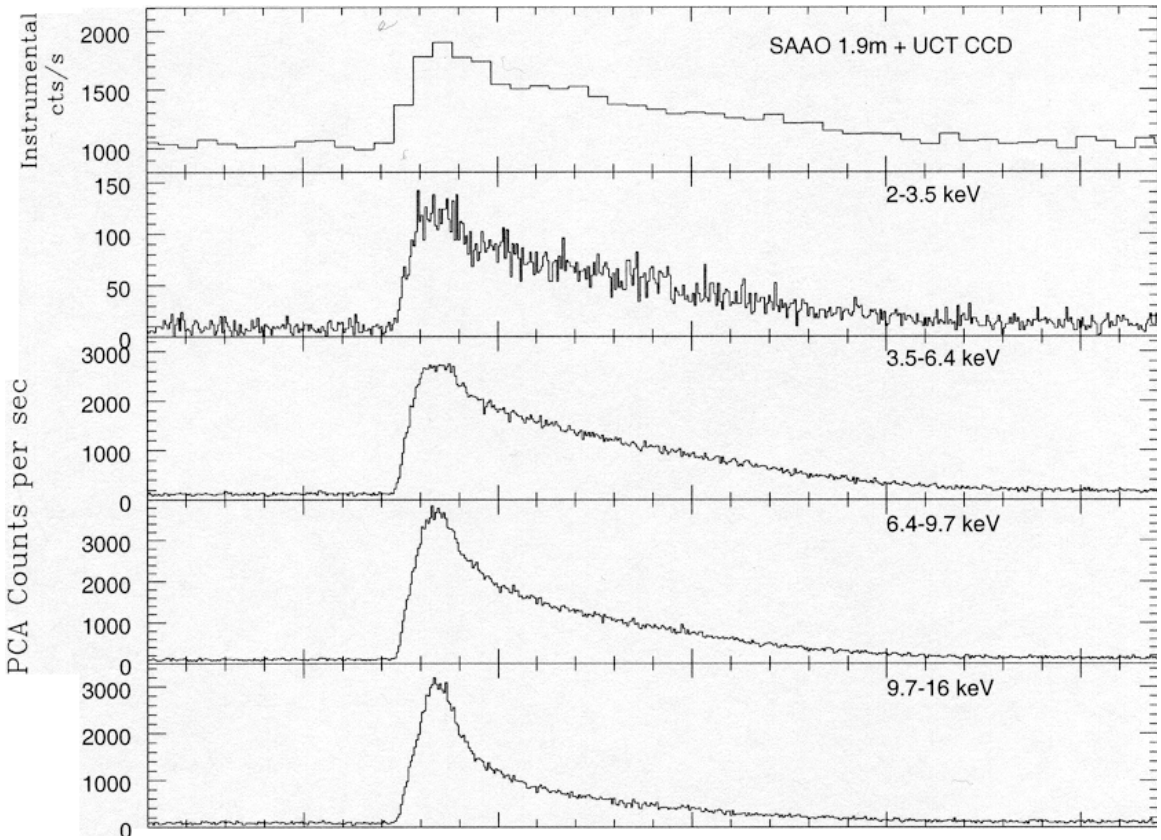

Figure 1.6: X-ray/optical bursts from GS 1826-24 by Kong *et. al.* [2]. The top graph is the optical observation from the SAAO. The next four graphs are X-ray burst profiles taken by RXTE with the proportional counter array (PCA). The system being observed here is thought to contain a 1.4 $M_\odot$ neutron star separated by 2-3 light seconds from a 0.1-1.1 $M_\odot$ companion star with an orbital period of $\sim$ 2.1 h. The ticks on the horizontal axis are in 10 second intervals.

clear runaway along with the long tail as the burst proceeds. The nature of the tail is mainly due to waiting point nuclei beyond Ni. These waiting point nuclei, and their effect on the burst profile is the subject of the next chapter.

Chapter 2

Proton Drip Line Calculations and the rp process

2.1 Overview

Meeting the challenge of understanding rp process nucleosynthesis requires a combination of observation, models and input data. The ability of any model to accurately predict physical phenomena is inherently limited by the quality of the input data. It is also important to understand the impact of input uncertainties on the models. Even small uncertainties may prevent the model from having predictive power. A study of the impact of nuclear physics input data on the rp process within the framework of an accreting neutron star x-ray burst model was carried out. The results of this study, [16], are presented in this chapter.

2.2 Introduction

The masses for the proton-rich nuclei above $A = 60$ have not yet been measured. However, they are important for the astrophysical rapid-proton capture (rp) process [3] which follows a path in nuclei near $N = Z$ for $A = 60 - 100$. The rp process

is the dominant source of energy in type I X-ray bursts and it determines the crust composition of accreting neutron stars [13,15,17–19]. It may also be responsible for the p process nucleosynthesis of a few proton-rich stable nuclei in the $A = 74$–98 mass range. In the absence of experimental masses for the proton-rich nuclei, one often uses the masses based upon the Audi-Wapstra extrapolation (AWE) method [4]. In this thesis the displacement-energy method [20–23] was used to obtain the proton-rich masses, with the Skyrme Hartree-Fock model for the displacement energies. The displacement energy is the difference in the binding energies of mirror nuclei for a given mass A and isospin T:

$$D(A,T) = BE(A,T_z^<) - BE(A,T_z^>), \tag{2.1}$$

where $T = \mid T_z^< \mid = \mid T_z^> \mid$, $BE(A,T_z^<)$ is the binding energy of the proton-rich nucleus and $BE(A,T_z^>)$ is the binding energy of the neutron-rich nucleus. The displacement energy can be much more accurately calculated than the individual BE in a variety of models since it depends mainly on the Coulomb interaction. In particular, the spherical Hartree-Fock model based upon the recent SkX set of Skyrme parameters [24] was used, with the addition of charge-symmetry breaking (CSB), SkX$_{csb}$ [25]. With the addition of CSB, these calculations are able to reproduce the measured displacement energies for all but the lightest nuclei to within an rms deviation of about 100 keV [25]. In the $A = 41 - 75$ mass region, the mass (binding energy) of most of the neutron-rich nuclei are experimentally usually known to within 100 keV or better (the only exception being ^{71}Br for which we use the AWE). Thus, the experimental binding energy for the neutron-rich nucleus $BE(A,T_z^>)_{exp}$ was combined with the Hartree-Fock value for $D(A,T)_{HF}$ to provide an extrapolation for the proton-rich binding energy:

$$BE(A,T_z^<) = D(A,T)_{HF} + BE(A,T_z^>)_{exp}. \tag{2.2}$$

The method is similar to the one used by Ormand [22] for the proton-rich nuclei with $A = 46 - 70$. In [22], the displacement energies are based upon shell-model configuration mixing, which includes Coulomb and CSB interactions with parameters for the single-particle energies and strengths, which are fitted to this mass region. In the present work, which covers the region $A = 41 - 75$, the displacement energies are based upon Skyrme Hartree-Fock calculations with a global set of parameters which are determined from the properties of closed-shell nuclei and nuclear matter. The CSB part of the interaction has one parameter, which was adjusted to reproduce the displacement energies in the $A = 48$ mass region [25].

The displacement energies for all but the lightest nuclei can be reproduced with the constant CSB interaction given in [25], and the same CSB interaction was used for the extrapolations to higher mass discussed here.

The calculations presented here are relevant for the masses of proton-rich nuclei via their connection with their mirror neutron-rich analogues. Improvement upon the masses of nuclei with $N = Z$ was not possible and, as will be discussed, the relatively large errors which remain for the ^{64}Ge and ^{68}Se masses are the dominant uncertainty in the *rp* process calculations.

Details of the Hartree-Fock calculations will be discussed, and a comparison between the calculated and experimental displacement energies for the $A = 41 - 75$ mass region will be made. Then the extrapolations for the proton-rich masses and the associated one- and two-proton separation energies will be presented. The proton drip line, which is established by this extrapolation will be compared to experiment, and the nuclei which will be candidates for one- and two-proton decay will be discussed. Finally, the significance of the new extrapolation for the *rp* process in type I X-ray bursts is explored.

2.3 Displacement-Energy Calculations

The SkX_{csb} interaction is used to carry out Hartree-Fock calculations for all nuclei in the range $Z = 20 - 38$ and $N = 20 - 38$. The binding energies are then combined in pairs to obtain theoretical displacement energies for $A = 41 - 75$ and $T = 1/2$ to $T = 4$:

$$D(A,T)_{HF} = BE(A,T_z^<)_{HF} - BE(A,T_z^>)_{HF}. \tag{2.3}$$

The calculation is similar to those presented in [25], but several refinements are made. The single-particle states in proton-rich nuclei become unbound beyond the proton-drip line. In the nuclei, we consider they are unbound by up to about 2 MeV. Since 2 MeV is small compared to the height of the Coulomb barrier (about 6 MeV at a radius of 7 fm), the states are "quasi-bound" and have a small proton decay width (on the order of keV or smaller). To obtain the quasi-bound wave functions, the HF potential was put in a box with a radius of 20 fm and a depth of 20 MeV. In all cases considered, the dependence of the results on the form of the external potential is negligible as long as the radius is greater than about 10 fm and the potential depth is greater than about 10 MeV.

In [25] the occupation numbers of the spherical valence states were filled sequentially, and in this mass region they always occur in the order $f_{7/2}$, $p_{3/2}$, $f_{5/2}$, $p_{1/2}$ and $g_{9/2}$. This scheme was improved by carrying out an exact pairing (EP) calculation [26] at each stage of the HF iteration. The exact pairing model has recently been discussed in [26]. The EP method uses the single-particle energies from the HF calculation together with a fixed set of $J = 0, T = 1$ two-body matrix elements and gives the orbit occupations and the pairing correlation energy. The orbit occupations are then used together with the HF radial wave functions to calculate the nucleon densities, which go into the Skyrme energy density functional. This procedure is iterated until conver-

gence (about 60 iterations). The pairing is calculated for protons and neutrons with the same set of two-body matrix elements taken from the FPD6 interaction for the pf shell [27] and the Bonn-C renormalized G matrix for the matrix elements involving the $g_{9/2}$ orbit [28]. For those nuclei considered here, the occupation of the $g_{9/2}$ orbit is always small. It is known that deformed components of the 2s-1d-0g shell are essential for the nuclear ground states above $A = 76$, as indicated by the sudden drop in the energy of the 2^+ state from 709 keV in ^{72}Kr to 261 keV in ^{76}Sr [29]. Thus, $A = 76$ was the largest A. In addition, one cannot always use Eq. (2) above $A = 76$ since many of the masses of the neutron-rich nuclei are not known experimentally.

The results obtained are not very sensitive to the strength of the pairing interaction and the associated distribution of the nucleons between the p and f orbits since these orbits have similar rms radii and single-particle Coulomb shifts. For example, a 20 percent change in the strength of the pairing interaction results in displacement energy changes of less than 20 keV. If pairing is removed, the displacement energies can change by up to about 100 keV. Thus, at the level of 100 keV accuracy pairing should be included, but it is not a crucial part of the model.

A final refinement has been to add a Coulomb pairing contribution to the proton-proton $J = 0$ matrix elements. The two-body Coulomb matrix elements were calculated in a harmonic-oscillator basis. The Coulomb pairing was then defined as the difference of the diagonal $J = 0$ matrix elements from the $(2J + 1)$ weighted average (which corresponds to the spherical part of the Coulomb potential, which is in the HF part of the calculation). The Coulomb pairing matrix elements are 50-100 keV.

In Fig. 2.1, the calculated displacement energies (crosses) are shown in comparison with experiment (filled circles) in cases where both proton- and neutron-rich masses have been measured and with the AWE (squares) in cases where the mass of the proton-rich nucleus is based upon the AWE. The corresponding differences between experiment and theory are shown in Fig. 2.2, including the experimental or AWE error

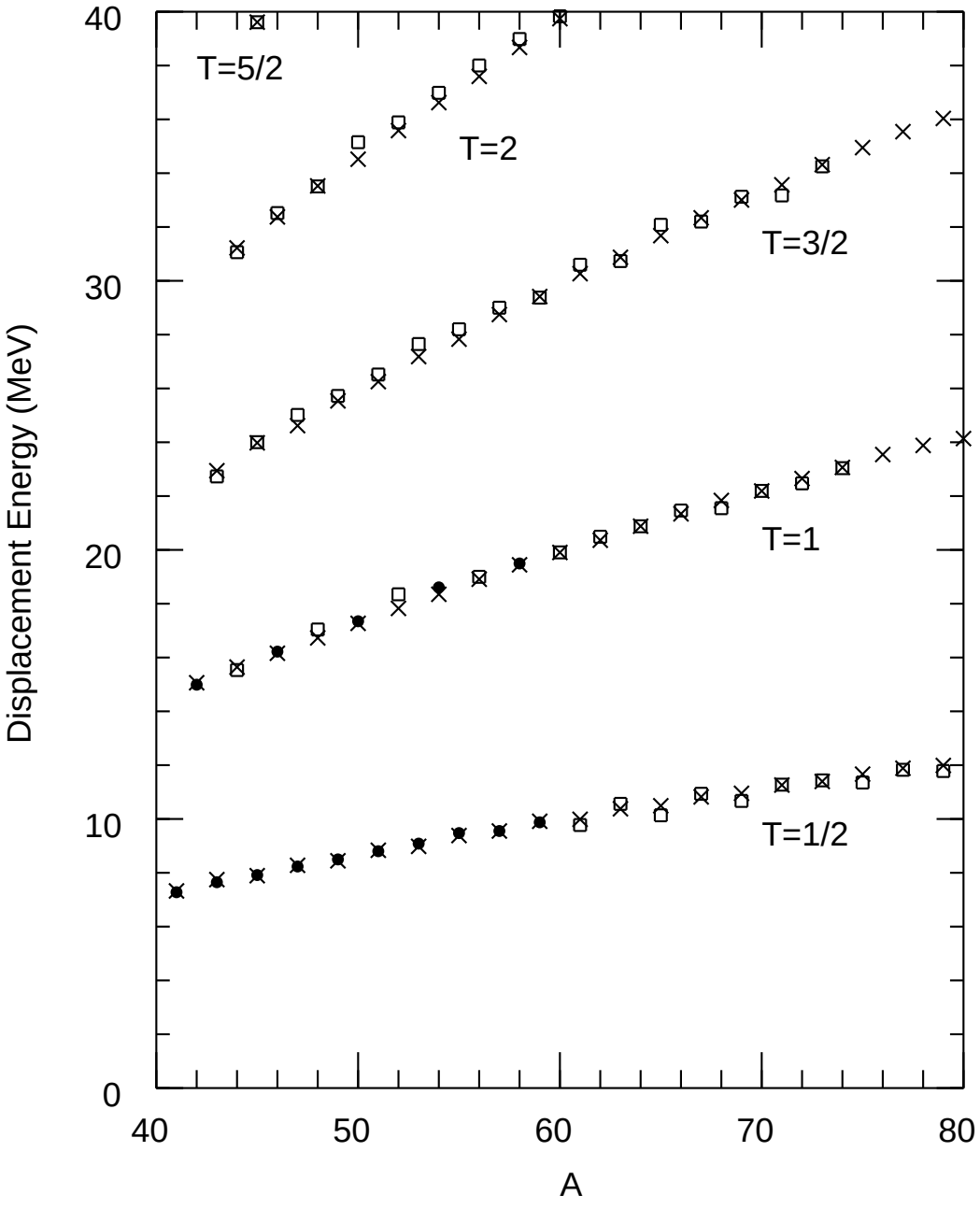

Figure 2.1: Calculated displacement energies (crosses) as a function of mass number. They are compared to experimental data (filled circles) and to values based upon the Audi-Wapstra extrapolations (squares).

bars. It can be seen that when the displacement energy is measured the agreement with the calculation is excellent to within an rms deviation of about 100 keV. The most exceptional deviation is that for $A = 54$ involving the ^{54}Ni-^{54}Fe mirror pair;

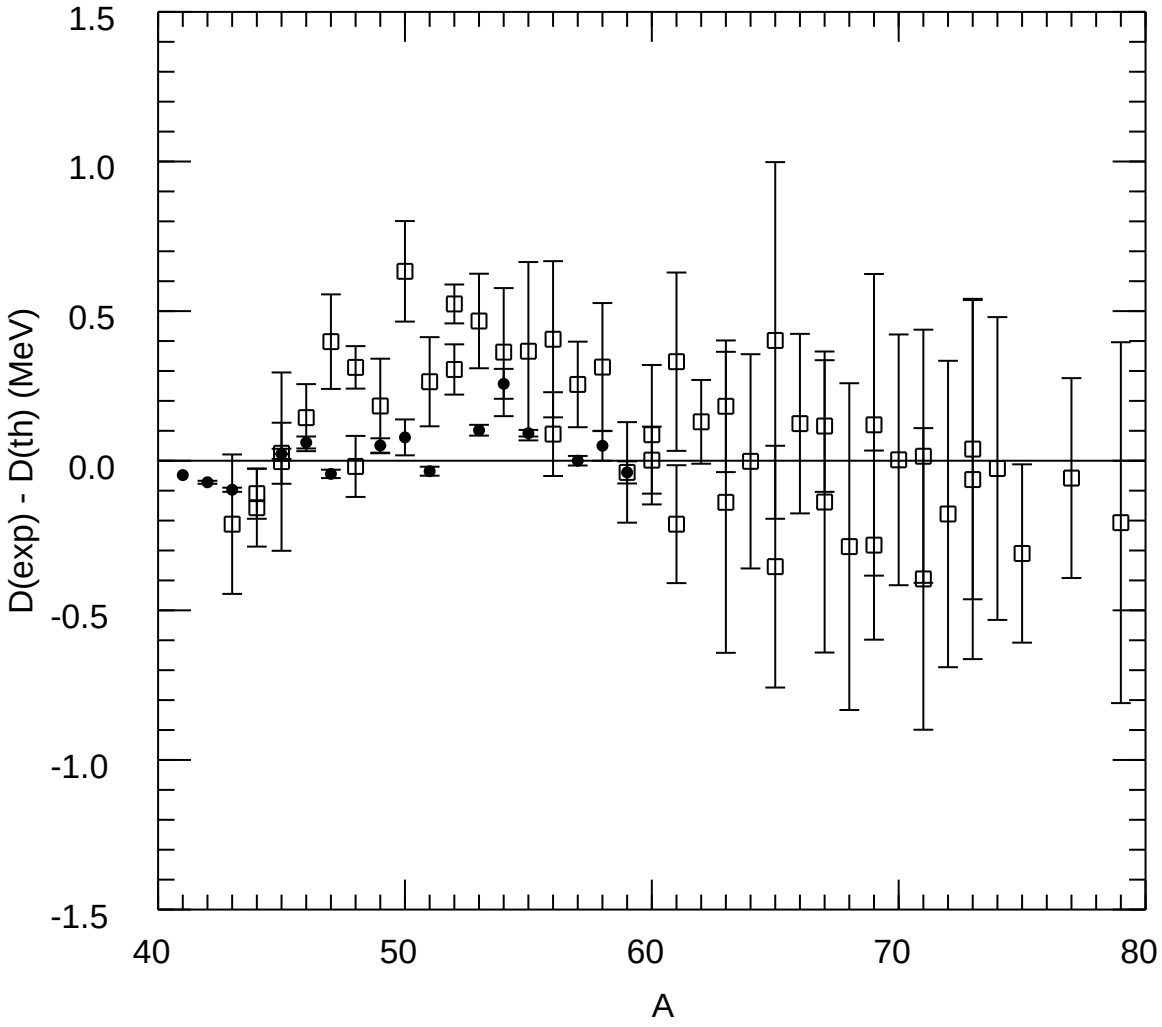

Figure 2.2: The difference between the calculated displacement energies and experiment (filled circles) or values based on the Audi-Wapstra extrapolations (squares).

a confirmation of the experimental mass for ^{54}Ni (which has a 50 keV error) would be worthwhile. The comparison based upon the AWE (squares) shows a much larger deviation with typically up to 500 keV differences, but the AWE error assumed is sometimes (but not always) large enough to account for the spread. The implication of this comparison is that the error in the HF extrapolation of the displacement energies is probably much less than the error in the AWE of the displacement energies. In particular, one notices in Fig. 2.1 in the region $A = 60 - 75$ that the displacement energy based upon the AWE shows a small oscillation, which is not present in the

HF calculation and which is not present in the experimental data for $A < 60$.

2.4 Proton-Rich Masses and Separation Energies

The next step is to use Eq. (2) to calculate the binding energy of the proton-rich nuclei based upon the HF calculation of the displacement energy together with the experimental binding energy of the neutron-rich nucleus [4, 5]. The only neutron-rich nucleus whose mass is not yet experimentally measured is ^{71}Br, for which the AWE value was used. The binding energies for the HF extrapolations for the proton-rich nuclei are given an error based upon the experimental error of the neutron-rich binding energy folded in quadrature with an assumed theoretical error of 100 keV.

The HF extrapolated set of binding energies for proton-rich nuclei, together with the experimental binding energies for nuclei with $N = Z$ and neutron-rich nuclei, provides a complete set of values from which the one- and two-proton separation energies are obtained. The masses for the $N = Z$ nuclei ^{66}As, ^{68}Se, ^{70}Br, are not measured and the AWE value was used. The mass for ^{74}Rb has a relatively large experimental error.

Results for the one- and two-proton separation energies are shown in Fig. 2.3. The first line in each box is the one-proton separation energy (and the associated error) based upon the AWE with the associated error. The second line is the one-proton separation energy based upon the HF extrapolation, and the third line is the two-proton separation energy based upon the HF extrapolation. The error in the separation energies is the error for the binding energies of the parent and daughter nuclei folded in quadrature.

The double line in Fig. 2.3 is the proton-drip line beyond which the one-proton separation energy and/or the two-proton separation energy becomes negative. However, due to the Coulomb barrier, some of the nuclei beyond the proton-drip line may

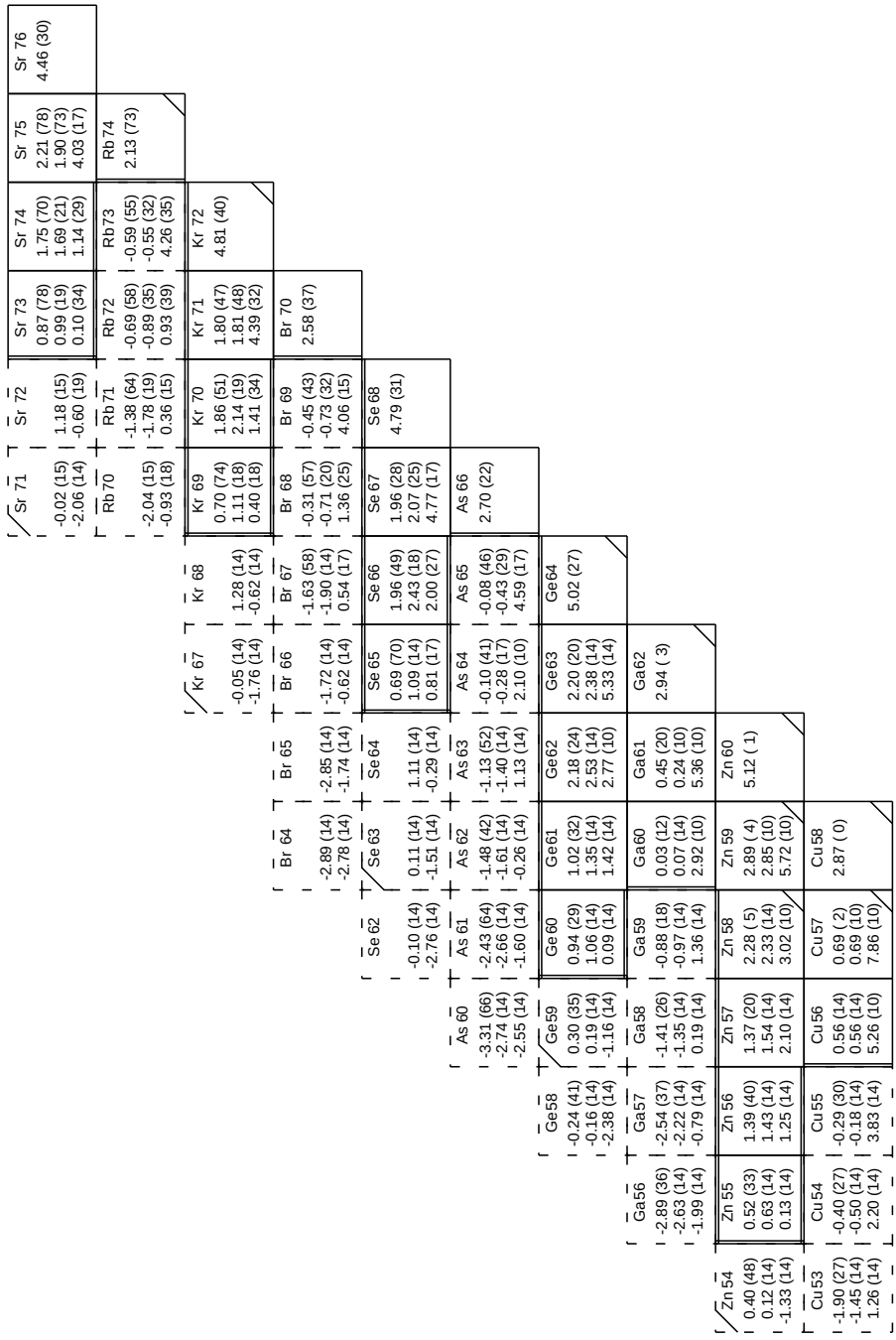

Figure 2.3: A section of the mass chart for $N = Z$ and proton-rich nuclei showing: (line 1): the one-proton separation energy (followed by the associated error) based upon AWE; (line 2): the one-proton separation energy based upon the present HF calculations; and (line 3): the two-proton separation energy based upon the HF calculations. The line in the lower right-hand corner indicates that the mass has been measured for this nucleus. A line in the upper left-hand corner indicates that this nucleus is a candidate for diproton decay.

have lifetimes that are long enough to be able to observe them in radioactive beam experiments. The observation of ^{65}As in the experiment of Blank et al. [30] excludes half-lives which are much shorter than 1 μs, which indicates that it is unbound by less than 400 keV. The identification of ^{65}As as a β-emitter by Winger et al. [31], together with the non-observation of emitted protons by Robertson et al. [32], indicates that it is unbound by less than 250 keV. Both limits are compatible (within error) with the HF results given in Fig. 2.3. The non-observation of ^{69}Br in the radioactive beam experiments of Blank et al. [30] and Pfaff et al. [33] means that its lifetime is less than 24 nsec, which implies that it is proton unbound by more than 500 keV [33]. This is compatible with the HF result shown in Fig. 2.3. The non-observation of ^{73}Rb in the experiments of Mohar et al. [34], Jokinen et al. [35], and Janas et al. [36] gives an upper limit of 30 nsec for the half-life which implies that ^{73}Rb is proton unbound by more than 570 keV, again in agreement (within error) of the present HF result. Thus, all of the current experimental data are consistent with our calculations.

The proton-drip line has not yet been reached for most Z values. Beyond the proton-drip line there are several candidates for nuclei which should be explored for one-proton emission: ^{54}Cu, ^{58}Ge, ^{64}As, ^{68}Br, ^{69}Br, ^{72}Rb and ^{73}Rb. The most promising candidates for the illusive diproton emission (in addition to ^{48}Ni [20, 22]) are ^{64}Zn, ^{59}Ge, ^{63}Se, ^{67}Kr and ^{71}Sr. Estimated lifetime ranges for these diproton decays are given by Ormand [22].

2.5 Implications for the rp process

The rp process beyond Ni plays a critical role during hydrogen burning at high temperatures and densities on the surface of accreting neutron stars in X-ray bursters and X-ray pulsars [13, 15, 17–19]. Nuclear masses are among the most important input parameters in rp process calculations, as they sensitively determine the balance

between proton capture and the inverse process, (γ,p) photodisintegration. It is this (γ,p) photodisintegration that prevents the *rp* process from continuing via proton captures once a nucleus close to the proton drip line is reached. This nucleus then becomes a "waiting point" as the *rp* process has to proceed at least, in part, via the slow β^+ decay. The effective lifetime of the waiting points in the *rp* process determines the overall processing time scale, energy generation and the final abundance distribution. At a waiting point nucleus (Z,N), a local (p,γ)-(γ,p) equilibrium is established with the following isotones (Z+1,N), (Z+2,N). The effective proton capture flow destroying waiting point nuclei and reducing their lifetime is then governed by the Saha equation and the rate of the reaction leading out of the equilibrium. Because of the odd-even structure of the proton drip line two cases have to be distinguished [13]. For temperatures below $\approx 1.4\ GK$, equilibrium is only established with the following isotone (Z+1,N). In this case, the destruction rate of the waiting point nucleus via proton captures $\lambda_{(Z,N)(p,\gamma)}$ is determined by the Saha equation and the proton capture rate on the following isotone (Z+1,N). The total destruction rate of the waiting point nucleus (Z,N) is then given by the sum of proton capture and β decay rates:

$$\lambda = \lambda_\beta + Y_p^2 \rho^2 N_A^2 \left(\frac{2\pi\hbar^2}{\mu_{(Z,N)} kT}\right)^{3/2} \frac{G_{(Z+1,N)}(T)}{(2J_{\mathrm{p}}+1) G_{(Z,N)}(T)} \times \exp\left(\frac{Q_{(Z,N)(p,\gamma)}}{kT}\right) < \sigma v >_{(Z+1,N)(p,\gamma)} \tag{2.4}$$

where, λ_β is the β decay rate of nucleus (Z,N), Y_p the hydrogen abundance, ρ the mass density, J_p the proton spin, $G_{(Z,N)}$ the partition function of nucleus (Z,N), T the temperature, $\mu_{(Z,N)}$ the reduced mass of nucleus (Z,N) plus proton, $Q_{(Z,N)(p,\gamma)}$ the proton capture Q-value of the waiting point nucleus, and $< \sigma v >_{(Z+1,N)(p,\gamma)}$ the proton capture rate on the nucleus (Z+1,N). For higher temperatures, local equilibrium is maintained between the waiting point nucleus (Z,N) and the next two following isotones (Z+1,N) and (Z+2,N). In this case, $\lambda_{(Z,N)(p,\gamma)}$ is given by the Saha equation

and the β decay rate of the final nucleus $\lambda_{(Z+2,N)\beta}$, and the total destruction rate λ of the waiting point nucleus becomes:

$$\lambda = \lambda_\beta + Y_p^2 \rho^2 N_A^2 \left(\frac{2\pi\hbar^2}{kT}\right)^3 \mu_{(Z,N)}^{-3/2} \mu_{(Z+1,N)}^{-3/2} \frac{G_{(Z+2,N)}(T)}{(2J_\mathrm{p}+1)^2 G_{(Z,N)}(T)} \times \exp\left(\frac{Q_{(Z,N)(2p,\gamma)}}{kT}\right) \lambda_{(Z+2,N)\beta} \qquad (2.5)$$

In both cases, the destruction rate of a waiting point nucleus depends exponentially either on its one-proton capture Q-value $Q_{(Z,N)(p,\gamma)}$ or two-proton capture Q-value $Q_{(Z,N)(2p,\gamma)}$. Nuclear masses therefore play a critical role in determining the *rp* process waiting points and their effective lifetimes.

It has been shown before that the most critical waiting point nuclei for the *rp* process beyond Ni are ^{64}Ge, ^{68}Se and ^{72}Kr [13]. With the exception of ^{56}Ni and ^{60}Zn, these nuclei are by far the longest-lived isotopes in the *rp* process path. The reason for these three nuclei being the most critical ones is that with increasing charge number the $N = Z$ line moves closer to the proton drip line and away from stability. Therefore, proton capture Q-values on even-even $N = Z$ nuclei, which are favored in the *rp* process because of the odd-even structure of the proton drip line, decrease with increasing charge number, while the β decay Q-values become larger. ^{64}Ge, ^{68}Se and ^{72}Kr happen to be located in the "middle", where proton capture Q-values are already low enough to suppress proton captures and allow β decay to compete, but at the same time β decay Q-values are still small enough for half-lives to be long compared to *rp* process time scales. The critical question is to what degree proton captures can reduce the long β decay lifetimes of ^{64}Ge (63.7 s half-life), ^{68}Se (35.5 s half-life) and ^{72}Kr (17.2 s half-life). As Eqs. 2.4 and 2.5 show, the answer depends mainly on the one- and two-proton capture Q-values. Unfortunately, experimental data doesn't exist for the relevant Q-values. The only experimental information available are upper limits of the one-proton capture Q-values of ^{68}Se and ^{72}Kr from the non-observation of

^{69}Br [4,4] and ^{73}Rb [4,27,35], and the lower limits on the one-proton capture Q-value on ^{65}As from its identification as a β-emitter in radioactive beam experiments (see Sec. 2.4). While these data provide some constraints, accurate Q-values are needed for the calculations and have to be predicted by theory. The new masses calculated in this thesis cover exactly this critical mass range, and provide improved predictions for all the relevant Q-values in the $A = 64$–72 mass region (see Fig. 2.3). As discussed in Sec. 2.4, all of our new predictions are compatible with the existing experimental limits.

To explore the impact of the new mass predictions on *rp* process models, calculations were performed with a 1-D, one zone X-ray burst model [15, 37]. Ignition conditions are based on a mass accretion rate of 0.1 times the Eddington accretion rate, an internal heat flux from the neutron star surface of 0.15 $MeV/nucleon$, an accreted matter metallicity of 10^{-3} and a neutron star with 1.4 solar masses and 10 km radius.

In principle, proton separation energies can influence the reaction flow in two ways. First, they affect the forward to reverse rate ratios for proton capture reactions and the local (p,γ)-(γ,p) equilibria through the $\exp(Q/kT)$ term in the Saha equation (in Eqs. 2.4 and 2.5). This leads to an exponential mass dependence of the waiting point lifetimes. Second, theoretical predictions of reaction rates $< \sigma v >$ (in Eq. 2.4) depend also on the adopted Q-values. In this work both effects were taken into account. To explore the impact of Q-value uncertainties on proton capture reaction rate calculations we use the statistical model code SMOKER [13]. Even though the nuclei in question are close to the proton drip line, a statistical approach is justified in most cases because reaction rates tend to become important only for larger Q-values when a local (p,γ)-(γ,p) equilibrium cannot be established. Then the level density tends to be sufficient for the statistical model approach. Based on the new reaction rates we used our new Q-values to recalculate (γ,p) photodisintegration rates via detailed

balance as discussed in [13].

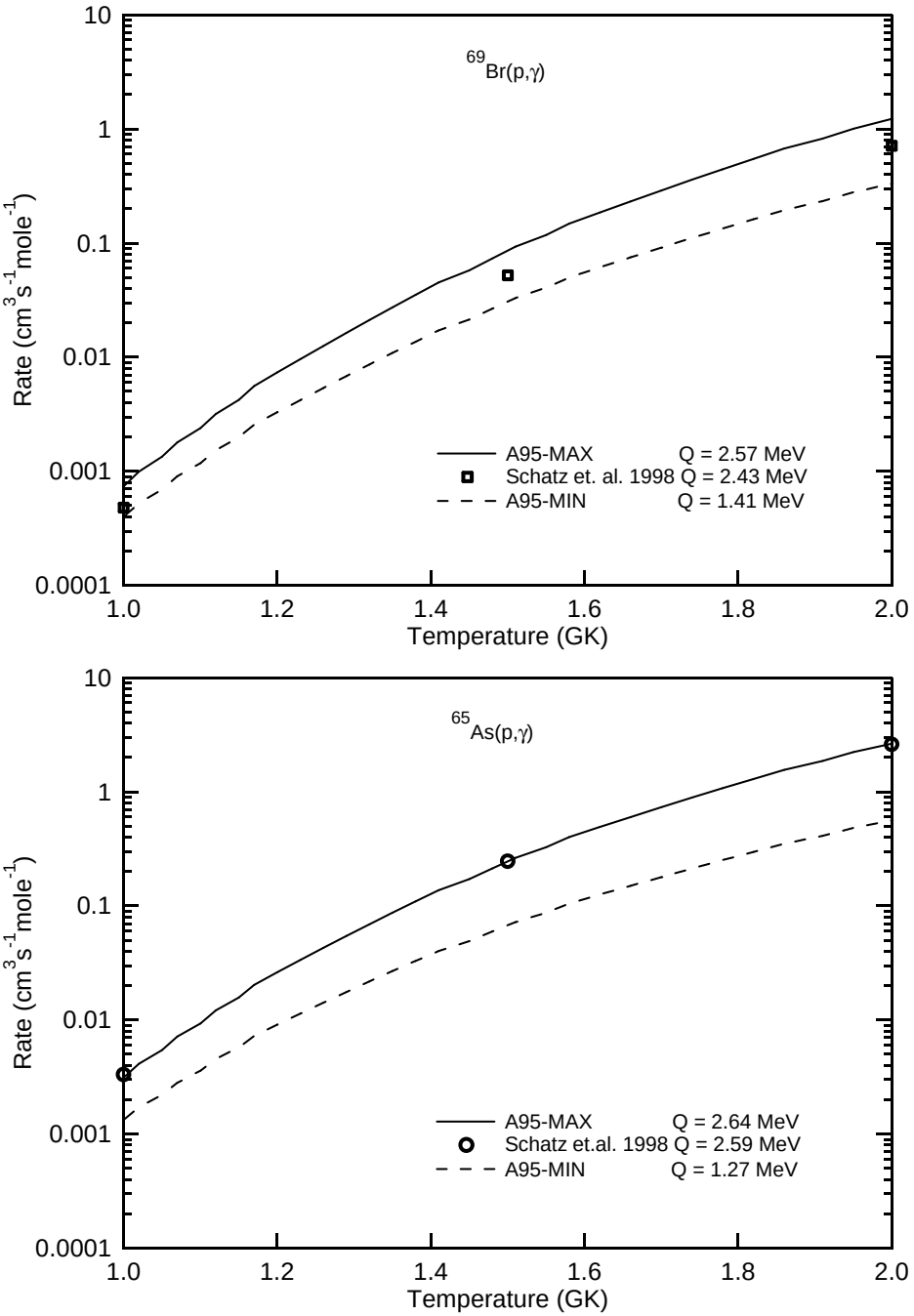

Figure 2.4: The calculated $X(p,\gamma)$ rates for $X =^{65}$As and $X =^{69}$Br with associated Q-values shown in the legend. The astrophysical reaction rates were calculated with the statistical model code SMOKER.

For the relevant temperature range between 1–2 GK, our new proton capture reaction rates vary in most cases not more than a factor of two within the explored mass

uncertainties. Exceptions among the relevant reaction rates are the proton capture rates on ^{65,66}As, ^{69,70}Br and ^{73,74}Rb. These rates show a somewhat stronger variation of typically a factor of 4 – 6 as the associated proton capture Q-values are particularly uncertain. Fig. 2.4 shows two examples for the Q-value dependence of statistical model reaction rates. Generally, a larger Q-value leads to larger rates, as the higher excitation energy of the compound nucleus opens up more possibilities for its decay. For reference, Fig. 2.4 also shows the rates listed in [13], which had been calculated using Q-values from the Finite Range Droplet Mass model (FRDM1992) [38].

To disentangle the different effects of mass uncertainties quantitatively, we performed test calculations in which changes in masses were only taken into account in the calculation of the (γ,p) photodisintegration rates, while the proton capture rates were kept the same. These test calculations lead to very similar luminosity and burst time scale variations as presented in this work. Discrepancies were at most 8% in the luminosity and 0.1% in the burst timescale. This can be understood from Eq. 2.4 and 2.5. For example, a change of 1.37 MeV in the proton capture Q-value changes the ^{65}As reaction rate and therefore the lifetime of the ^{64}Ge waiting point nucleus by a factor of 3–4 (see Fig. 2.4 and Eq. 2.4). However, the same 1.37 MeV Q-value change in the $\exp(Q/kT)$ term in Eq. 2.5 would result in a lifetime change of 6 orders of magnitude (for a typical $kT = 100\ keV$). Therefore, we concluded that the impact of mass uncertainties on rp process calculations through changes in theoretical reaction rate calculations within the statistical model is much smaller than the impact through changes in (p,γ)/(γ,p) reaction rate ratios.

The following calculations were performed with different assumptions on masses beyond the $N = Z$ line from Z = 30-38: SkX based on the mass predictions of this work, SkX-MIN with all proton capture Q-values set to the lowest value, and SkX-MAX with all proton capture Q-values set to the highest values within the error bars of our binding energy predictions. A similar set of calculations has been performed

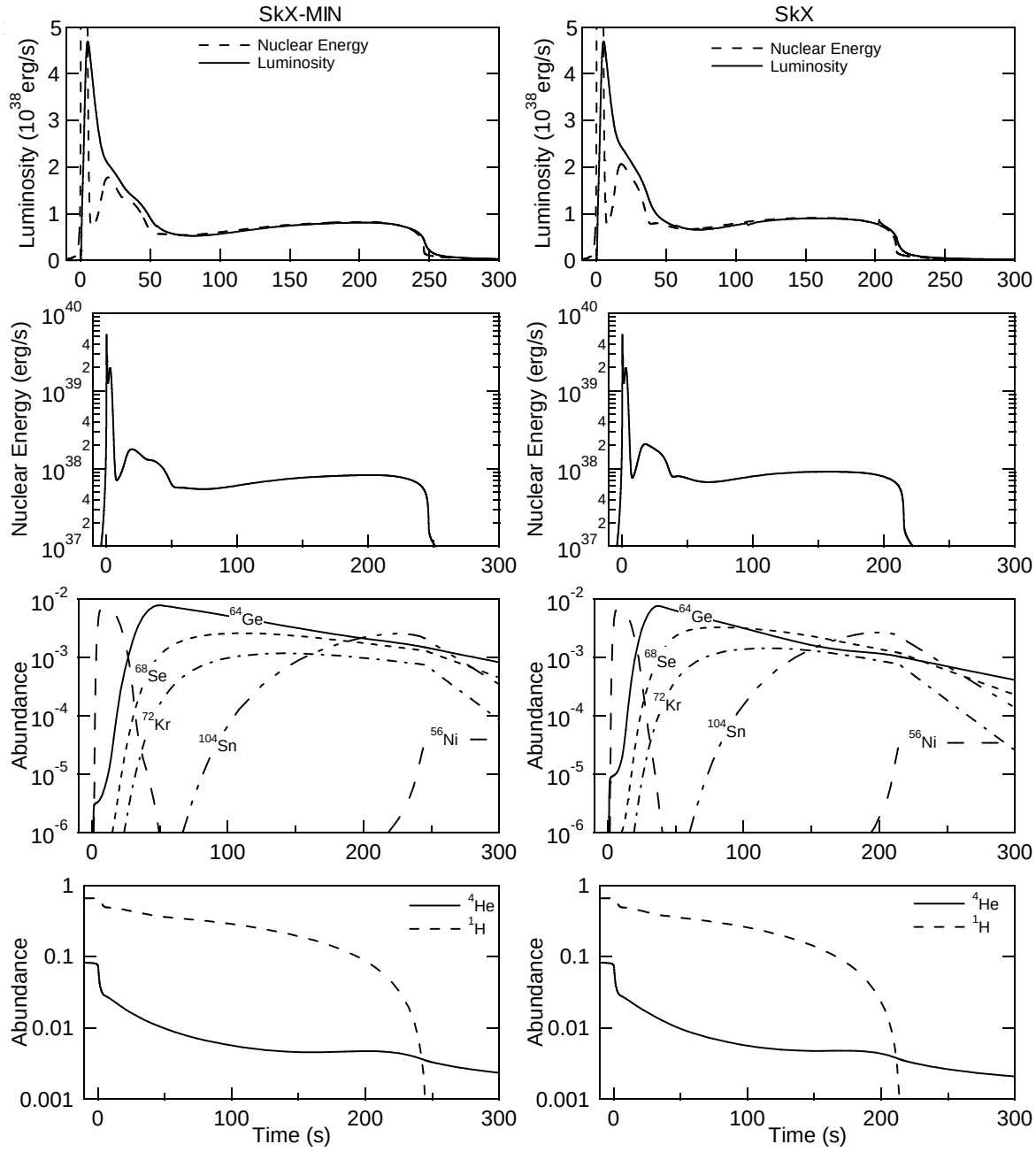

Figure 2.5: Luminosity, nuclear energy generation rate, and the abundances of hydrogen, helium, and the critical waiting point nuclei as functions of time as predicted by our X-ray burst model for different sets of proton capture Q-values. Shown are results for the sets SkX-MIN and SkX, for the smallest and the recommended proton capture Q-values within the error bars of the mass predictions of this work. The ^{104}Sn abundance indicates the operation of the SnSbTe cycle. Also, for comparison, the nuclear energy generation rate is shown as a dashed line together with luminosity, though it is off the scale shown during the peak of the burst. The mass of the accreted layer is 5.0×10^{21} g.

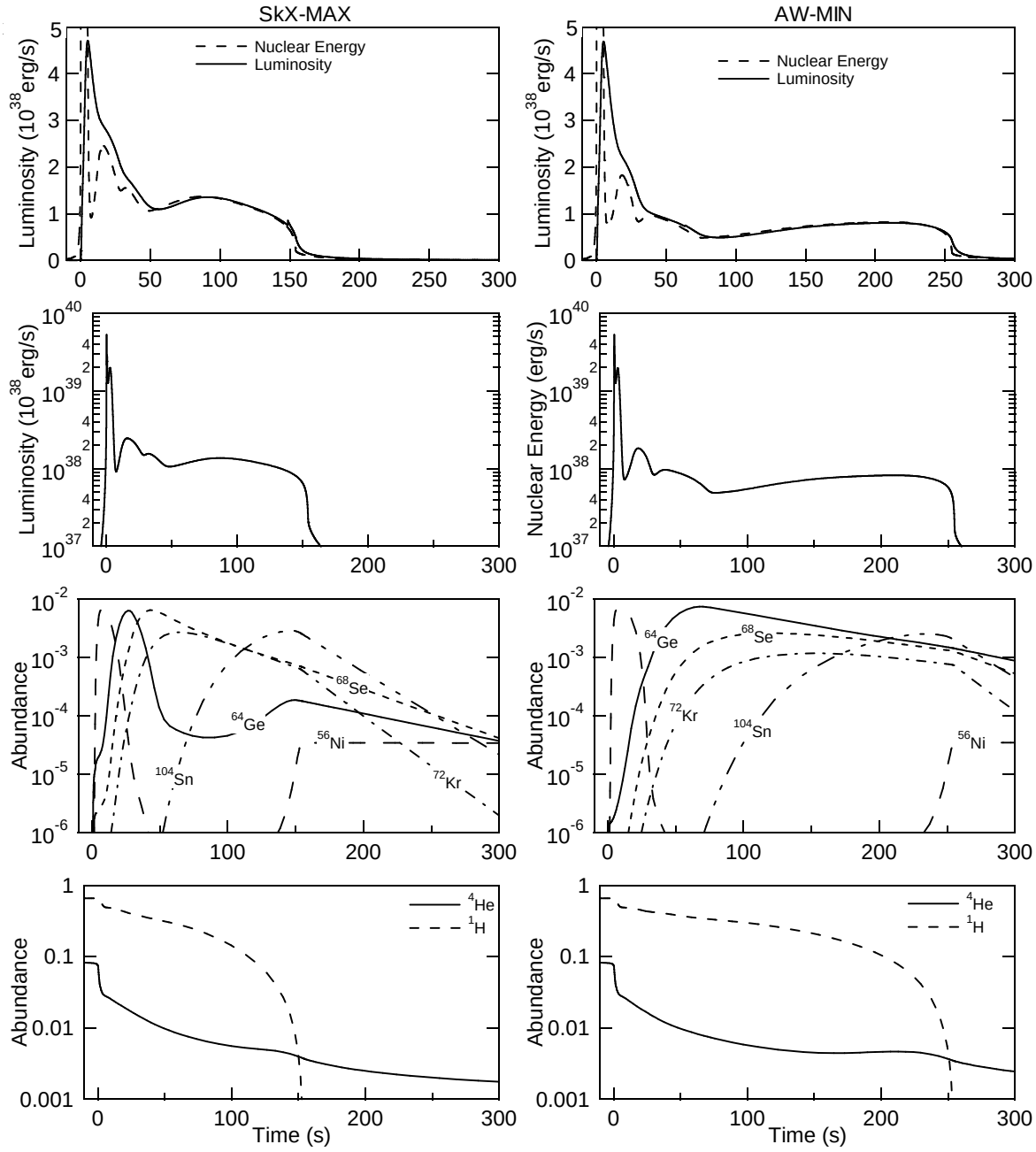

Figure 2.6: Luminosity, nuclear energy generation rate, and the abundances of hydrogen, helium, and the critical waiting point nuclei as functions of time as predicted by our X-ray burst model for different sets of proton capture Q-values. Shown are results for the sets SkX-MAX for the largest proton capture Q-values within the error bars of the mass predictions of this work and the corresponding series is shown for the Audi & Wapstra 1995 mass evaluation min (AW-MIN). The ^{104}Sn abundance indicates the operation of the SnSbTe cycle. Also, for comparison, the nuclear energy generation rate is shown as a dashed line together with luminosity, though it is off the scale shown during the peak of the burst. The mass of the accreted layer is 5.0×10^{21} g.

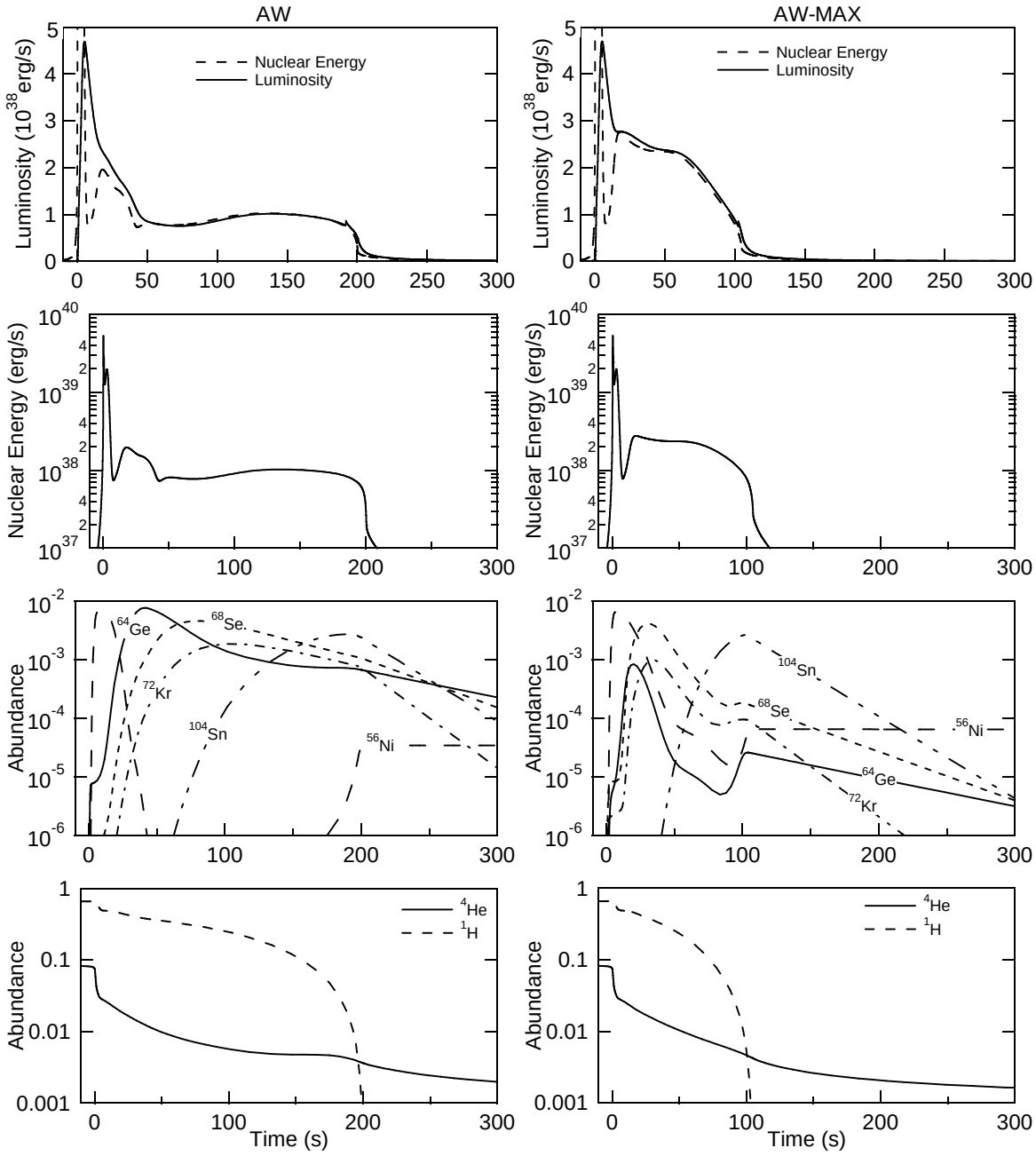

Figure 2.7: Luminosity, nuclear energy generation rate, and the abundances of hydrogen, helium, and the critical waiting point nuclei as functions of time as predicted by our X-ray burst model for different sets of proton capture Q-values. Shown are results for the Audi & Wapstra 1995 mass evaluation recommended and max (AW and AW-MAX). The ^{104}Sn abundance indicates the operation of the SnSbTe cycle. Also, for comparison, the nuclear energy generation rate is shown as a dashed line together with luminosity, though it is off the scale shown during the peak of the burst. The mass of the accreted layer is 5.0×10^{21} g.

for the mass extrapolations of Audi and Wapstra 1995 [4] (AW95) and are labeled AW, AW-MIN, and AW-MAX. Figs. 2.5, 2.6 and 2.7 show the X-ray burst light curve, the nuclear energy generation rate, the abundances of the most important waiting point nuclei and the hydrogen and helium abundances as a function of time for all calculations. As an example, Fig. 2.8 shows the time integrated reaction flow corresponding to the SkX calculation.

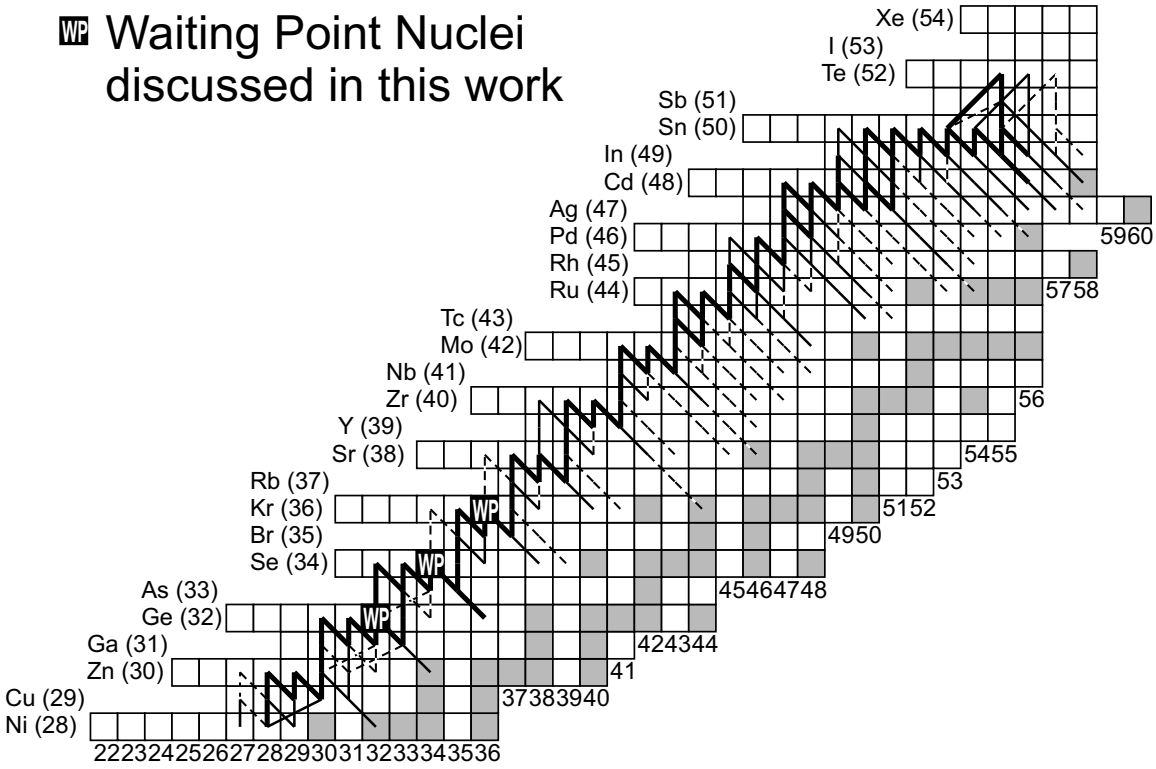

Figure 2.8: The time integrated reaction flow beyond Ni during an X-ray burst calculated on the basis of our new mass predictions. Shown are flows of more than 10% (thick solid line), 1%-10% (thin solid line), and 0.1%-10% (dashed line) of the flow through the 3α reaction. The key waiting points discussed in this work are marked as well.

While the αp and *rp* processes below ^{56}Ni are responsible for the rapid luminosity rise at the beginning of the burst, processing through the slow waiting points ^{64}Ge, ^{68}Se, ^{72}Kr and the operation of the SnSbTe cycle (indicated by the ^{104}Sn abundance) lead to an extended burst tail. The *rp* process from ^{56}Ni to ^{64}Ge, and the slowdown at ^{64}Ge lead to a pronounced peak in the energy generation rate around 50s after

burst maximum. In principle the other waiting points have a similar effect, but the corresponding peaks in the energy production are much wider and therefore not noticeable.

Fig. 2.9 compares X-ray burst light curves for different assumptions on nuclear masses. Generally, lower proton capture Q-values enhance photodisintegration and favor the waiting point nuclei in local equilibria. Both effects lead to a slower reaction flow and, therefore, to less luminous but longer lasting burst tails. Even though the uncertainties in our new mass predictions are significantly smaller than in AW95, they still allow for a burst length variation from $150 - 250$ s and a luminosity variation of about a factor of 2 (SkX-MIN and SkX-MAX). The lower limit Q-value calculation with AW95 masses (AW-MIN) is similar to our lower limit (SkX-MIN), but the larger uncertainties in the AW95 masses lead to large differences in the upper limits (SkX-MAX and AW-MAX) and would imply significantly shorter bursts with much more luminous tails (AW-MAX). However, some of the large proton capture Q-values in AW-MAX and to a lesser degree in SkX-MAX are already constrained by the experiments on ^{69}Br and ^{73}Rb. If those constraints are taken into account, one obtains the AW-MAXEXP and SkX-MAXEXP calculations respectively, which are also shown in Fig. 2.9. The SkX-MAXEXP and AW-MAXEXP light curves are very similar.

The dependence of the light curves on the choice of proton capture Q-values can be understood entirely from the changes in β decay and proton-capture branchings of the main waiting points ^{64}Ge, ^{68}Se, and ^{72}Kr shown in Table 2.1. The calculations with the lower limits on proton capture Q-values (SkX-MIN and AW-MIN) do not differ much as they all predict that proton captures do not play a role. However, for the upper limits sizable proton capture branches occur and lead too significant reductions in the lifetimes of the waiting points. In our upper limit (SkX-MAX) 26% proton capture was obtained on ^{68}Se (via 2p capture) and 86% proton capture on ^{64}Ge, while proton captures on ^{72}Kr, with 8%, play only a minor role. These branchings

become even larger for the AW95 upper limit calculations (AW-MAXEXP and AW-MAX). Note that β decay of ^{60}Zn is negligible (See Table 2.1) because proton capture dominates for the whole range of nuclear masses considered here.

Table 2.1: Branchings for proton captures on the most important waiting point (WP) nuclei for different mass predictions from AW95 (AW) and this work SkX. These branchings are the time integrated averages obtained from our X-ray burst model.

WP	SkX	SkX-MIN–MAX	AW-MIN–MAX	AW-MIN–MAXEXP
^{60}Zn	95%	91% - 97%	83% - 98%	83% - 99%
^{64}Ge	30%	0.5% - 86%	0.0% - 98%	0.0% - 99%
^{68}Se	0.5%	0.0% - 26%	0.0% - 74%	0.0% - 15%
^{72}Kr	0.0%	0.0% - 8%	0.0% - 87%	0.0% - 8%

The importance of the one-proton capture Q-values in the determination of lifetimes for *rp* process waiting points has been discussed extensively before [13]. This importance is clearly expressed by the large changes in branching ratios and light curves when experimental constraints (which only exist for one-proton separation energies) are imposed on the AW-MAX calculations leading to AW-MAXEXP (Fig. 2.9 and Table 2.1). However, the two-proton capture Q-values can be equally important. For example, the proton capture branching on ^{68}Se changes by an order of magnitude from 2% in AW to 15% in AW-MAXEXP. This change is entirely due to the change in the ^{70}Kr proton separation energy from 1.86 MeV in AW to 2.4 MeV in AW-MAXEXP as the proton capture Q-value on ^{68}Se is very similar (only 0.05 MeV difference). The reason for this sensitivity is the onset of photodisintegration of ^{70}Kr that depends very sensitively on its proton separation energy. As soon as temperatures are sufficiently high for ^{70}Kr(γ,2p)^{68}Se to play a role, ^{68}Se, ^{69}Br, and ^{70}Kr are driven into a local (p,γ)-(γ,p) equilibrium. With rising temperature the proton capture on ^{68}Se drops quickly to zero, because the temperature independent and slow β decay of ^{70}Kr in Eq. 2.5 cannot provide a substantial leakage out of the equilibrium. This is different from the situation at lower temperatures described by Eq. 2.4 where a lower equilibrium abundance of ^{69}Br at higher temperatures can be somewhat compensated

by the increasing proton capture rate on ^{69}Br. This effect is illustrated in Fig. 2.10 which shows the lifetime of ^{68}Se against proton capture and β decay as a function of temperature for different choices of proton capture Q-values.

The lifetime equals the β decay lifetime for low temperatures because of slow proton capture reactions, and at high temperatures because of the photodisintegration effect discussed above. For the AW masses, the low proton separation energy of ^{70}Kr leads to strong photodisintegration already at temperatures around 1.15 GK before proton captures can play a role. Therefore, proton captures never reduce the lifetime significantly. For AW-MAXEXP, the only change is a larger ^{70}Kr proton separation energy of 2.4 MeV. Though ^{69}Br is unbound by 500 keV, proton captures can reduce the lifetime of ^{68}Se by about a factor of two around 1.4 GK before photodisintegration sets in and starts inhibiting further proton captures. This can be compared with the upper limits of our predictions for proton separation energies (SkX-MAX). The larger proton separation energy of ^{69}Br allows an onset of proton captures at slightly lower temperatures, but the lower proton separation energy of ^{70}Kr leads also to an onset of photodisintegration at somewhat lower temperatures, thus effectively shifting the drop in lifetime by about 0.1 GK. Note that it is not only the amount of lifetime reduction, but also how well necessary conditions match the actual conditions during the cooling of the X-ray burst that determine the role of proton captures and, therefore, the overall time scale of the *rp* process. As Fig. 2.10 shows, both depend sensitively on the nuclear masses.

A long-standing question is how the nuclear physics, and in particular the properties of the long-lived waiting points ^{64}Ge, ^{68}Se and ^{72}Kr affect the end-point of the *rp* process. Even for our lowest proton capture Q-values, where proton captures on ^{68}Se and ^{72}Kr become negligible, we still find that the *rp* process reaches the SnSbTe cycle [15].

Fig. 2.11 shows the final abundance distribution for the two extreme cases – our

calculation with the slowest (SkX-MIN) and the fastest (AW-MAX) reaction flow. In both cases, the most abundant mass number is $A = 104$, which is due to accumulation of material in the SnSbTe cycle at ^{104}Sn. The main difference between the abundance patterns are the abundances that directly relate to the waiting points at $A = 64$, 68, and 72 and scale roughly with the waiting point lifetime. In addition, for AW-MAX nuclei in the $A = 98$–103 mass range are about a factor of 3 more abundant because of the faster processing and the depletion of $A = 64$, 68 and 72.

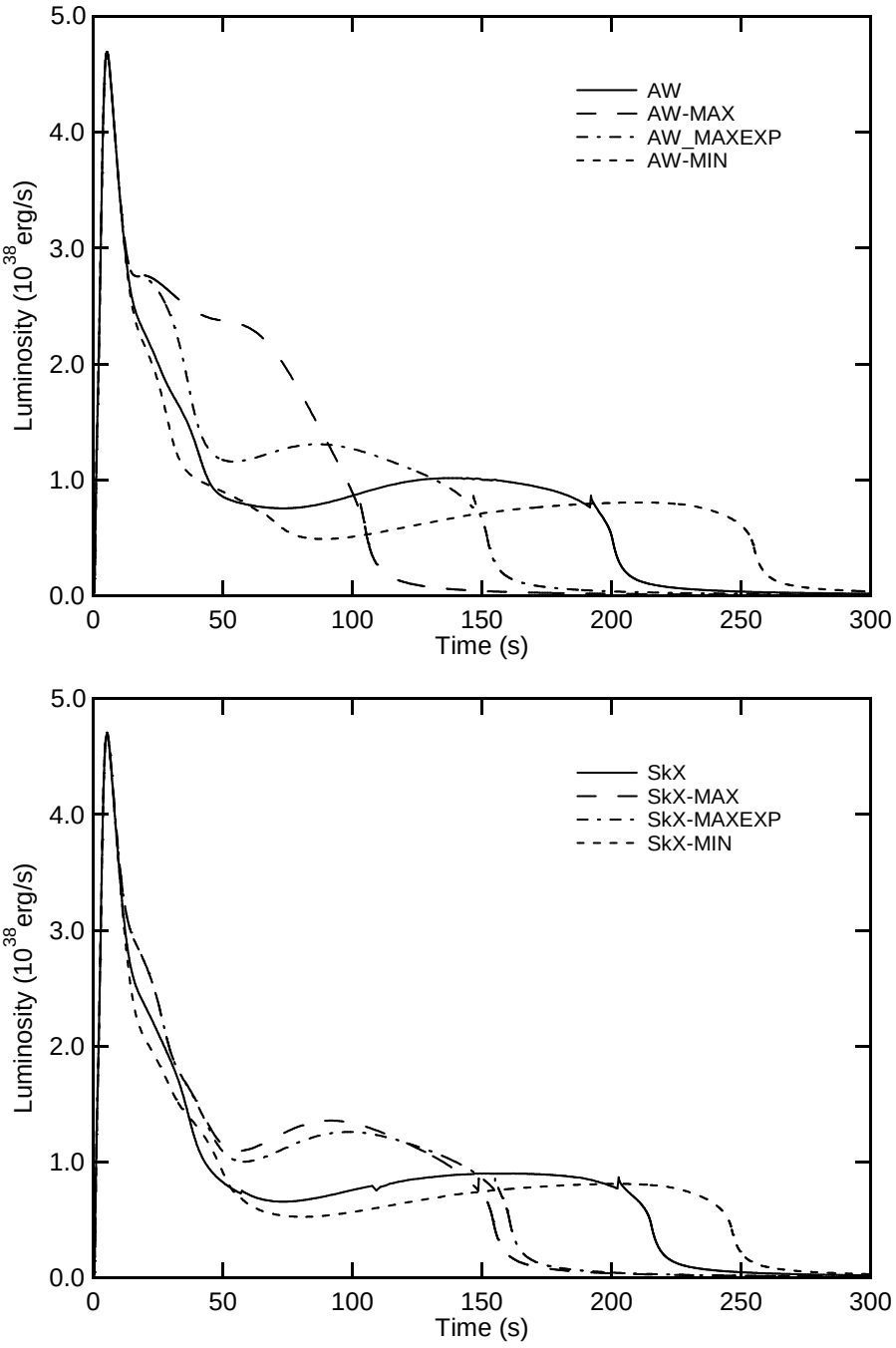

Figure 2.9: X-ray burst luminosity as functions of time for model calculations with different assumptions on proton capture Q-values in the Zn-Sr range: results on the upper panel are based on the Audi & Wapstra 1995 recommended masses (AW) and the largest (AW-MAX) and smallest (AW-MIN) proton capture Q-values according to their error bars. AW-MAXEXP is identical to AW-MAX, but takes into account experimental limits on the proton capture Q-values of ^{68}Se and ^{72}Kr. The lower panel shows the same set of calculations based on the mass predictions of this work (SkX). The mass of the accreted layer is 5.0×10^{21} g.

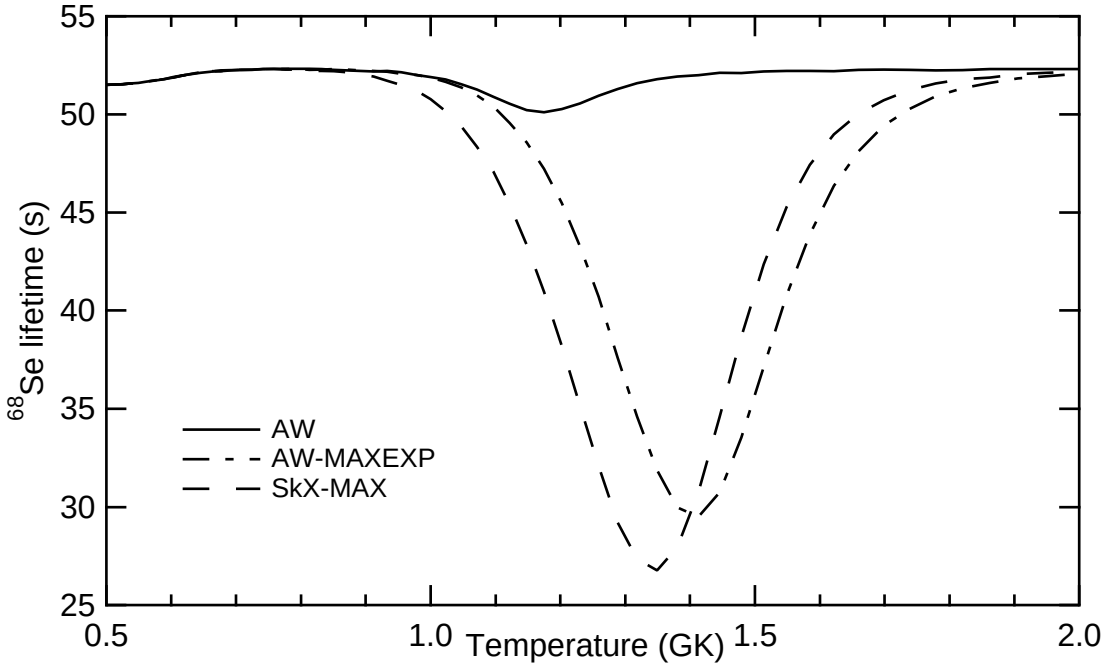

Figure 2.10: The lifetime of ^{68}Se against β decay and proton-capture for typical *rp* process conditions during the burst tail (hydrogen abundance 0.35, density $6{\cdot}10^5$ g/cm^3) for three different assumptions on proton capture Q-values on ^{68}Se and ^{69}Br: Audi & Wapstra 1995 recommended masses (AW), the largest proton capture Q-values within the AW error bars but with experimental constraints on the ^{68}Se(p,γ) Q-value (AW-MAXEXP), and the largest proton capture Q-values within the error bars of the predictions from this work (SkX-MAX).

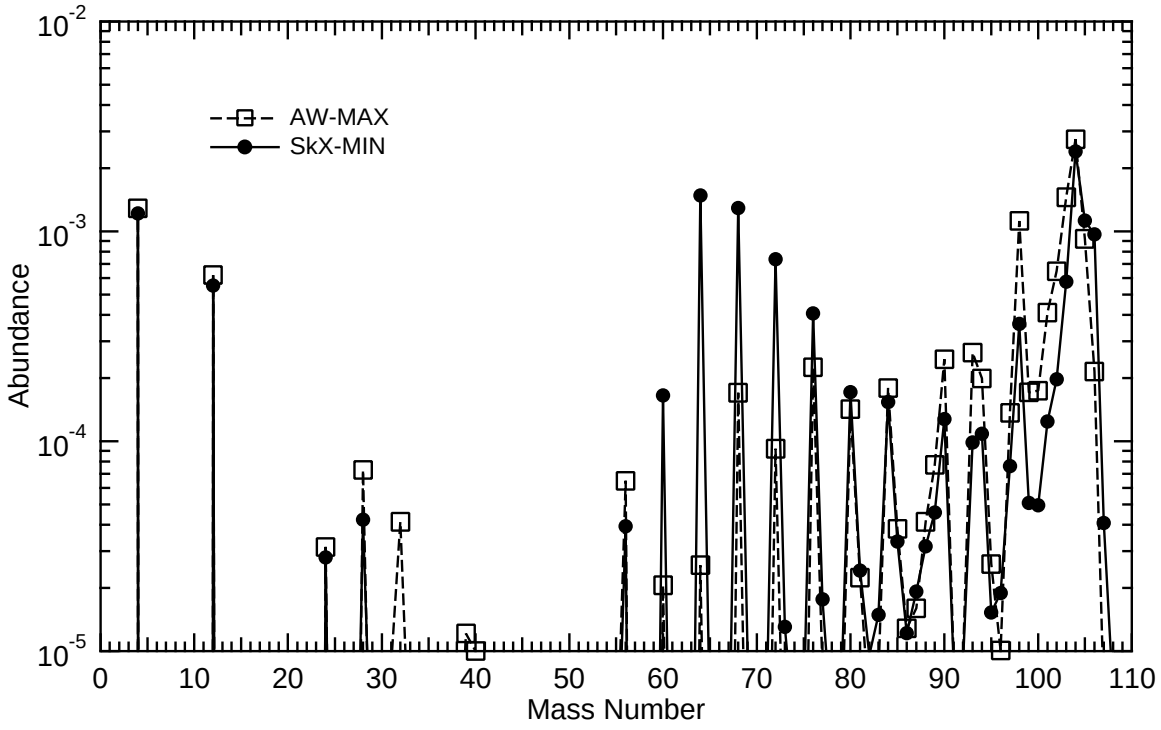

Figure 2.11: The final abundance distribution summed over mass numbers for a calculation with the lowest proton capture Q-values within the uncertainties of the mass predictions of this work (SkX-MIN) and with the largest proton capture Q-values within the uncertainties of AW95 (AW-MAX).

2.6 Summary and Conclusions

A new set of predictions were made for the masses of proton-rich nuclei on the basis of the displacement energies obtained from spherical Hartree-Fock calculations with the SkX_{csb} Skyrme interaction [24, 25]. SkX_{csb} provides a large improvement in the displacement energies over those obtained with other Skyrme interactions via the addition of a one-parameter charge-symmetry breaking component [25]. A comparison with the experimental displacement energies measured in the mass region A=41– 59 indicates that the accuracy of the calculated displacement energies is about 100 keV. Thus this was used as a measure of the uncertainty expected for the higher mass region of interest in this work. Experimental masses for some proton-rich nuclei in the mass region A=60-70 will be required to test the predictions. At the upper end, some deviation was expected due to the very deformed shapes which involve the excitation of many pf-shell nucleons into the $g_{9/2}$ (sdg) shell which go beyond the spherical approach. In addition to the application to the rp process, the implication of the present model for the proton drip line. The most promising candidates for diproton emission are ^{64}Zn, ^{59}Ge, ^{63}Se, ^{67}Kr and ^{71}Sr.

The rp process calculations based upon the masses obtained in the present model and those obtained from the Audi-Waptra mass extrapolations clearly demonstrate the sensitivity of X-ray burst tails on nuclear masses at and beyond the $N = Z$ line between Ni and Sr. Such a sensitivity on the Q-values for proton capture on ^{64}Ge and ^{68}Se has been pointed out before by Koike et al. [19] based on a similar X-ray burst model. However, Koike et al. [19] used a limited reaction network only including nuclei up to Kr. As shown in this work, this is not sufficient for any assumption on nuclear masses, and as a consequence, very different light curves and final abundances are found.

The new calculation leads to tighter constraints on proton capture Q-values as compared with the AW95 mass extrapolations (see Fig. 2.9). The first radioactive

beam experiments, including the nonobservation of ^{69}Br and ^{73}Rb, have also begun to provide important constraints. If those experiments are taken into account, the new predictions do not lead to substantially tighter limits, with the exception of the proton capture on ^{64}Ge, where no experimental upper limit on the proton capture Q-value exists. The new calculations increase the minimum β branching at ^{64}Ge by an order of magnitude from 1% to 14%, leading to a lower limit of the average ^{64}Ge half-life in the *rp* process of 12.6 s instead of 0.9 s. As a consequence, a smooth and continuous drop in the light curve during the first 30–40 s after the maximum was predicted, as opposed to the hump predicted with AW-MAX.

However, uncertainties in the mass predictions are still too large to sufficiently constrain the light curves and to determine the role that proton captures play in the reduction of waiting point lifetimes. While found that within the errors of our mass predictions proton capture on ^{72}Kr is negligible, the predicted average proton capture branchings for ^{64}Ge and ^{68}Se still cover a large range of 0.5%–86% and 0.0% - 26% respectively (of course this is a model-dependent result - for example, more hydrogen or a higher density could strongly increase the proton capture branches). To a large extent this is because of the large uncertainties in the masses of $N = Z$ nuclei ^{64}Ge (measured: 270 keV), ^{68}Se (AW95 extrapolated: 310 keV), and ^{72}Kr (measured: 290 keV) [4] that cannot be determined with the method presented here. In addition, uncertainties in the masses of mirror nuclei increase the errors for ^{73}Rb (170 keV) and ^{70}Kr (160 keV) substantially beyond the ≈100 keV accuracy of our predicted Coulomb shifts. Overall, this results in typical uncertainties of the order of 300 keV for several of the critical proton capture Q-values.

To summarize, uncertainties in the masses of the nuclei that determine the proton capture branches on ^{64}Ge and ^{68}Se represent a major nuclear physics uncertainty in X-ray burst light curve calculations. The relevant nuclei are listed in the upper part of Table 2.2 together with the currently available mass data and their uncertainties.

The proton capture branches on ^{60}Zn and ^{72}Kr are of similar importance, but are sufficiently well constrained by current experimental limits and theoretical calculations. However, both the experimental and the theoretical limits are strongly model dependent. Therefore, improved experimental mass data would still be important to confirm the present estimates. These nuclei are listed in the lower part of Table 2.2. As discussed in Sec. 2.4 there is experimental evidence indicating proton stability of all the nuclei listed, except for ^{69}Br and ^{73}Rb, which are probably proton unbound. Mass measurements of the proton bound nuclei could be performed with a variety of techniques including ion trap measurements, time of flight measurements, or β decay studies. Recent developments in the production of radioactive beams allow many of the necessary experiments to be performed at existing radioactive beam facilities such as ANL, GANIL, GSI, ISOLDE, ISAC, and the NSCL. Mass measurements of the proton unbound nuclei ^{69}Br and ^{73}Rb require their population via transfer reactions from more stable nuclei, or by β decay from more unstable nuclei. Both are significantly more challenging as much higher beam intensities or the production of more exotic nuclei are required, respectively.

Of course, burst timescales depend sensitively on the amount of hydrogen that is available at burst ignition. The more hydrogen that is available the longer the *rp* process and the longer the burst tail timescale. In this thesis a model with a large initial hydrogen abundance (close to solar) was used to explore the impact of mass uncertainties on X-ray burst light curves. This allowed drawing conclusions on the uncertainties in predictions of the longest burst timescales and the heaviest elements that can be produced in X-ray bursts. The former is important for example in light of recent observations of very long thermonuclear X-ray bursts from GX 17+2 [39], the latter for the question of the origin of p nuclei discussed below. Nevertheless, a similar light curve sensitivity to masses for other models was expected as long as there is enough hydrogen for the *rp* process to reach the $A = 74-76$ mass region. In the one

Table 2.2: Nuclei for which more a accurate mass would improve the accuracy of *rp* process calculations in type I X-ray bursts. The upper part of the table lists nuclei for which the current uncertainties lead to large uncertainties in calculated burst time scales. The lower part of the table lists nuclei, for which accurate masses are important, but current estimates of the uncertainties do not lead to large uncertainties in *rp* process calculations. Nevertheless, an experimental confirmation for the masses being in the estimated range would be important. Within each part, the nuclei are sorted by uncertainty, so a measurement of the top ranked nuclei would be most important. For each nucleus we list either the experimental mass excess (Exp) ([4] and [5] for ^{70}Se) or the theoretical mass excess (SkX) calculated in this work in MeV.

Nuclide	Exp	SkX
^{68}Se		-54.15 ± 0.30[a]
^{64}Ge	-54.43 ± 0.250	
^{70}Kr		-40.98 ± 0.16
^{70}Se[b]	-61.60 ± 0.12	
^{65}As		-46.70 ± 0.14
^{69}Br		-46.13 ± 0.11
^{66}Se		-41.85 ± 0.10
^{72}Kr	-54.11 ± 0.271	
^{73}Rb		-46.27 ± 0.17
^{73}Kr[b]	-56.89 ± 0.14	
^{74}Sr		-40.67 ± 0.12
^{61}Ga		-47.14 ± 0.10
^{62}Ge		-42.38 ± 0.10

[a] Theoretical estimate from AW95.
[b] Mirror to an *rp* process nucleus - a more accurate mass measurement could reduce the error in the mass prediction for the proton rich mirror nucleus by more than 30%.

zone model it was found that this requires about a 0.35-0.45 hydrogen mass fraction at ignition. Even though the burst temperatures and densities vary somewhat with the initial conditions we find shorter, but otherwise very similar reaction paths governed by the same waiting point nuclei. For bursts with initial hydrogen abundances below ≈ 0.3 the *rp* process does not reach the $A = 60 - 72$ mass region anymore and the mass uncertainties discussed in this work become irrelevant.

Observed type I X-ray bursts show a wide variety of timescales ranging from 10 s to hours. The goal is to improve the underlying nuclear physics so that the observed

burst timescales can be used to infer tight constraints on ignition conditions in type I X-ray bursts such as the amount of hydrogen available for a given burst. Such constraints would be extremely useful as they could, for example, lead to constraints on the impact of rotation and magnetic fields on the fuel distribution on the neutron star surface as well as on the heat flux from the neutron star surface [2, 40]. Our results indicate that without further theoretical or experimental improvements on nuclear masses it will not be possible to obtain such tight, quantitative constraints.

Nevertheless, some qualitative conclusions can already be drawn on the basis of the new mass predictions. The new results provide strong support for previous predictions that the *rp* process in the $A = 64 - 72$ mass region slows down considerably leading to extended burst tails [15]. As a consequence, the long bursts observed for example in GS 1826-24 [2] can be explained by the presence of large amounts of hydrogen at ignition and can therefore be interpreted as a signature of the *rp* process.

Even for the lowest proton capture Q-values, when ^{68}Se and ^{72}Kr slow down the *rp* process with their full β decay lifetime the *rp* process still reaches the SnSbTe cycle. Clearly, such a slowdown of the *rp* process does not lead to a premature termination of the *rp* process as has been suggested previously (for example [17]), but rather extends the burst time scale accordingly. As a consequence we find that hydrogen is completely consumed in our model.

However, a slower *rp* process will produce more nuclei in the $A = 64$–72 range and less nuclei in the $A = 98$–103 mass range. Interestingly, among the most sensitive abundances beyond $A = 72$ is ^{98}Ru, which is of special interest as it is one of the light p nuclei whose origin in the universe is still uncertain. p nuclei are proton rich, stable nuclei that cannot be synthesized by neutron capture processes. While standard p process models can account for most of the p nuclei observed, they cannot produce sufficient amounts of some light p nuclei such as ^{92,94}Mo and ^{96,98}Ru (for example [41]). Costa et al. [42] pointed out recently that a increase in the ^{22}Ne(α,n) reaction rate by

a factor of 10-50 above the presently recommended rate could help solve this problem, but recent experimental data seem to rule out this possibility [43]. Alternatively, X-ray bursts have been proposed as nucleosynthesis site for these nuclei [13, 15]. An accurate determination of the ^{98}Ru production in X-ray bursts requires, therefore, accurate masses in the $A = 64 - 72$ mass range. Further conclusions concerning X-ray bursts as a possible p process scenario have to wait for future self-consistent multi-zone calculations with the full reaction network that include the transfer of the ashes into the interstellar medium during energetic bursts.

Chapter 3

Nuclear Spectroscopy

3.1 Introduction

In chapter 2 it was shown how important the mass of nuclear isotopes are to the modeling of X-ray bursts, and in particular, to nucleogenesis via the *rp* process. Hence, the uncertainty in these masses must be addressed in order to make progress in our understanding of this astrophysical scenario and the related problem of modeling novae. In addition, excitation energies of key states and their reaction Q values are often the most important factors in determining resonant or nonresonant capture rates at a given temperature. Therefore, to accurately determine the proton capture reaction rates we must be able to measure the properties of key states.

Though the neutron deficient states of interest are proton unbound, the states that dominate the reaction rates at temperatures found in the *rp* process have lifetimes long enough to decay via gamma ray emission due to the Coulomb barrier. Provided the proton unbound states of interest can be populated with an appropriate reaction mechanism, the resulting gamma rays can, in principle, be measured yielding information about the level structure. Reaction mechanisms that remove neutrons are well suited to this kind of study since primary beam rates are higher closer to stability.

The (p,d) reaction was chosen because it had a relatively large cross section, of order of magnitude 1 *mb* for the beam energies of the secondary beams available, and the reaction mechanism was well understood. One challenge in using the (p,d) reaction was the need for a proton target. Though pure proton targets are technically possible, as frozen hydrogen, they were not available for this study. Therefore, a polypropylene target was used. In this case reactions on carbon must also be considered. Taking measurements on a pure carbon target and subtracting the appropriate amount from the results of the polypropylene target experiment could accomplish this. However, carbon is an excellent target in that it also has a large cross section for neutron removal by knockout reaction from the projectile. Fortunately, the knockout reaction mechanism was also well understood [44]. Because neutron removal cross sections and related information are not needed for a precise measurement of the excitation energies, the lack of information about what reaction populated the excited states presented minor difficulty. A problem with using two reactions was the loss of a meaningful momentum distribution as each reaction has its own unique set of dynamics. Fortunately, several of the neutron rich mirror nuclei are well studied and this information can be used to make J^{π} assignments and for guidance in understanding the measured decay schemes.

In order to test the method, the ^{33}Ar isotope was chosen. The choice of ^{33}Ar was based on two main factors. First, the recent upgrade of the facilities at the NSCL yield an intense beam of ^{36}Ar, which would allow for sufficient ^{34}Ar nuclei to quickly debug any unanticipated problems that may occur with any new technique. Second, ^{33}Ar is an important, yet relatively unknown nucleus on the path of the *rp* process that proceeds via the ^{32}Cl(p,γ)^{33}Ar reaction.

3.1.1 Experimental Technique

The technique can be broken down into three main parts. The first consists of secondary beam production. The second, particle identification, and the third coincident gamma ray reconstruction. Each of these will be discussed in the subsequent sections.

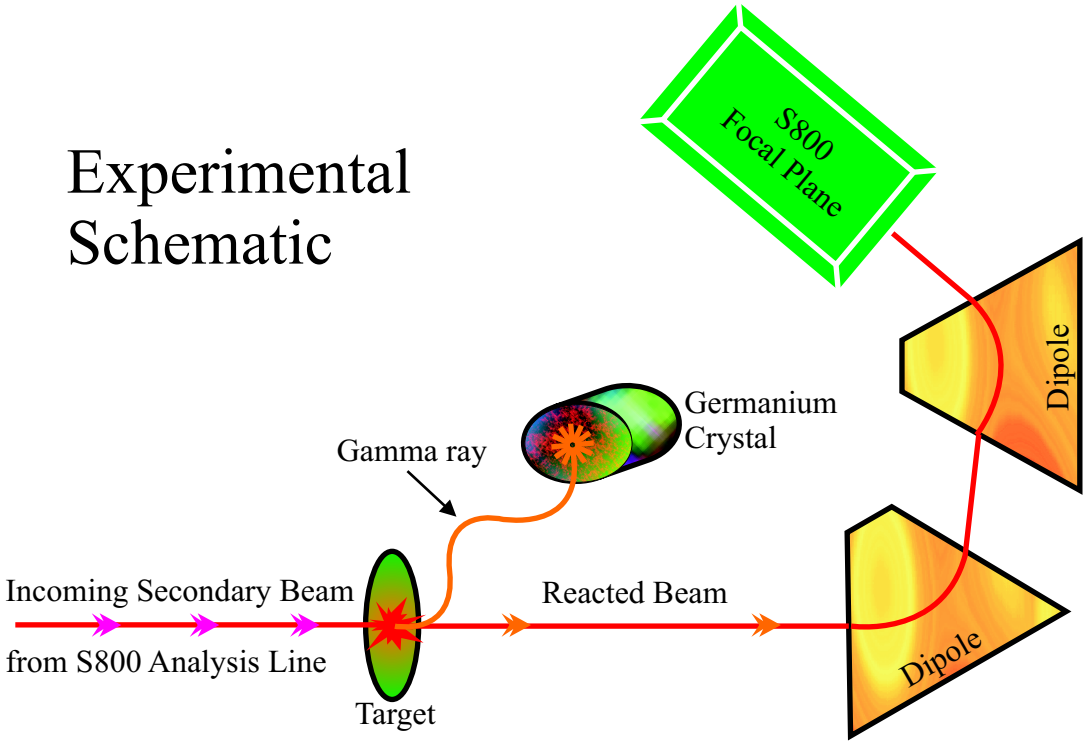

Figure 3.1: Cartoon of the experimental setup.

The experiment began when a secondary beam of radioactive isotopes produced in the A1900 fragment separator was transported to the S800 analysis line. The S800 analysis line was used with the S800 spectrograph operated in dispersion matched, energy loss mode. A schematic of the experiment is shown in Fig. 3.1. The secondary beam, in red, left the S800 analysis line and interacted with the target at the entrance of the S800 spectrograph. The S800 was set to accept the ^{33}Ar particles produced as the beam reacted with the target. The S800 provided unique particle identification for ^{33}Ar produced from the ^{34}Ar beam. With a unique particle identification, the coincident gamma rays, the orange wavy line in Fig. 3.1, were identified with a particle

as they were collected in the segmented germanium array (SeGA) crystals. When the gamma rays were measured in the lab frame, a Doppler correction was applied to reconstruct the correct center of mass (CM) decay energies.

3.2 Secondary Beam Properties

Secondary beam production began with ^{36}Ar gas entering an electron cyclotron resonance ion source (ECR), which for this experiment was the advanced room temperature ion source (ARTEMIS). In the ECR, the gas was heated into a plasma so as to strip and create a net positive charge on the ^{36}Ar atoms. The ^{36}Ar ions were then injected into the K500 cyclotron where they were further accelerated for injection into the K1200 cyclotron. A stripper foil was located at the center of the K1200 cyclotron where the remaining electrons were removed from the ^{36}Ar ions. Once fully stripped in the K1200, the ions were accelerated to 150 $MeV/nucleon$ and were then sent from the K1200 to the production target of the A1900 where the secondary beam was produced. The secondary beam was made by stripping neutrons from ^{36}Ar. After the production of the ^{34}Ar secondary beam in the primary production target, the beam was passed through another material "wedge" that aided in the separation of the various fragments in the beam. The secondary beam of interest was then transmitted through the second half of the A1900 fragment separator and delivered to the S800 analysis line. The relevant beam production parameters for the experiment presented in this dissertation are given in table 3.1:

Table 3.1: Secondary beam production information.

K500 MeV/nuc	K1200 MeV/nuc	^{9}Be Production Target (mg/cm^2)	Al "Wedge" mg/cm^2	Energy MeV/nuc	Beam
13.0	150.0	587	240	104.0	^{35}Ar
13.0	150.0	1034	240	83.8	^{34}Ar

3.3 Experimental Hardware and Software

3.3.1 MSU Segmented Germanium Detector Array

The MSU segmented germanium detector array (SeGA) [45–47] consisted of an array of eighteen, thirty-two fold, high-purity segmented germanium detectors – all of which were located 20 *cm* from the polypropylene target used for this experiment. The geometry of the detector system is shown in Figs. 3.2 and 3.3. As shown in the figures, the array had two rings, a 37° ring and a 90° ring, each capable of holding eight and ten detectors, respectively. However, due to the large gate valve on the entrance to the S800 spectrograph, only seven detectors were actually mounted on the detector frame. This experiment had five detectors operational in the 37° ring and eight detectors in the 90° ring. The detectors used in the 37° ring were, as labeled in Figs. 3.2 and 3.3: 1, 2, 4, 6 and 9. The detectors used in the 90° ring were, as labeled in Figs. 3.2 and 3.3: 12, 13, 14, 17, 19, 20, 21 and 22. The intrinsic energy resolution of the SeGA detectors [45] varied from 2.5 to 2.8 keV at 1332 keV.

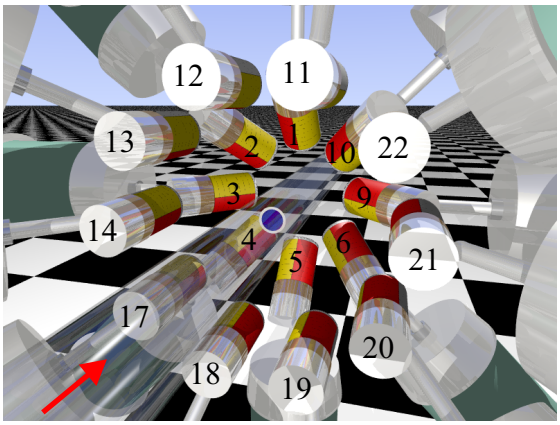

Figure 3.2: SeGA back view. The crystal housing are labeled by detector number. The grey and aqua colored cylinders are the cryostats. The red arrow labels the beam direction and the target is the purple circle in the middle.

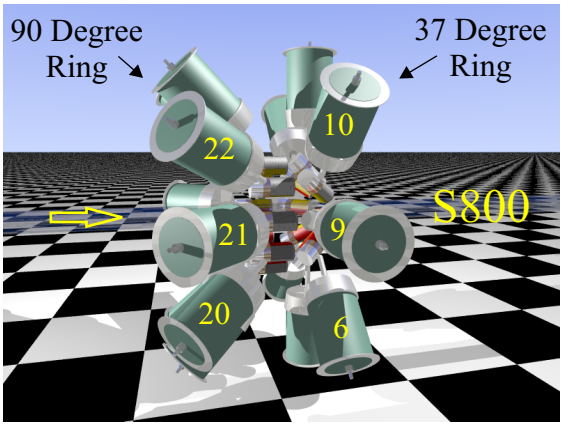

Figure 3.3: SeGA Side View

SeGA Energy and Efficiency Calibration

Energy calibration of the SeGA detectors was carried out by placing a source of known gamma ray energies at the target position and then using a quadratic function that transformed the raw 13-bit spectra from the detectors into calibrated energy spectra. This calibration was performed with the standard sources ^{56}Co, ^{133}Ba and ^{152}Eu. A total of 24 known gamma rays were used for this purpose, ranging from 80.9971 (12) keV to 3.451119 (4) MeV. As the large gate valve of the S800 near the array was previously activated by its use as a beam stop, the spectra from the gate valve were analyzed and any calibration source gamma ray that coincided in energy with a contamination peak from the gate valve was not used. The data was then rescanned and checked to assure the quality of the calibration procedure. The error in the energy calibration ranged from 0.01 keV at lower gamma ray energies (less than 1 MeV) to a few tenths of a keV above 1 MeV.

In order to determine the intensities (I) of the Doppler corrected gamma rays, the number of counts in the photo peak ($Area$) was divided by the efficiency (Eff) of the detector setup, *i.e.*

$$I = \frac{Area}{Eff}. \tag{3.1}$$

Therefore, to find I, we determined the photo peak area of the measured gamma rays

as well as the efficiency of SeGA for a gamma ray emitted from a moving reference frame.

The efficiency calibration procedure was carried out using the same sources as above in concert with GEANT simulations. The sources ^{56}Co, ^{133}Ba and ^{152}Eu have known gamma ray decay intensities and half-lives, in addition to having known gamma ray decay energies. These calibrated sources have their activities measured so that when combined with the time since manufacture, the source activity was well known. The efficiency calibration for the experiment is somewhat different due to the Doppler correction. Because the Doppler shift is different for the two rings, the two rings must be calibrated separately. Analytically, the angular dependence of the Doppler correction is given by

$$E_{\gamma}^{part} = \frac{E_{\gamma}^{lab}(1 - \beta^{lab} cos(\theta^{lab}))}{\sqrt{1 - (\beta^{lab})^2}} \tag{3.2}$$

where *lab* denotes the laboratory frame values and *part* the particle CM frame values.

The procedure for ultimately determining the intensities of measured Doppler corrected gamma rays involved several steps. The details of each step are given in

Table 3.2: Outline of SeGA efficiency callibration procedure.

Step	Result
• Measure calibrated sources	Measured efficiency for $\beta = 0$ γs
• GEANT simulation of $\beta = 0$ γs	Simulated efficiency for $\beta = 0$ γs
• GEANT/Data comparison	Simulation correction factor (f_G)
• Simulate 10M $\beta = 0.386$ γs	Simulated efficiency for
Determine $\beta = 0.386$	$\beta = 0.386$ γs
simulated peak areas	
• Scale simulation to data	Scaling factor for
for $\beta = 0.386$ γs	GEANT simulations (f_d)
• Intensity of $\beta = 0.386$ γs	$I = \frac{f_d * 10M}{f_G}$

Tab. 3.2.

The measured efficiency for a gamma emitted from a $\beta = 0$ source (*i.e.* at rest) of each ring was calculated as

$$Efficiency = \frac{PeakArea}{Intensity \times LiveRatio \times RunLength \times SourceActivity}. \quad (3.3)$$

where *SourceActivity* is the known activity of the source. The *LiveRatio* is a measured quantity that is related to the amount of time the data acquisition was available for taking data relative to the amount of time data was taken (*RunLength*). In order to accurately determine the *PeakArea*, the shape of the peak must be correctly taken into account. The peak shape used was adapted from the standard gamma analysis package GF3 [48] by D. Radford. The form of this function has three components: a low energy skewed Gaussian, which accounts for incomplete energy collection; a Gaussian, for the main photo-peak; and a quadratic background. Mathematically, the shape is a sum of

$$skew = A_0 \times (\frac{R}{100} \times e^{\frac{x-x_0}{\sigma}} \times Erfc(\frac{\sigma + x - x_0}{\sqrt{2}\sigma}) \quad (3.4)$$

$$Gaussian = A_0 \times (1 - \frac{R}{100}) \times e^{\frac{-(x-x_0)}{2\sigma}} \quad (3.5)$$

$$quadratic\, background = a * x^2 + b * x + c. \quad (3.6)$$

The parameters R and $\sigma(keV)$ were fixed in the final fits as their energy dependence had been determined prior to the final fit and were linearly parameterized as a function of energy by a least squares fit to the source data. Fig. 3.4 shows the 37° ring σ vs. energy data, along with the corresponding fit line.

Once all efficiency data were fit, the area and associated error were calculated by standard error propagation. The area for the fit function was calculated by finding the antiderivative for the fit function on a finite closed domain, $[-x, x]$, and then taking

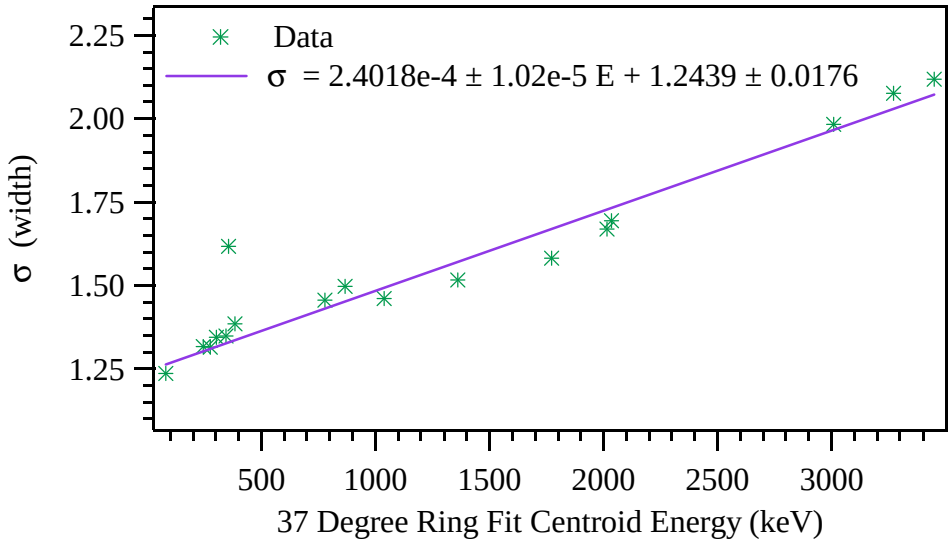

Figure 3.4: The fits with $\sigma(keV)$ and R allowed to vary yielded the data points. A line was then fit to the data to determine the linear energy dependence of the change in σ as a function of energy The outlier at 356 keV was eliminated from the fit.

the limit $x \rightarrow \infty$. Formally, the functional form is given by

$$Area = A_0\sigma(\sqrt{2\pi} + \frac{(2-\sqrt{2e\pi})R}{100\sqrt{e}}). \tag{3.7}$$

The results of the efficiency calculation, given by the source data for both rings with error bars, are displayed in Fig. 3.5.

The next task was to determine the efficiencies of Doppler corrected gamma rays. In order to do this, a GEANT simulation [49] of the detector setup was performed. The simulation makes a Monte Carlo simulation with ten million gamma rays at the measured Doppler corrected particle frame energies, assuming isotropic emission in the CM frame. The simulation models the response of the detector system for the incident gamma rays as they are detected in the lab frame.

The simulated efficiency for gammas emitted from a $\beta = 0$ source was then directly scaled by a least squares fit to the measured source data efficiency to correct for a small difference between the simulated efficiency and the measured efficiency. The

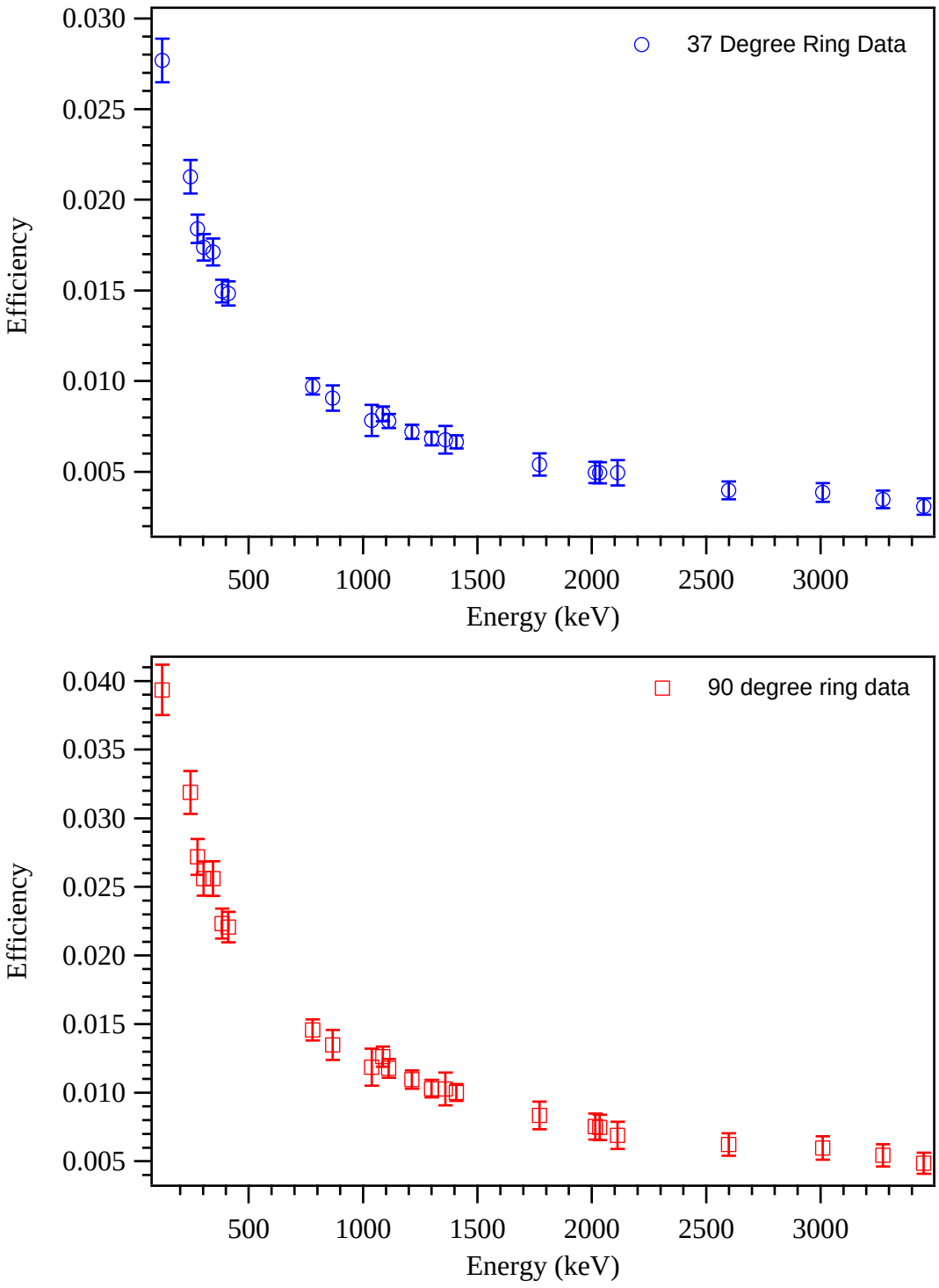

Figure 3.5: The 37 and 90 degree ring efficiency data showing the dependence of efficiency on energy. The data come from the three standard sources of ^{56}Co, ^{133}Ba and ^{152}Eu used for this experiment.

difference between the measured and the simulated efficiency was approximately 1%. This scaling factor (f_G) represents a global adjustment of the simulated efficiency and is, therefore, valid at all energies of interest.

The next step in finding the CM efficiency was to perform a simulation for 10M gamma rays emitted for a $\beta = 0.386$ source. We determined by what factor the GEANT simulation had to be reduced to match the experimental data (scaling factor f_d); Fig. 3.6 shows an example for the ^{33}Ar 1359 keV peak in the 37 degree ring.

In order to calculate the simulated efficiency, we needed to determine the area in the photo peak of the simulation. The efficiency determined by the simulation is then the area in the photo peak of the simulation ($Asim$) divided by $10M$. Analytically, $Efficiency = \frac{f_G * Asim}{10M}$. The measured photo peak area of our data was $Data\ Photo\ Peak\ Area = f_d * Asim$. The actual number of emitted gamma ray was determined from $number = \frac{10M * f_d}{f_g}$. Only one peak fit was necessary in this process, the peak fit of the GEANT simulation. The photo peaks from the simulation were fit with two skewed Gaussians and one Gaussian. The reduced chi-squared for these fits were all near unity.

A possible correction to the above procedure would be to take into account the angular distribution $W(\Theta)$ of the emmited gamma rays due to the reaction mechanism. A simulation [50] to check how important this effect might be was performed assuming a 50% alignment, which is at least a factor of two more than expected. The simulation showed that for the 37 and 90 degree rings, the dipole and quadrupole distributions have nearly identical $W(\Theta)$ distributions; therefore, separating the polarities was not possible. Further, changes in the angular distribution due to parallel (oblate) and perpendicular (prolate) alignment, with respect to the beam momentum, gave an approximately 5% effect. Again not significant since efficiency is only measurable to the 10% level.

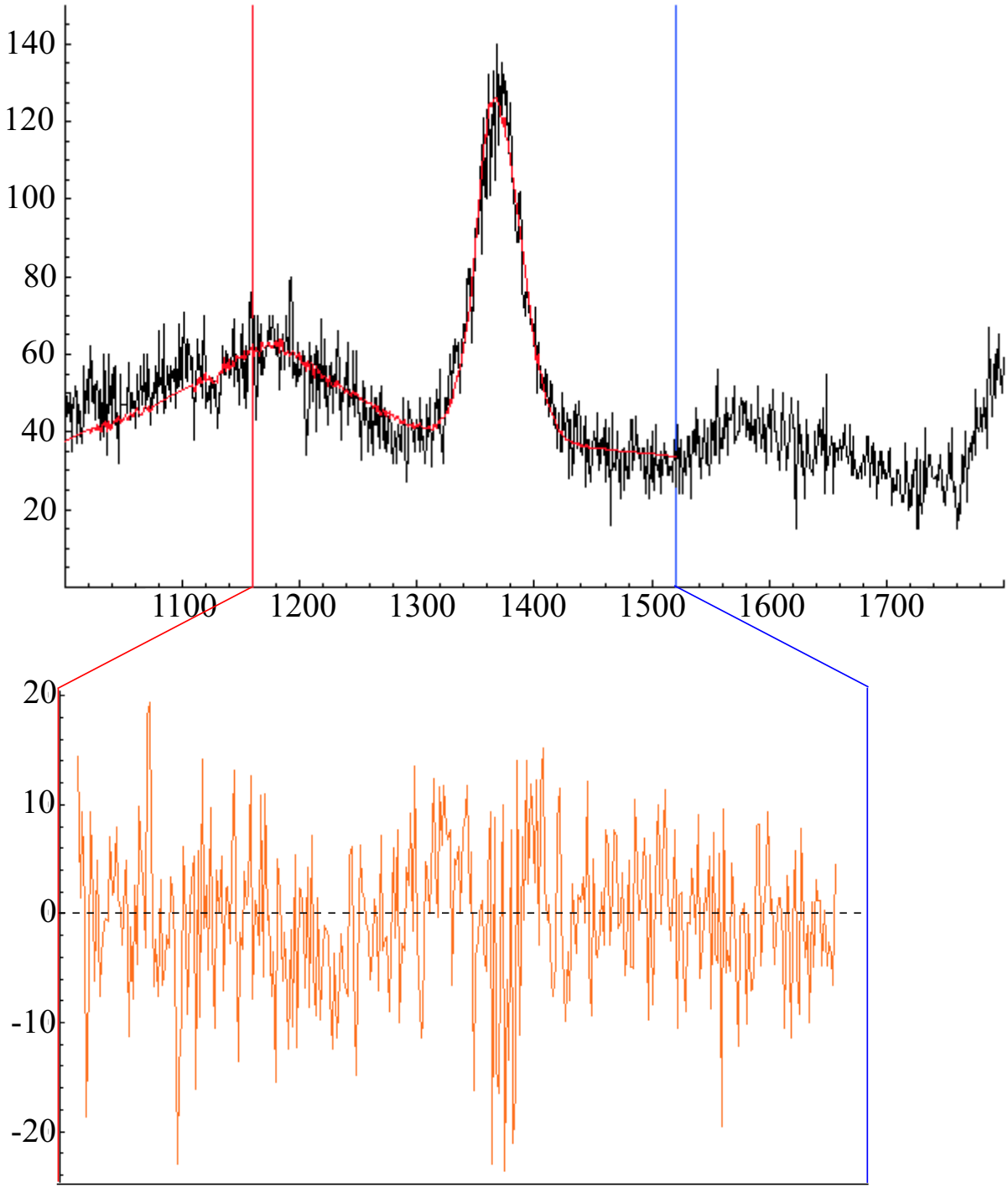

Figure 3.6: GEANT simulated gamma-ray spectra scaled to the ^{33}Ar 1359 keV peak in the 37 degree ring. The experimental spectrum is in black while the simulation is in red. The two vertical lines on either side of the peak denote the left and right endpoints of the fit area. The abscissa units are in counts and the ordinate in keV. The plot in orange directly below is an enlarged view of the fit region containing the residual between the simulation and the data.

3.3.2 S800 Spectrograph

The S800 spectrograph [51, 52], Figs. 3.7 & 3.8, was used to obtain both particle identification and event reconstruction of parameters for the reaction. These will

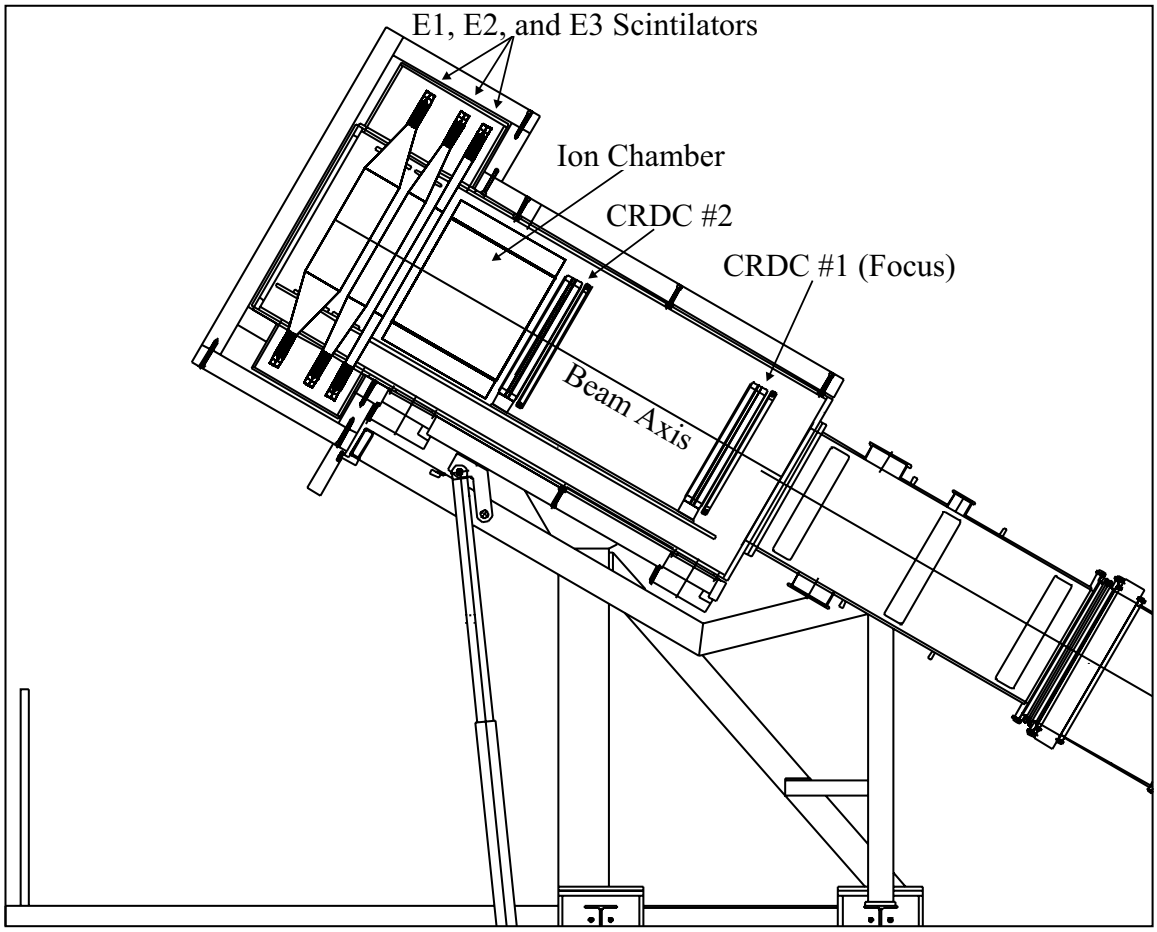

Figure 3.7: S800 focal plane has six detectors. The first three detectors, moving from right to left, are gas detectors. The second set of three detectors are plastic scintillators.

be outlined in detail in the sections 3.4.1 and 3.3.2, respectively. In general, the S800 spectrograph is a large acceptance, magnetic, charged particle, spectroscopy device. Several of its notable characteristics are: Momentum acceptance of 5%; angular acceptance of 7 degrees in the dispersive plane and 10 degrees in the non-dispersive plane, which corresponds to a solid angle of 20 msr; and a dispersion of 9.6 $cm/\%$. The S800 spectrograph was operated in dispersion matched, energy loss mode. This

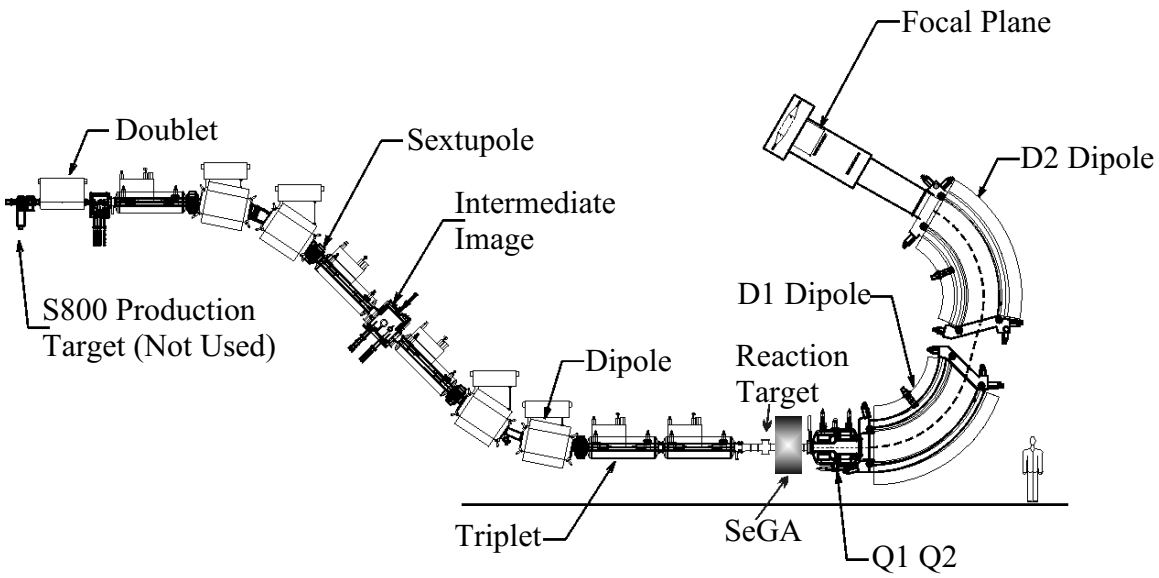

Figure 3.8: S800 spectrograph with SeGA placeholder.

mode of operation is detailed in [52].

Cathode Readout Drift Counters

The cathode readout drift chambers (CRDC) measure position in two dimensions, and consequently, angles in the horizontal and vertical planes. The CRDC's are filled with a mixture of 80% CF_4 (Freon 14) and 20% iC_4H_{10} (IsoButane). The thin windows for the detectors used in this experiment limited the gas pressure to 50 $Torr$. The high purity gas was filtered and regulated by a new gas handling system developed as a part of this thesis work. An introduction to the software interface is provided in appendix A. Charged particles ionized the gas and the liberated electrons then drifted in the electric field toward the anode wire. As the charge was collected on the anode wire an image charge was induced on the pads [51]. The calibrated drift time yielded the y-position and the calibrated pad position yielded the x-position. The calibration was carried out by means of a mask placed between the incoming beam and the CRDC. The mask had holes and slits in known positions with respect to the beam axis. An example of a calibration spectra is given in Fig. 3.9.

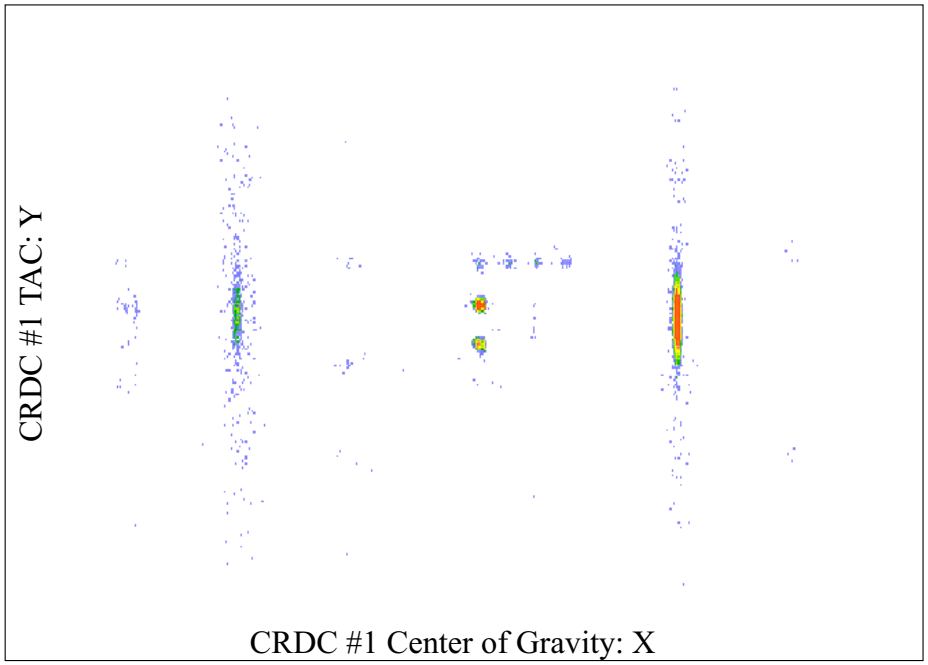

Figure 3.9: XY plot of the beam on CRDC1 after passing through calibration mask. The data is taken from a 10bit by 10bit spectrum of the raw, uncalibrated, parameters.

Each CRDC had a total of 224 pads. Since each pad had a slightly different response, $\pm 6\%$, a gain matching procedure was used. The position of a particle passing through the detector was taken as the centroid of the charge distribution collected on the pads. The pad centroid was determined by fitting a Gaussian peak shape to the pads in the vicinity of the pad with the maximum response to a particular event. This fit procedure allowed for an improved centroid determination over a weighted mean technique. However, if the response of each pad was not uniform then the charge distribution across the pads would not have the correct form and could have, in principle, caused the fit routine to fail.

Further, to improve the quality of the position calibration, an iterative position correction procedure was used in conjunction with a virtual focal plane. The virtual focal plane takes into account the fact that the mask was not at the same position as the center of the CRDC. In fact, they were $8cm$ apart. The procedure consists of comparing the raw parameters with the mask position to obtain a slope and offset,

i.e.

$$Y_{mm} = slope_Y \times channelnumber + offset_Y \tag{3.8}$$

with units $[slope_Y] = mm/ch$ $[offset_Y] = mm$ and

$$X_{mm} = slope_X \times padnumber + offset_X \tag{3.9}$$

with units $[slope_X] = mm/pad$ $[offset_X] = mm$.

The data were then rescanned into the calibrated X and Y parameters. The XY positions of the data were then found then used to correct the slope and offsets of the XY calibrations. Since the calibration was linear, the new slope and offset were easily found. The new offset and slope are given by the equation,

$$Y_{new} = slope_{old} \times slope_{new} + slope_{new} \times offset_{old} + offset_{new} \tag{3.10}$$

where "old" is the last iterations slope/offset and "new" is the current value. The procedure gave deviations between the calibration mask positions and the calibrated XY positions of less than $0.3mm$.

The angle that a particle makes with respect to the beam axis as it passed through CRDC1 and CRDC2 was calculated with elementary trigonometry. The CRDCs are a fixed distance apart, 1.073 m. Combining this fact with the X and Y positions from the CRDCs, one can solve for the angles with an inverse trigonometric function.

Finally, the sensitivity of the drift time on gas composition can cause a small, but noticeable, change in the Y position over time. The change in the gas composition can be attributed to several common causes. Initially, when the gas handling system is brought into operation, the system can take several hours to begin to reach a steady state. For this reason, one would like to start the system several days before start

of experimentation. Also, incorrect operation of the system in which the operational parameters are accidentally changed will effect the system until it has sufficient time to regain a steady state. Therefore, as the state of the system was changed prior to experimentation, the resulting change in the Y position was inevitable and subsequently corrected. The correction takes the form of a slight change in the Y position slope. The Y position centroid, as a function of the run number, is shown in Fig. 3.10. The correction was applied event by event.

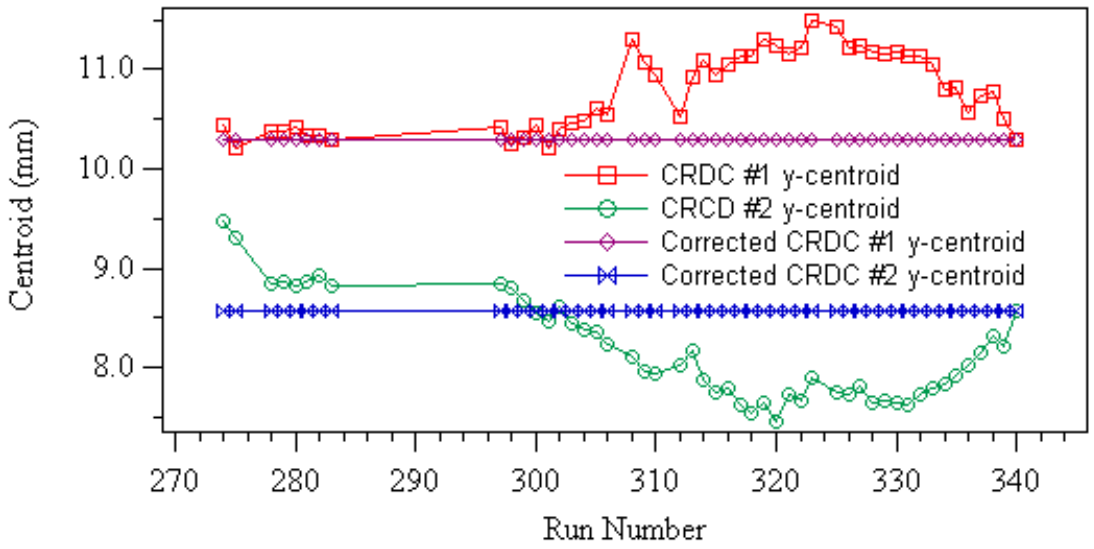

Figure 3.10: The centroid of the Y position is shown as a function of run number for both CRDC's before and after correction. The difference in the increase/decrease in the centroid for the two CRDC's is due to the fact that the CRDC's are rotate 180 degrees with respect to one another on an axis perpendicular to the beam direction and parallel to the dispersive direction. The small scale changes in the centroid as it varies from the general trend are due to statistics, i.e. not all runs are the same length and therefore do not have the same amount of data.

Target Event Reconstruction

The S800 spectrograph consisted of two large superconducting quadrupoles and two 75 degree bend dipoles. Theoretically, if the magnetic fields of the magnets are known exactly, then the trajectory for a given charged particle can be computed exactly. Therefore, given a set of initial positions, subscript i denotes the target chamber

measurements and angles one could find the final positions. Subscript f denotes the focal plane measurements and angles with the use of a transfer matrix,

$$\begin{bmatrix} x_f \\ \theta_f \\ y_f \\ \phi_f \end{bmatrix} = S \begin{bmatrix} \theta_i \\ y_i \\ \phi_i \\ \delta_i \end{bmatrix}, \tag{3.11}$$

where x, y, θ, and ϕ are the positions and angles of our charged particle while δ is the fractional energy, *i.e.*

$$\delta_i = \frac{(E - E_0)}{E_0}. \tag{3.12}$$

The target spot size is assumed to be negligible. The central energy, E_0, is determined by the magnetic field setting of the spectrograph dipoles. For a charged particle moving in a uniform magnetic field

$$B\rho \propto \frac{p_0}{Q} \tag{3.13}$$

where, B is the magnetic field in Telsa, ρ is the bend radius of the spectrograph, Q is the charge of the particle, and p_0 is the central momentum. The constant of proportionality is given by the ratio of the fundamental constants obtained in converting to the units listed and is equal to 3.3356 if p is in units of $\frac{GeV}{c}$, Q is in units of e, B is in Tesla and ρ is in m. E_0 could then be determined by using the relativistic relation for energy and momentum and equation 3.13.

The program COSY INFINITY [53] was used to calculate the transfer matrix for the S800 spectrograph. Experimentally, the quantities measured are in the focal plane. Therefore, an inverse transfer map that relates measured quantities in the focal plane to the parameters at the target was needed. The inversion procedure is beyond the

scope of this thesis and is described in [54]. The inverted transfer matrix, Eqn. 3.11,

$$\begin{bmatrix} \theta_i \\ y_i \\ \phi_i \\ \delta_i \end{bmatrix} = R \begin{bmatrix} x_f \\ \theta_f \\ y_f \\ \phi_f \end{bmatrix} \tag{3.14}$$

related the quantities measured in focal plane to the target quantities of interest.

Ion Chamber

Immediately following the CRDCs, the beam particles passed through an ionization chamber. The ion chamber (IC) was designed to measure the energy loss as the beam particles ionize the gas in the detector by sampling the signal generated along sixteen anode strips. The gas used was P10, which is comprised of 90% argon (Ar) and 10% CH_4 (methane). As with the CRDCs, the response of the individual strips was not exactly uniform; therefore, they were gain matched using the same procedure detailed for the CRDCs. Finally, the pressure in the detector depended on the type of window used on the detector. The windows used for this work allowed a pressure of 140 $Torr$.

Scintillators

The second set of four detectors were plastic scintillators made of BC-408. As a particle passed through the BC-408 plastic, some amount of light was generated and then passed from the scintillator through the light guide and into a photo multiplier tube (PMT) where the amount of light collected by the detector was converted into an electric signal. PMT's are located on the top and bottom of the scintillator. The total energy deposited in the detector was estimated by

$$E_i = \sqrt{E_i^{Up} \times E_i^{Down}}. \tag{3.15}$$

This function gave a more symmetric peak shape, thereby giving a slight increase in the resolution of the detector rather than an alternative form estimated by

$$E_i = \frac{\sqrt{(E_i^{Up})^2 + (E_i^{Down})^2}}{2}. \tag{3.16}$$

In order from first to last, with respect to the beam, the scintillators were labeled E1, E2 and E3. E1, E2 and E3 are 3mm, 5cm and 10cm thick, respectively. These detectors were used to provide timing, energy loss and total energy. Timing was taken from E1. The timing response for the 10 cm detector was measured to be 160 ps FWHM for a beam of 60 MeV/u ^{16}O [51]. This timing information is used for three main purposes. First, it is used to calculate the drift time for the CRDC's, which was 0-20 μs [52] depending on the location of the ionization site and the drift voltage. Second it is used in conjunction with another timing signal, which may come from another scintillator upstream or the cyclotron RF to obtain a particle time of flight (TOF). Third, it is used to provide a start for the data acquisition.

3.3.3 Data Acquisition

The new, high-performance "NSCL data acquisition system" software[1] developed at the NSCL by Ron Fox *et. al.* [55] was used. The recent upgrades at the NSCL coupled with new and upgraded detector systems, highlighted the need for a new data acquisition system capable of handling the increased data rates. In addition to the potential for high data rate experiments, there was also a need for flexibility in the software for handling the changes in detector systems from experiment to experiment. These needs were addressed by combining the object oriented performance of C++ with a scripted user interface via the Tcl/Tk scripting language [56]. Detailed information on the data acquisition software can be found at "http://docs.nscl.msu.edu/daq/overview/".

[1]The data acquisition software has no special name associated with it. However, most people refer to it as "SpecTcl" which is, in fact, just the name for the data analysis component.

3.4 Data Analysis

3.4.1 Data Reduction

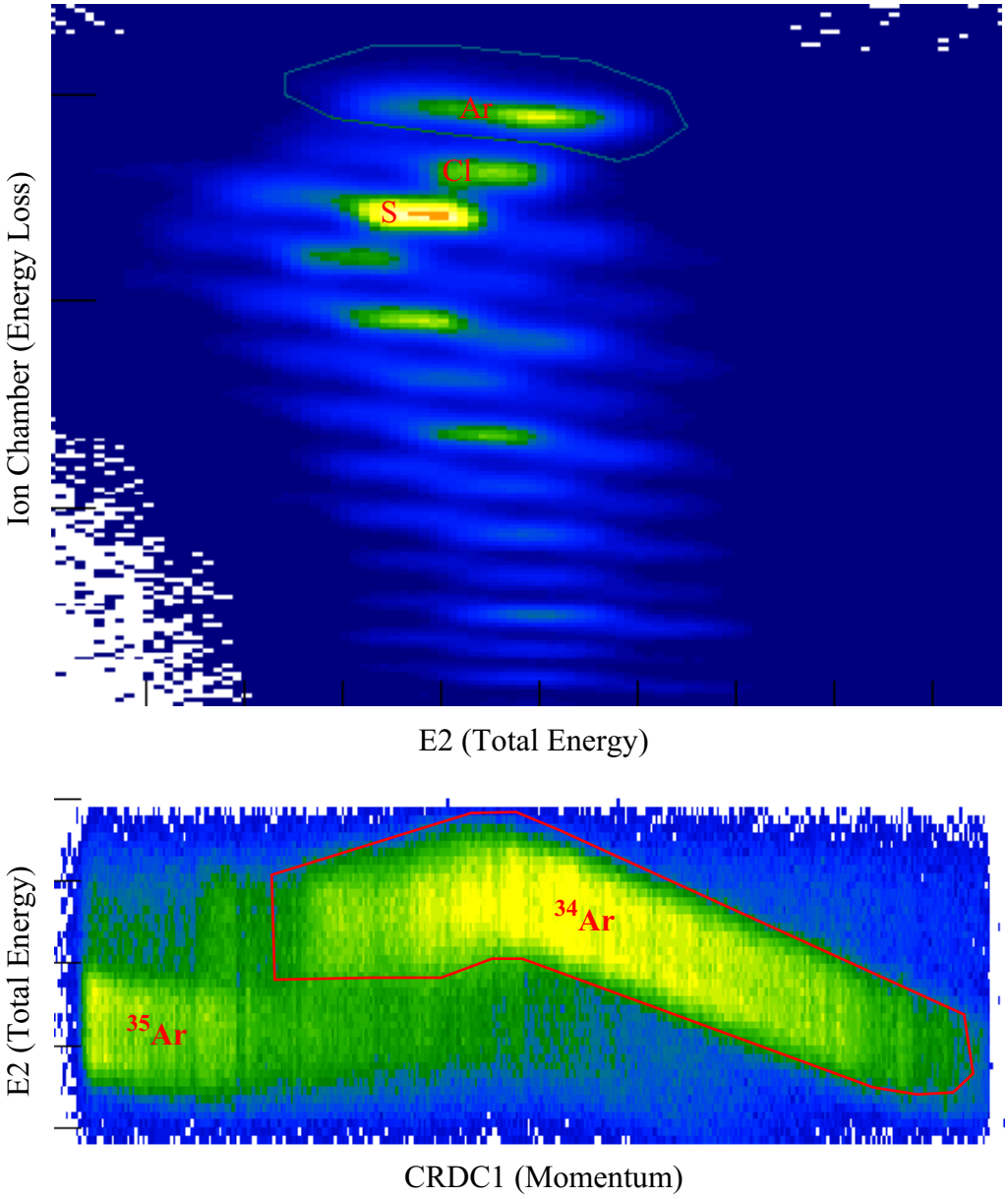

Figure 3.11: 9-bit by 9-bit particle identification spectra with gates. The top figure was used to separate argon. The bottom spectra was used to separate isotopes of Argon. The shape of the E2 distribution is due to the nonlinear response of the photo tube readout method for the plastic.

The secondary beam production process creates many isotopes. In particular, the

secondary beam for this experiment contains an admixture of ^{34}Ar, ^{33}Cl and ^{32}S. Therefore, positive identification of the isotope of interest from the others that enter the focal plane of the S800 was necessary. The S800 was set to center the ^{33}Ar in the focal plane. The unreacted ^{34}Ar was removed with a beam blocker after checking its position in the focal plane to verify that the S800 was set correctly. Unique particle identification was then possible using time of flight (TOF), energy loss, total energy and momentum of the particles. The first selection was made by looking at energy loss vs. total energy, see Fig. 3.11. This selection allowed the separation of one element from another. Once the isotopes of Argon were identified, we then needed to separate ^{33}Ar from the ^{34}Ar. This was done by examining energy loss vs. the CRDC1 position, which roughly corresponded to momentum, see Fig. 3.11. A final gate was applied to the particles so that an AND gate of these two gates gave a positive particle identification of the ^{33}Ar isotope. The choice of particle ID method was determined by the relative efficiency of the detectors used. The CRDC2 detector had a higher efficiency than CRDC1, which was higher than the efficiency of the coincidence of the beam line scintillators used to calculate the TOF. Therefore, by using CRDC2, roughly twice as much data could be used for analysis. Initially, PID using CRDC1, CRDC2 and TOF were all compared and cross checked to ensure that there was no change in the data from method to method, with the exception of the change in the number of counts due to the aforementioned change in efficiencies. The check was performed by examining the Doppler corrected gamma ray spectra for any changes in the number or quality of the peaks. For example, if a PID gate was too large, then contamination peaks from nearby nuclei showed up in the spectra.

3.4.2 Level Diagram Construction

In order to properly assign the energies, spins and parities of excited states of ^{33}Ar, it was necessary to work out in detail the gamma ray decay scheme from the experimental data. Fig. 3.12 shows the observed gamma ray spectrum measured in coincidence with an ^{33}Ar in the S800 focal plane with several peak energies displayed.

All of the peaks shown in Fig. 3.12 were initially assumed to be the result of single transitions and the energies and intensities were determined. Tab. 3.3 gives the energies and intensities with one sigma errors for the gamma rays extracted from the data.

E_γ keV	ΔE_γ keV	I_γ	ΔI_γ
437	3	2	0.3
639	2	< 1	
1084	4	< 1	
1359	2	100	14
1556	8	5	0.7
1798	2	82	12
2005	5	3	2
2097	5	2	1
2460	2	47	7

Table 3.3: Energies and intensities of ^{33}Ar γ radiation derived from coincidence data.

To sort out how the gamma rays presented in Tab. 3.3 fit together, several pieces of information were considered. Three main sources of information were available: Calculated and experimental spectroscopic factors [6]; the previous mass measurement of ^{33}Ar by Nann *et. al.* [57]; and the structure and decay scheme of the neutron rich mirror to ^{33}Ar, ^{33}P.

The measurement by Nann *et. al.* found excited states of ^{33}Ar at 1.34 MeV and 1.79 MeV. Similarly, the isobar ^{33}P has states at 1.4316 MeV and 1.8476 MeV. This information strongly suggests that the 1.359 MeV and 1.798 MeV states correspond to the previous measurement states in ^{33}Ar, as well as, the analog states in the isobar.

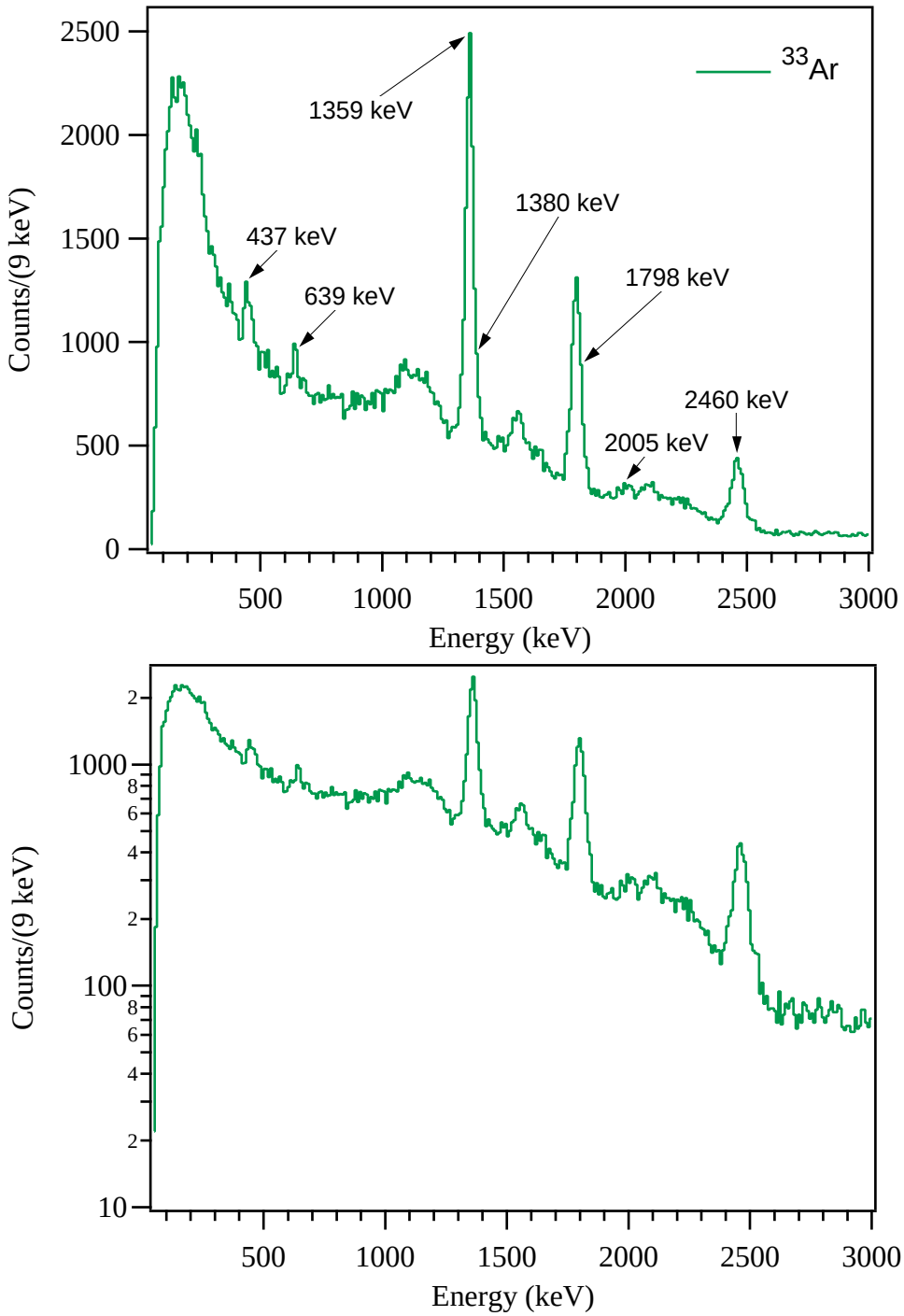

Figure 3.12: ^{33}Ar gamma-ray spectra. The upper plot displays the spectra, with several marked energies, on a linear scale. The lower plot displays the same spectra with a logarithmic scale.

However, to be completely sure, the intensities of these two states against the one neutron removal spectroscopic information were checked. Fig. 3.4 gives the measured spectroscopic factors for the one proton removal from ^{34}S to the ^{33}Ar isobar ^{33}P which agree with the calculated one neutron removal spectroscopic factors for ^{34}Ar to ^{33}Ar.

J^π	Excitation Energy MeV	C^2S
$3/2^+$	1.43	0.68
$5/2^+$	1.85	1.20
$3/2^+$	2.54	<0.01
$3/2^+$	3.28	0.14
Proton	Threshold	Q = 3.34 MeV
$5/2^+$	3.49	0.34
$5/2^+$	4.05	1.35
$5/2^+$	5.05	1.73

Table 3.4: One neutron removal spectroscopic factors for ^{34}Ar.

The fourth $J^\pi = 5/2^+$ state is dominated by proton decay, [6], so it cannot be observed by this technique. Therefore, the only other possibility for a strong gamma ray that could complicate the assignment of the 1359 and 1798 keV gamma rays is the third $J^\pi = 5/2^+$ state. In order to rule out any competing nearby gamma rays, the decay scheme for the ^{33}P isobar was used as a guide. The decay scheme for the ^{33}P isobar indicated there was a gamma ray from the de-excitation of the third $J^\pi = 5/2^+$ state that would be apart of the 1359 keV peak. However, the intensity would have been too weak to noticeably influence the centroid determination. Therefore, the unambiguous assignment of the 1359 keV peak as the first excited state and the 1798 keV peak as the second excited state was made.

Tab. 3.4 indicates that a strong state near 4 MeV should be populated. The isobar ^{33}P indicated that the decay strength for this $J^\pi = 5/2^+$ state is predominantly via a 2616.1 keV gamma ray to the first excited state. In examining the data, Tab. 3.3 and Fig. 3.12, a prominent peak at 2460 keV was found. Due to fact that this state is a part of a cascade, it should decay in coincidence with the 1359 keV gamma ray.

Gamma gamma coincidence data were determined by means of projecting the gamma ray coincidences for a given energy out of a 2D gamma gamma matrix along both axes and then summing the two projections. The matrix was formed by correlating all of the gamma detectors that had data for a given ^{33}Ar event pair wise. By way of an example; assume that there were 5 detectors, and for a given event, detectors 1,2 and 5 had good gamma ray events, and further, that the detectors are read out by the data acquisition system in the order: 1, 2, 3, 4, 5. The coincidences registered in the gamma gamma matrix would be: (1,2), (1,5), and (2,5). The (1,2) matrix element would represent a point in the matrix with x (column) position equal to the Doppler corrected gamma ray energy of detector 1 and a y (row) position equal to the Doppler corrected gamma ray energy of detector 2. If the efficiency for the detection of a single gamma ray is represented as x, then the efficiency for the detection of two gamma rays in a cascade is approximately x^2. Therefore, as the detection efficiency of the detector array is approximately 1%, the gamma gamma matrix contains roughly a factor of 100 less data than the spectrum shown in Fig. 3.12.

The gamma gamma coincidence data for the 2460 keV, Fig. 3.14, and 1359 keV, Fig. 3.13 were analyzed. The positive cross correlation observed in Figs. 3.13 and 3.14, along with the isobaric information, yielded the assignment of an energy of 3819 keV to the third $J^\pi = 5/2^+$ state.

The 437 keV peak was in excellent agreement with the energy difference between the 1798 and 1359 keV states. Examination of the isobar strengthened the notion that the 437 keV state was a transition between the first $J^\pi = 3/2^+$ and $J^\pi = 5/2^+$. Again, the gamma gamma coincidences were checked. It was found, Fig. 3.13, that the 437 keV peak cross correlated with the 1359 keV state. Additionally, if the 1798 keV state decays via the 437 keV transition to the 1359 keV first excited state, then we did not expect to find the 437 keV in coincidence with the 1798 keV gamma ray. Inspection of the 1798 keV coincidence spectra, Fig. 3.15, showed that this was

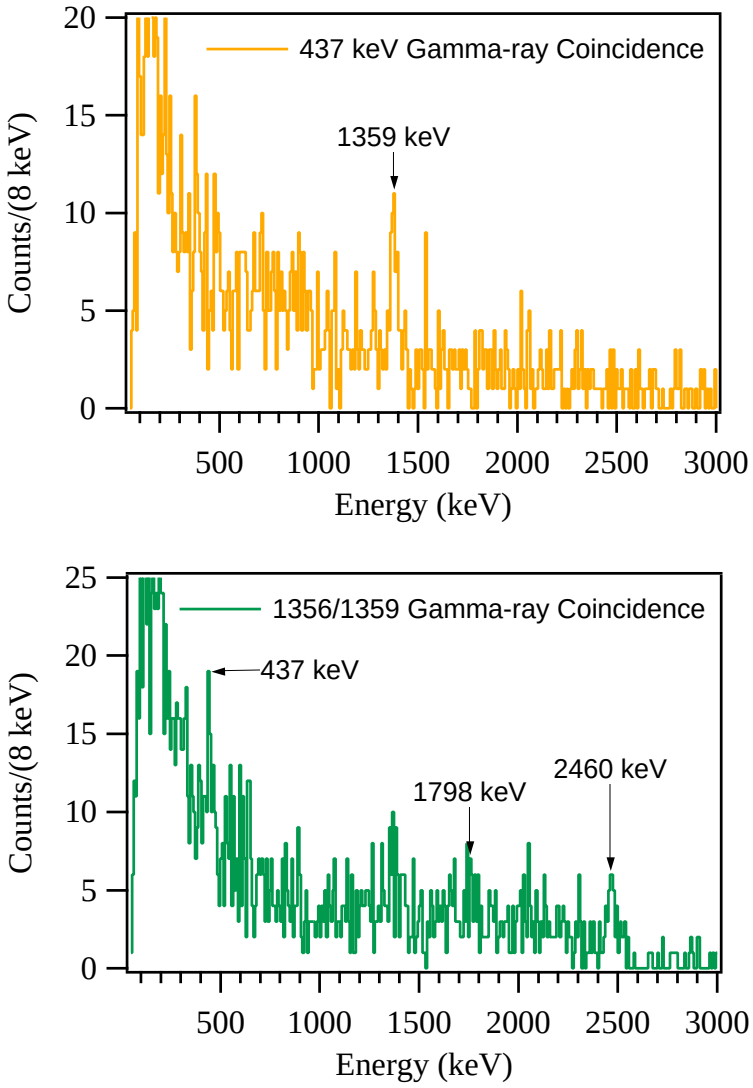

Figure 3.13: ^{33}Ar gamma-ray coincidence spectra for the 437 keV peak is shown in the upper graph. A prominent 1359 keV coincidence was observed. The lower graph displays the 1356 and 1359 keV coincidence gamma rays. 437, 1798 and 2460 keV gamma rays were observed.

indeed the case.

It was noted in the course of examining the coincidence for the 1359 keV gamma ray, Fig. 3.13, that there was weak evidence for a coincidence with the 1798 keV gamma ray. The 1798 keV coincidence spectra was checked, Fig. 3.15, and a state with similar energy to the 1359 keV was present. This led to the conclusion that either there was a 1798 keV feeding the 1359 keV state or visa versa. However, the

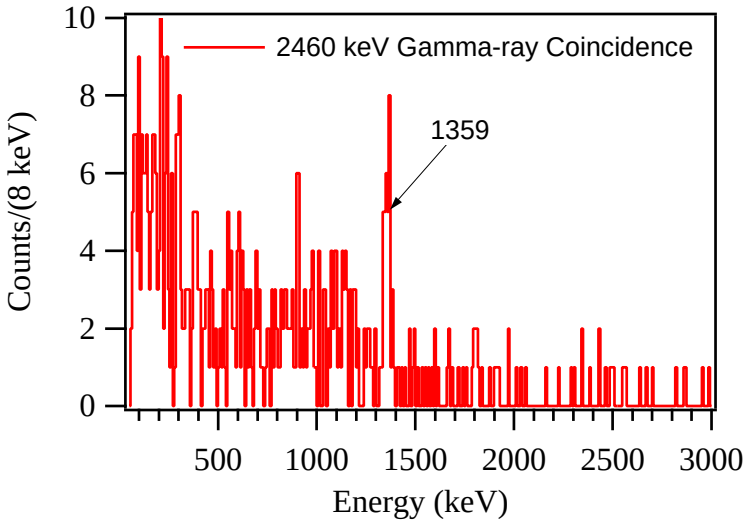

Figure 3.14: ^{33}Ar gamma-ray coincidence spectra for the 2460 keV gamma ray peak. A prominent 1359 keV peak was observed.

energy measured for the 1359 keV state was slightly different, though within errors, due to the low statistics in the coincidence spectra. The isobar was checked and the 1356 keV transition was found to feed the 1798 keV J=5/2 second excited state. This also implied that the 1359 keV peak was not made up of one particular transition, however, the strength of the 1356 keV state is not sufficient to noticeably affect the centroid. Finally, in addition to the validation of the 1356 keV line, we then had a state with an energy of 3154 keV. In comparison with the ^{33}P isobar, the 3154 keV state was assigned a $J = 3/2^{+}(5/2)^{+}$.

Further examination of the ^{33}Ar gamma ray spectrum, Fig. 3.12, shows that the Compton background for the 2460 keV peak had two small structures. These peaks were not large enough to show up in the coincidence spectra for the three largest peaks. However, the coincidence spectra for these peaks yielded valuable information. The coincidence spectra for the 2005 and 2097 keV, Fig. 3.16, both showed clear evidence for coincidence with the 1359 keV peak. Because a cross correlation with the 1359 keV coincidence was not possible, it was necessary to check the background spectra by looking at the coincidences of the gamma rays immediately following the

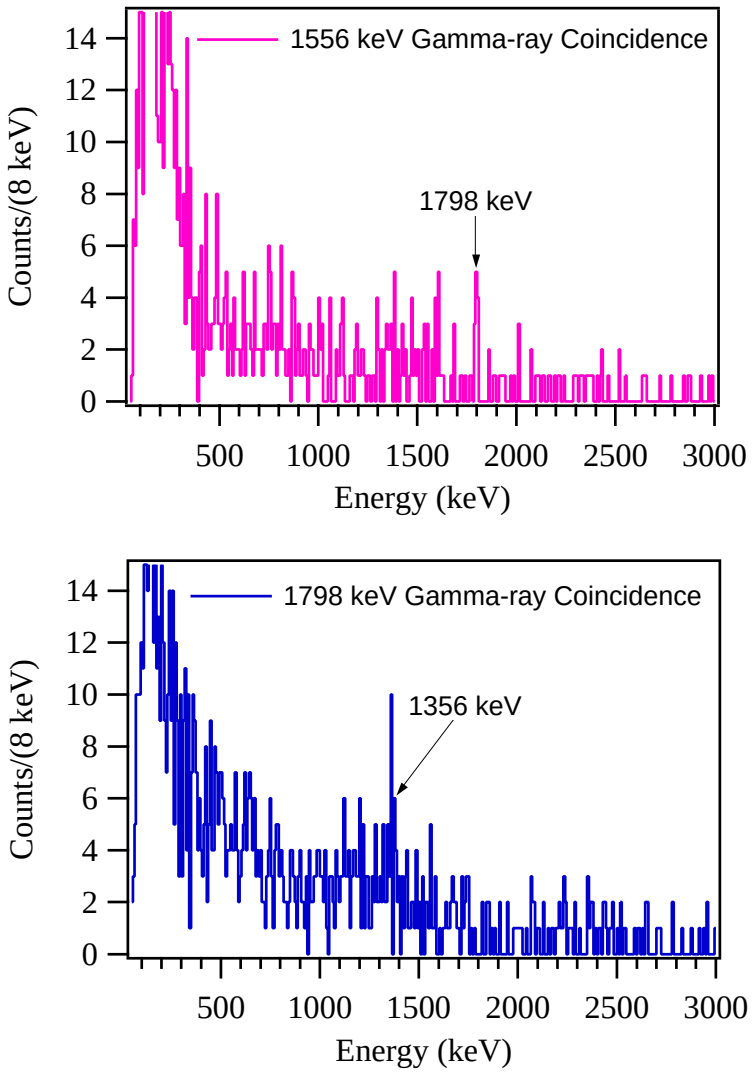

Figure 3.15: ^{33}Ar gamma-ray coincidence spectra.

2005 and the 2097 keV gamma rays as the peaks sit on a wide Compton peak that will also have coincidence with the 1359 keV gamma ray. The background verified that the 2005 and 2097 keV peaks were in coincidence with the 1359 keV first excited state. We then had evidence for two proton unbound states at 3364 and 3456 keV, corresponding to the 2005 and 2097 keV gamma rays, respectively.

Examination of the mirror, ^{33}P, showed that the 3364 keV should also have transition to the 1798 keV second excited state. Careful inspection of the Compton peak revealed that indeed there was evidence for this transition. However, due to the posi-

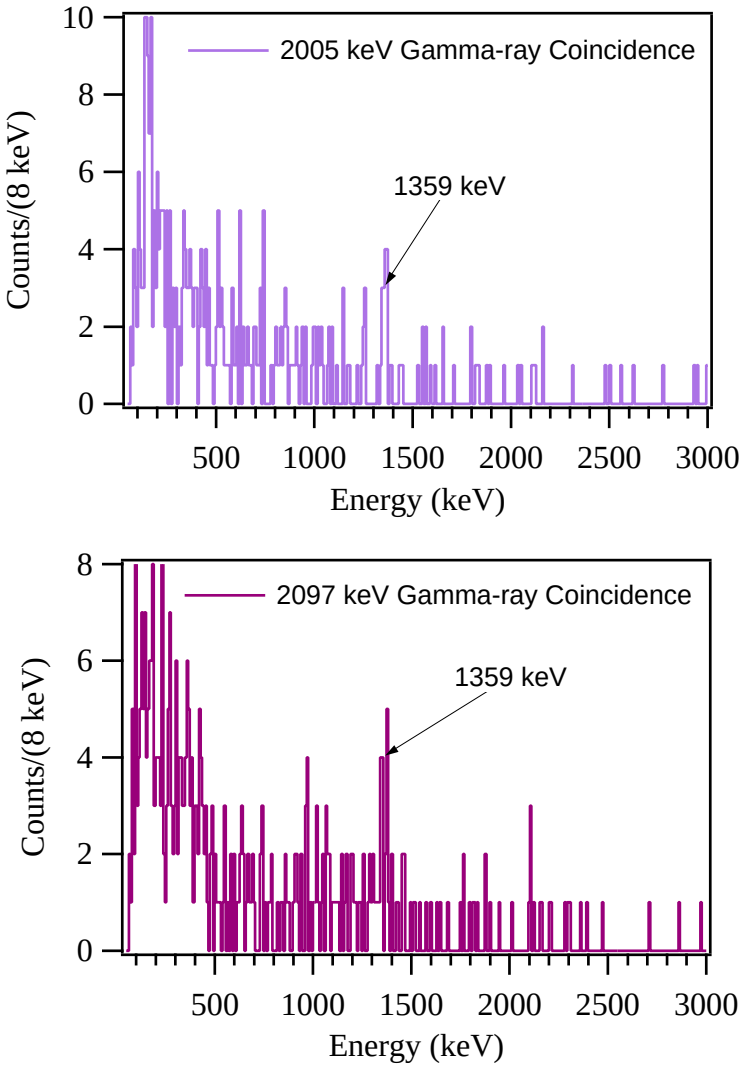

Figure 3.16: ^{33}Ar gamma-ray coincidence spectra for the 2005 and 2097 keV gamma rays. The upper, 2005 keV gamma ray, coincidence spectra as well as the lower, 2097 keV gamma ray, spectra show coincidence with the 1359 keV peak greater then their respective backgrounds.

tion of the potential peak, the exact nature of the Compton peak had to be studied. The analysis of the Compton peak resulting from the strong 1798 keV peak used in the calculations of the efficiencies above, showed that their was indeed an excess of counts at the potential peak position. A fit of the peak energy verified that the energy did indeed fit for the transition being considered. As a final check, the coincidence spectra for the 1556 keV peak, Fig. 3.15, was examined. Fortunately, because the

1556 keV peak sits on the Compton background for the 1798 keV peak, there is no chance for self coincidence in this case. As seen in Fig. 3.15, the 1556 keV peak was found to have the correct coincidence. As a final check, the intensities were compared with the isobaric analogs in ^{33}P and the agreement was verified.

Similarly, for a check of the 3364 keV state, the mirror nucleus was checked. It was further discovered that, in addition to the 2097 keV gamma ray transition from the $J^{\pi} = 7/2^{+}$ 3456 keV state, there should also be a weaker transition to the 1798 keV state. Examination of the ^{33}Ar spectra showed a small peak located early in the rise of the Compton peak from the 1798 keV peak. The energy and intensity of the state, 1651 keV, matched the corresponding isobaric analog states. However, because the state was so weak and gamma gamma coincidence could not be verified, this transition was considered likely, but not certain.

The peaks at 639 keV and 1084 keV are marginally statistically significant. However, the energies match perfectly to those expected from a second $J^{\pi} = 3/2^{+}$ state at 2439 keV in ^{33}Ar. The 639 and 1084 keV decay from this state go to the known 1798 and 1359 keV states.

The above analysis formed a coherent picture of the level structure of the ^{33}Ar nucleus. The states identified were summarized, Tab. 3.5. The gamma ray relationship found was formulated as a level diagram, Fig. 3.17.

The level diagram for ^{33}Ar had two notable issues that could not be resolved. The first issue observed was an unidentified 1380 keV transition from the 3819 keV state to the 2439 keV state. Unfortunately, there was no chance to observe this gamma ray as it was part of the dominant 1359 keV gamma ray peak. The second issue was the unobserved 2439 keV transition to the ground state from the second J=3/2 state. Again, given the presented evidence, it was part of the much stronger 2460 keV transition. Both states would have had about 5 units of intensity relative to the 1359 keV gamma decay intensity, Fig. 3.17.

E_γ keV	δE_γ keV	I_γ	δI_γ	Mult.
437	3	2	0.3	E2/M1
639	2	<1		E2/M1
1084	4	<1		E2/M1
1356	8	2	0.3	E2/M1
1359	2	100	14	E2/M1
1556	8	5	0.7	M1/E2
1798	2	82	12	E2/M1
2005	5	3	2	E2/M1
2097	5	2	1	
2460	2	47	7	E2/M1
3154	9			
3364	6			
3456	6			
3819	4			

Table 3.5: Characteristics of ^{33}Ar γ radiation. The intensities are given relative to the 1359 keV γ-ray intensity. Transition type, Mult., is based on shell model calculations [6] where the dominant transition is given first. The $7/2^+$ state is not in the sd shell and therefore were not included in the shell model calculations. The displayed uncertainties were calculated at the one sigma confidence level.

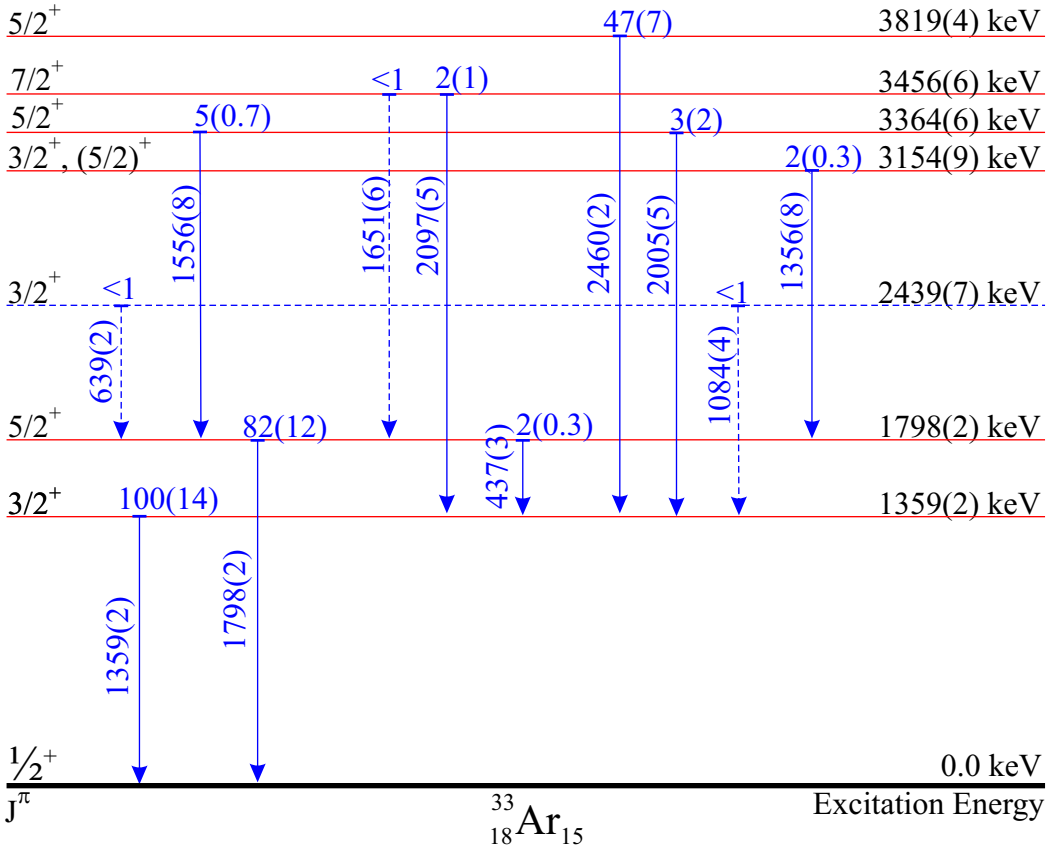

Figure 3.17: ^{33}Ar level diagram.

Chapter 4

Isobaric Multiplet Mass Equation

The isobaric multiplet mass equation (IMME) empirically quantifies a relation between masses of isobaric analogs to the z-axis projection of their isospin. Isospin symmetry in nuclei results in the success of the quadratic form of the IMME in describing the mass difference between isobars. It was originally proposed by Wigner in 1957 and was reviewed by W. Benenson and E. Kashy [58]. The A=33 isospin quartet, of which ^{33}Ar is a member, was reviewed originally in [57] and more recently in [7] based the precise measurement of the ^{33}Ar ground state. This thesis provides new information on the comparison of the quartets which include the first two excited states of ^{33}Ar. The present measurements are much more precise than the previous values.

We may express the IMME mathematically as

$$ME = a + bT_z + cT_z^2 + dT_z^3. \tag{4.1}$$

If isospin symmetry is valid, the d coefficient should be zero. The quality of the agreement of the quadratic form of the IMME with measurements can only be tested by precise measurements. That the form of the equation is indeed quadratic can be investigated case by case and has been done in [58] and for several cases subsequently,

e.g. in the $A = 23, 27\,; T = 3/2$ quartets by J.A. Caggiano [52]. For this thesis the necessity of the addition of a cubic term was examined for the $A = 33\, T = 3/2$ isobaric quartet with the first $J^\pi = \frac{3}{2}^+,\ \frac{5}{2}^+$ states. No higher lying states could be examined because the corresponding states in ^{33}P and ^{33}Cl, which have large excitation energies, $> 6MeV$, are not known.

The 1359 keV state in ^{33}Ar is a member of the $T = 3/2\,; J^\pi = \frac{3}{2}^+$ first excited state quartet. The mass excesses of this quartet as a function of isospin was fit to equation 4.1 to determine the coefficients of the IMME. The masses for the ^{33}P, ^{33}S, ^{33}Cl nuclei were taken from [7], except for ^{33}Ar which is based on the ground state measurement presented in [7] and this work. The thesis measurement provides the excitation energies of the states relative to the ground state. However, the mass excess of the ground state, presented in [7], must be known in order to determine the mass excess of the excited states. The data used are given in Tab. 4.1. As noted in [7]

Nucleus	T_z	$ME_{exp}(MeV)$ $J^\pi = \frac{3}{2}^+$
^{33}P	+3/2	-24.9061(11)
^{33}S	+1/2	-19.6812(30)
^{33}Cl	-1/2	-14.0207(30)
^{33}Ar	-3/2	-8.0229(50)

Table 4.1: Mass excesses of the $J^\pi = \frac{3}{2}^+$ members of the first excited state quartet for $A = 33$ from [7] and this work.

this quartet requires a cubic form. The measurements of this work did not change the apparent inability of the quadratic form of the IMME to adequately describe this case. However, also mentioned in [7], there is an issue with the level assignment of the state in ^{33}Cl. Therefore, one cannot be sure that the apparent breakdown of the IMME is due to something peculiar about the $A = 33\, T = 3/2$ system. In fact, examining the evaluated nuclear structure data file [59] (ENSDF) database one finds that the neighboring 6.945(2) MeV state has a $(3/2^+, 5/2^+)$ J^π assignment. The state is not listed as a $T = 3/2$ isospin state but the level width is unknown so it was chosen as a

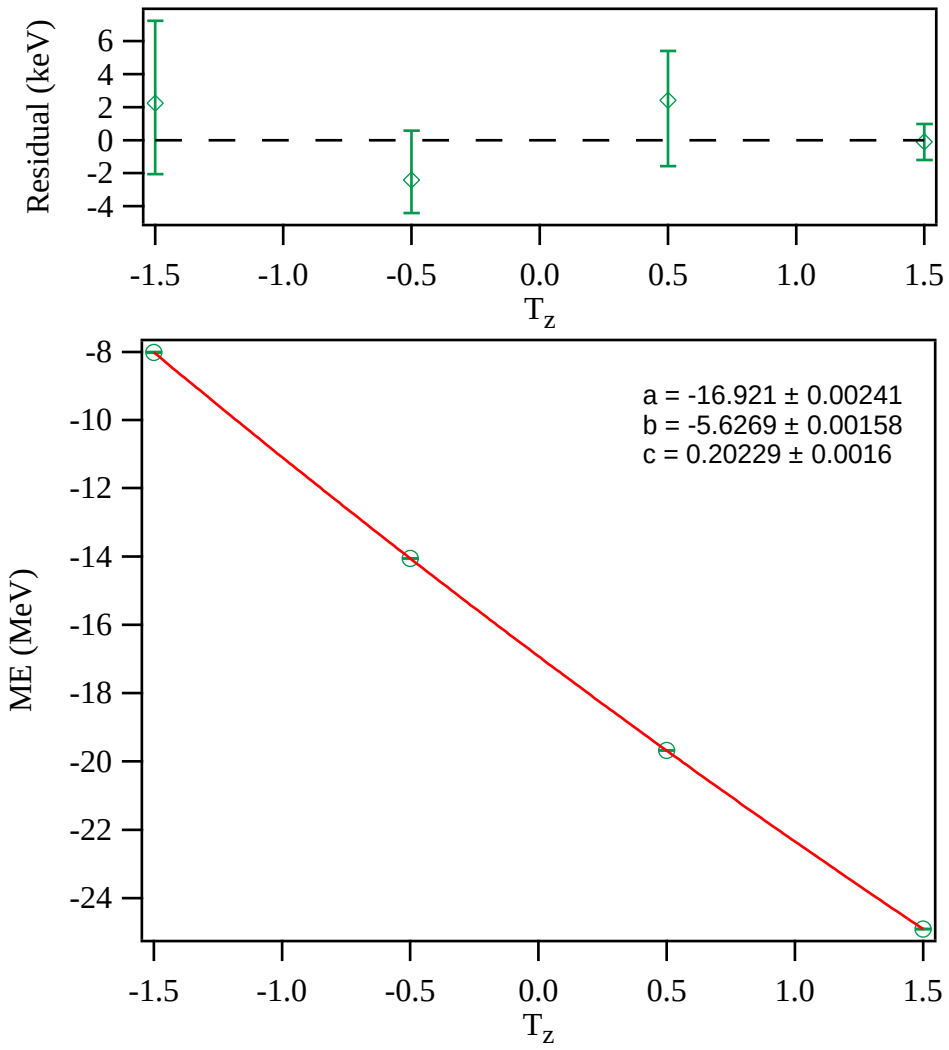

Figure 4.1: The lower figure demonstrates the $J^{\pi} = \frac{3}{2}^{+}$ $T = \frac{3}{2}$ mass excesses of the members of the $A = 33$ isobaric quartet as a function of isospin. The circles in the lower figure are the data points and the line is the quadratic fit to the data the coefficients of which are shown in the text box. The upper figure shows the fit residuals with error bars showing the uncertainty in the masses.

possible candidate. We assume that this is the correct isospin member, as was done in Tab. 4.2. The results from the fit of this data are shown in Fig. 4.1. The result of this fit are in much better agreement with a quadratic IMME. The cubic term for this fit was, $-2.82 \pm 2.29\ keV$. In [58] the impact of the masses of the $T_z = \pm 1/2$ members energies were shown to be three times that of the other two. Therefore, this result must be considered tentative until the uncertainty in the level assignment for

Nucleus	T_z	$ME_{exp}(MeV)$ $J^\pi = \frac{3}{2}^+$
^{33}P	+3/2	-24.9061(11)
^{33}S	+1/2	-19.6812(30)
^{33}Cl	-1/2	-14.0591(30)
^{33}Ar	-3/2	-8.0229(50)

Table 4.2: Recommended mass excesses of the $J^\pi = \frac{3}{2}^+$ members of the first excited state quartet for $A = 33$.

this state in ^{33}Cl can be resolved. Fortunately, there was no known issues with the level assignments for the $J^\pi = \frac{5}{2}^+$ $T = \frac{3}{2}$ member of the quartet.

The results of the fitting for the quadratic form of the IMME for the $J^\pi = \frac{5}{2}^+; T = \frac{3}{2}$ second excited state members of the quartet is shown in Fig. 4.2. The residuals, Fig. 4.2, show the agreement between the data and the predictions of the IMME. The cubic term for this case is consistent with zero, and has a value of $-0.6 \pm 2.4\ keV$. This state was previously measured [57] and therefore provides opportunity to analyze the change in the predictions of the IMME for the two cases, Tab. 4.3. In comparing

Nucleus	T_z	$ME_{exp}(MeV)$ $J^\pi = \frac{5}{2}^+$
^{33}P	+3/2	-24.4901(11)
^{33}S	+1/2	-19.2492(40)
^{33}Cl	-1/2	-13.6126(20)
^{33}Ar	-3/2	-7.5839(50) [this work]
^{33}Ar	-3/2	7.596(20) [57]

Table 4.3: Mass excesses of the $J^\pi = \frac{5}{2}^+$ members of the second excited state quartet for $A = 33$.

the results for the $J^\pi = \frac{5}{2}^+; T = \frac{3}{2}$ members of the quartet the authors [7, 57, 58] also found that the cubic term was consistent with zero. The notable change is in the change in the magnitude of the cubic term between the present work and Ref. [7] which quoted a cubic term of 2.6(4.0) keV.

The result of the measurements presented in this work show that the quadratic form of the IMME agrees well for the $J^\pi = \frac{5}{2}^+$ excited state and potentially for the

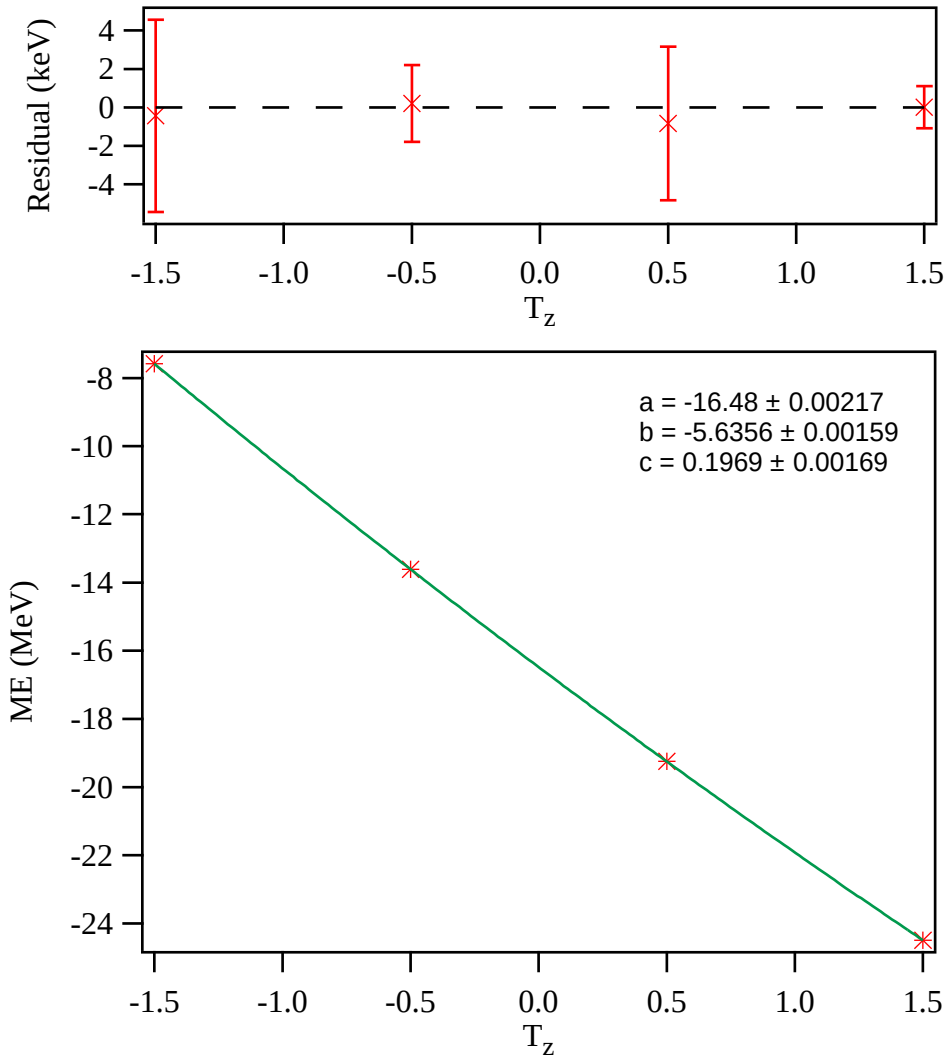

Figure 4.2: The lower figure demonstrates the $J^\pi = \frac{5}{2}^+$ $T = \frac{3}{2}$ mass excesses of the members of the $A = 33$ isobaric quartet as a function of isospin. The circles in the lower figure are the data points and the line is the quadratic fit to the data the coefficients of which are shown in the text box. The upper figure shows the fit residuals with error bars showing the uncertainty in the masses.

$J^\pi = \frac{3}{2}^+$ state. The ground state case was not considered as it was not measured. However, in [7] the ground state of ^{33}Ar was measured. However, at the time of publication for [7] it was not known that the first $T = 3/2$ state in ^{33}Cl was in err. Fortunately, a measurement was performed since [60] and the corrected first $T = 3/2$ state in ^{33}Cl gives excellent agreement [60] with the IMME prediction. Future experiments on the structure of the ^{33}P and ^{33}Cl, $T = 3/2$ states would be

useful as higher lying states could be examined. The $J^\pi = \frac{3}{2}^+$ $T = 3/2$ state in ^{33}Cl could also be resolved with experiment.

Chapter 5

Astrophysical Consequences of ^{33}Ar Measurement

5.1 Introduction

Proton capture reactions for nuclei near the proton drip line are characterized by small Q values and low level densities. Therefore, statistical model calculations for these nuclei are not applicable. Instead, the reactions must be calculated by means of summing individual nonresonant and resonant contributions. However, resonant proton capture rates depend exponentially on the resonance energies of the relevant particle unbound states. Thus, precise determinations of the relevant energy levels for these nuclei are an essential input to the rate calculations.

In this thesis we precisely measured almost all of the states of astrophysical interest for calculation of the ^{32}Cl(p,γ)^{33}Ar rate. At temperatures greater than or equal to $3 \times 10^8 K$ the ^{32}Cl(p,γ)^{33}Ar rate is considered a bottleneck for rp process reaction flow. In particular the ^{32}Cl(p,γ)^{33}Ar rate is one of three rates that influence the break out from the SCl cycle [61]. The new information on the important states was used to recalculate the ^{32}Cl(p,γ)^{33}Ar rate as a function of temperature. A comparison of

the new results with the original rates based on shell model predictions in [61] for the ^{32}Cl(p,γ)^{33}Ar rate was performed and the results presented below.

5.2 Reaction Rate Calculation Details

The derivations, and assumptions therein, for calculation of the nonresonant and resonant proton capture rates are detailed in many texts; see for example [1, 62]. Therefore only a summary of the relevant equations [61] given here.

5.2.1 Nonresonant Capture Rate Calculation

The nonresonant proton capture rate $N_A < \sigma\nu >_{nr}$ was calculated with the formula

$$N_A < \sigma\nu >_{nr} = 7.83 \times 10^9 (\frac{Z}{AT_9^2})^{\frac{1}{3}} S(E_0)[MeV\ b] exp(-4.29[\frac{Z^2 A}{T_9}]^{\frac{1}{3}}) \tag{5.1}$$

where A is the reduced mass in u given by $A = \frac{A_p A_T}{A_p + A_T}$; A_p is the mass of the proton and A_T is the mass of the target; T_9 is the temperature in GigaKelvin and Z is the proton number of the target nucleus. The total S factor was calculated from

$$S(E_0) = \sum_i \sigma_i C^2 S_i E_0 exp(2\pi\eta). \tag{5.2}$$

where E_0 is the optimum bombarding energy, and η is the Sommerfeld parameter. The spectroscopic factors $C^2 S_i$ were obtained by shell model calculations [6] and the single particle cross sections σ_i were scaled with excitation energy directly from those calculated in [61].

5.2.2 Resonant Capture Rate Calculation

The resonant capture rate $N_A < \sigma\nu >_{res}$ was calculated from the standard form

$$N_A < \sigma\nu >_{res} = 1.54 \times 10^5 (AT_9)^{\frac{-3}{2}} \omega\gamma[eV] exp(\frac{-11.605 E_r[MeV]}{T_9}) \tag{5.3}$$

where A, T_9 are as in the nonresonant case and E_r is the resonance energy which is given by E_r = *Excitation Energy - the proton separation energy*. The resonance strength is

$$\omega\gamma = \frac{2J+1}{2(2J_T+1)} \frac{\Gamma_p \times \Gamma_\gamma}{\Gamma_{Total}} \tag{5.4}$$

where J_T is the spin of the target, J is the spin of the resonance state, Γ_p is the proton width, and Γ_γ is the gamma width. Γ_p and Γ_γ were determined [6] from shell model calculations and the measured excitation energies.

5.3 New ^{32}Cl(p,γ)^{33}Ar Rate

A new ^{32}Cl(p,γ)^{33}Ar rate was calculated employing the formalism presented in the previous section. There were ten rates summed to give the total ^{32}Cl(p,γ)^{33}Ar rate. The resonance energy of eight of the ten states was based on this thesis' measurement. For each state, six rates were calculated: the maximum and minimum rate given the uncertainties in the excitation energy of the state, and the recommended rate for both the shell model calculations presented in [61] and this thesis.

The first five rates are nonresonant proton captures to the $J^\pi = \frac{1}{2}^+$ g.s., $J^\pi = \frac{3}{2}^+$ 1359 keV, $J^\pi = \frac{5}{2}^+$ 1798 keV, $J^\pi = \frac{3}{2}^+$ 2439 keV, and $J = \frac{3}{2}$ 3154 keV states. These rates were in turn summed to give the total contribution to the nonresonant capture rate (NR) shown in Fig. 5.1. All six rates representing the recommended,

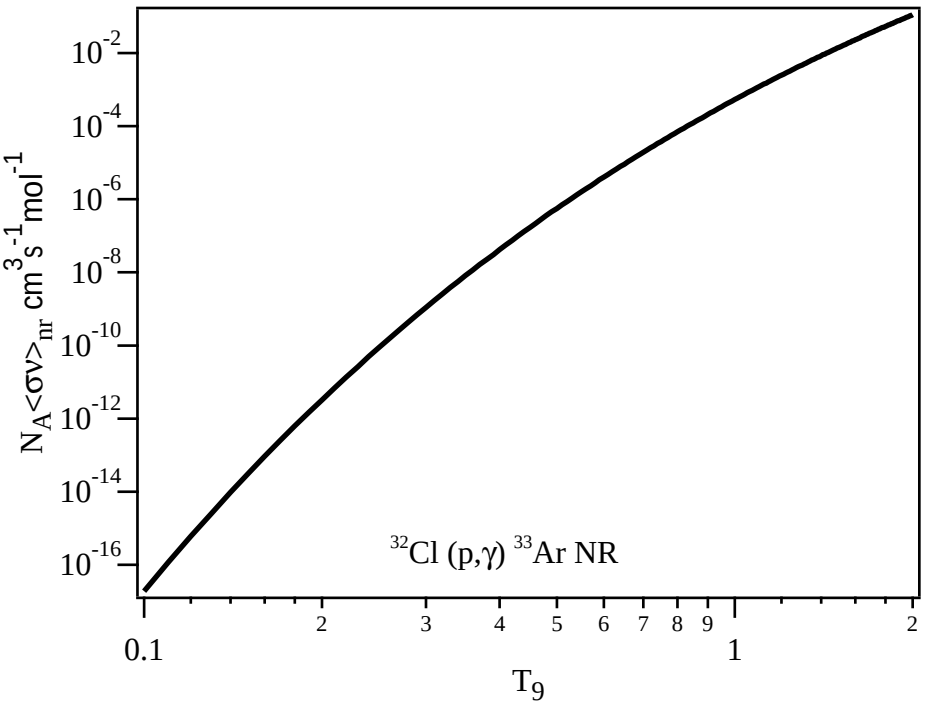

Figure 5.1: Total nonresonant capture rate. The recommended and possible maximum and minimum rates for the shell model calculations and this thesis were also calculated. The differences in these six rates are not noticeable on this scale.

maximum and minimum rates possible within the uncertainties in the shell model and this thesis were calculated. Due to the relative insensitivity of the parameters to changes in excitation energy only one line appears to be visible in the figure.

The first $J^{\pi} = \frac{5}{2}^{+}$ 3364 keV proton unbound state's, contribution to the total rate was calculated and is displayed in Fig. 5.2. The $J^{\pi} = \frac{5}{2}^{+}$ state's rate within

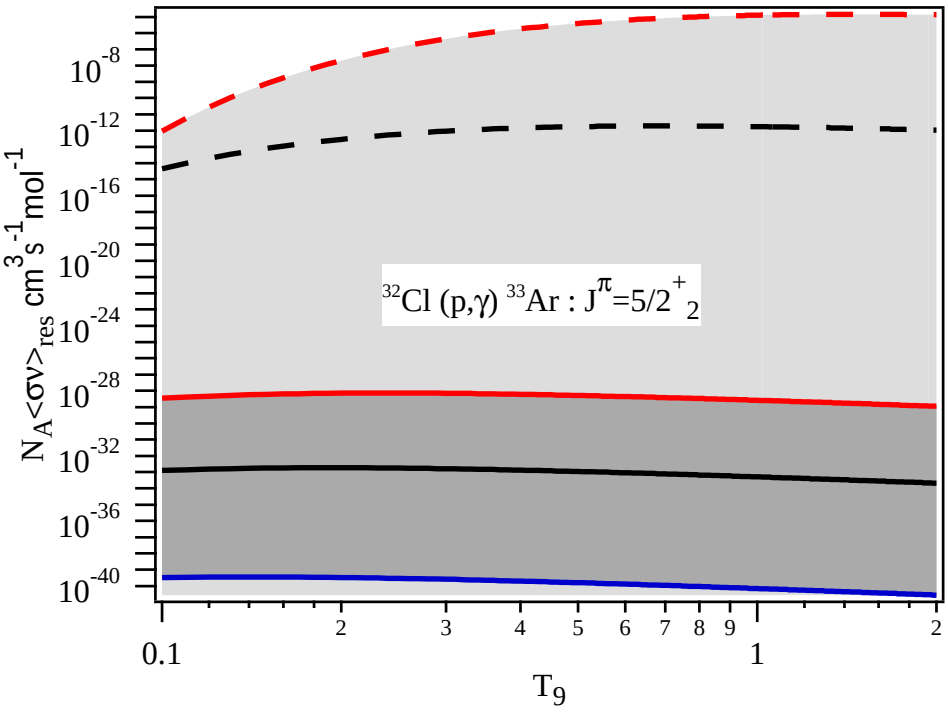

Figure 5.2: Rates possible within uncertainties for proton capture to the second $J^{\pi} = \frac{5}{2}^{+}$ 3364 keV state. The dashed lines correspond to shell model calculation rates and the solid lines to the rates based on this thesis. The red lines show the maximum rate possible within uncertainties while the blue lines shows the minimum rate possible with uncertainties. The blue dashed line corresponding the minimum shell model rate is not shown as it is approximately zero. The black line is the recommended excitation energy rate.

uncertainty was found to be somewhat different than the others in the sensitivity of the rate to changes in the resonance energy. This results from proximity of this state to the proton separation energy. The rate determined here is much lower than the previously recommended rate partly because of the dramatic change in the proton width as a function of excitation near the proton separation threshold and partly due to the lower resonance energy. Both effects are exponential and therefore the product of the two effects resulted in the dramatic change in the reaction rate. In fact, a rate below 10^{-24} will not contribute a noticeable effect in network calculations. Therefore,

we find that this state does not contribute to the overall ^{32}Cl(p,γ)^{33}Ar rate.

The second $J^{\pi} = \frac{7}{2}^{+}$ 3456 keV unbound state's, proton capture rate was calculated and shown in Fig. 5.3. Fig. 5.3 demonstrates the need for precise measurements, due to the extreme sensitivity of the rate to resonance energy.

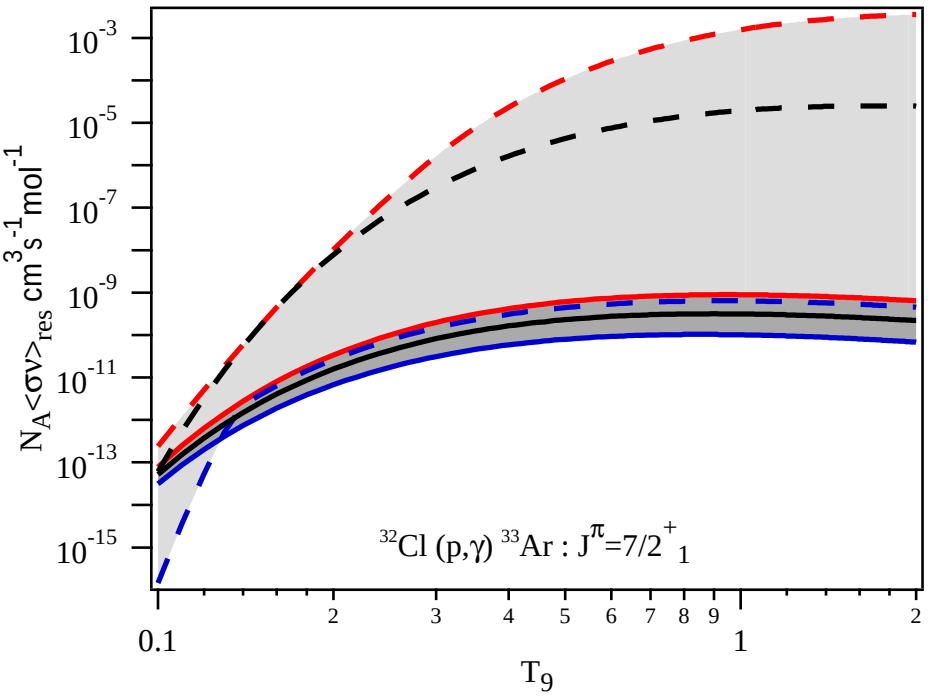

Figure 5.3: Rates possible within uncertainties for the second $J^{\pi} = \frac{7}{2}^{+}$ 3456 keV state. The dashed lines correspond to shell model calculation rates and the solid lines to the rates based on this thesis. The red lines show the maximum rate possible within uncertainties while the blue lines shows the minimum rate possible with uncertainties. The black line is the recommended rate.

The rate for the third and last proton unbound state, $J^{\pi} = \frac{5}{2}^{+}$ 3456 keV, measured in this thesis was calculated and is shown in Fig. 5.4. Fig. 5.4 shows that the rate derived from this thesis is now higher than the shell model rate despite the larger resonance energy of the shell model states. This effect demonstrates the sensitivity of resonance energy and temperature in the Gamow peak.

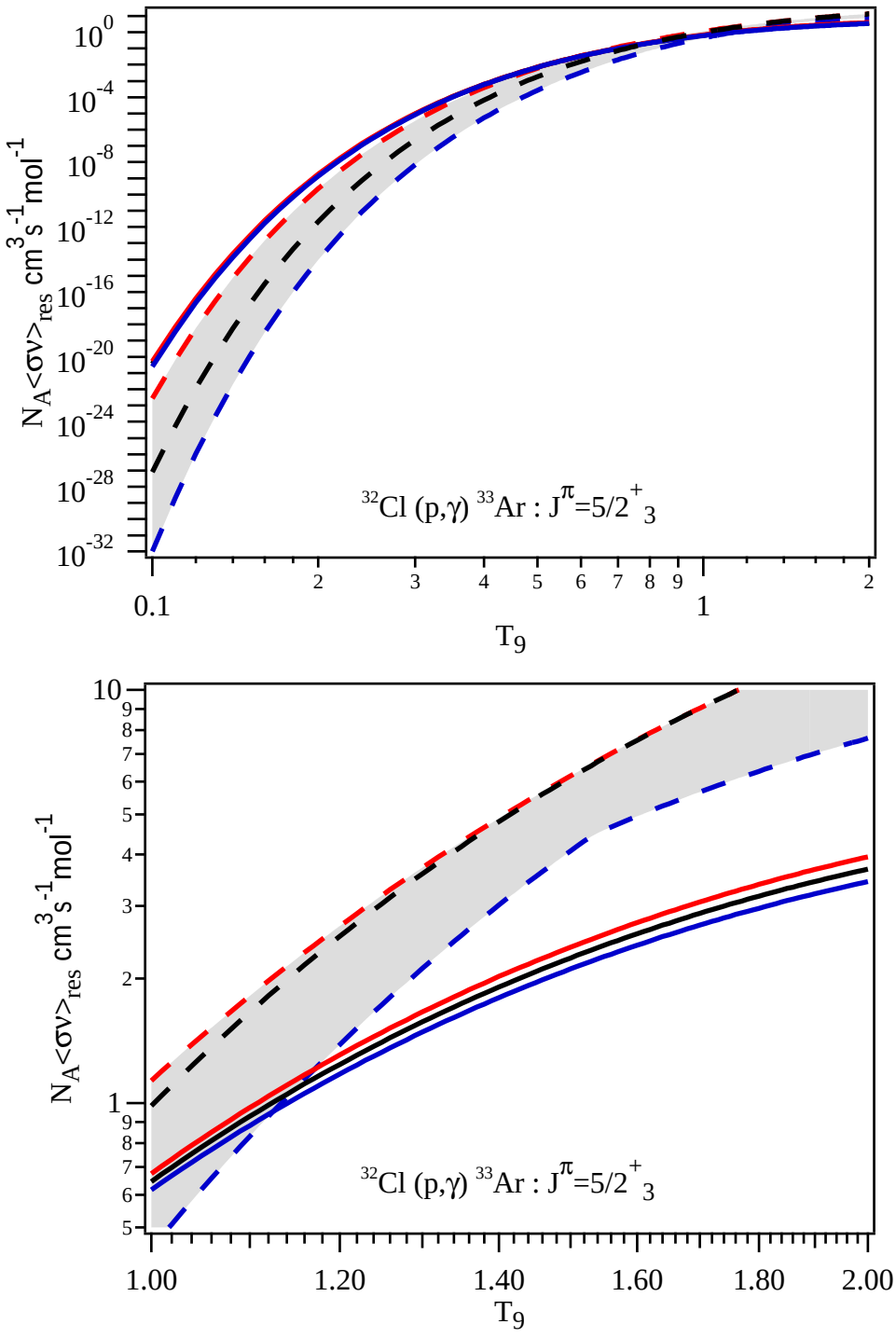

Figure 5.4: Two views of the same rates possible within uncertainties for the third $J^{\pi} = \frac{5}{2}^{+}$ 3819 keV state. The lower figure demonstrates the changes in the two sets of rates that take place above 1 GigaKelvin. The dashed lines correspond to shell model calculation rates and the solid lines to the rates based on this thesis. The red lines show the maximum rate possible within uncertainties while the blue lines shows the minimum rate possible with uncertainties. The black line is the recommended excitation energy rate.

The last two states, $J^{\pi} = 1/2^{+}$ 4190 keV, and $J^{\pi} = 3/2^{+}$ 5010 keV, used in the rate calculation were not observed in the experiment presented in this thesis. Their rates are shown in Fig. 5.5. The nonobservation was due to the large proton widths of these states. The large proton width implies that these two states decay via particle emission and therefore must be measured with another experimental technique, one of which was performed and will be briefly mentioned in the conclusions chapter.

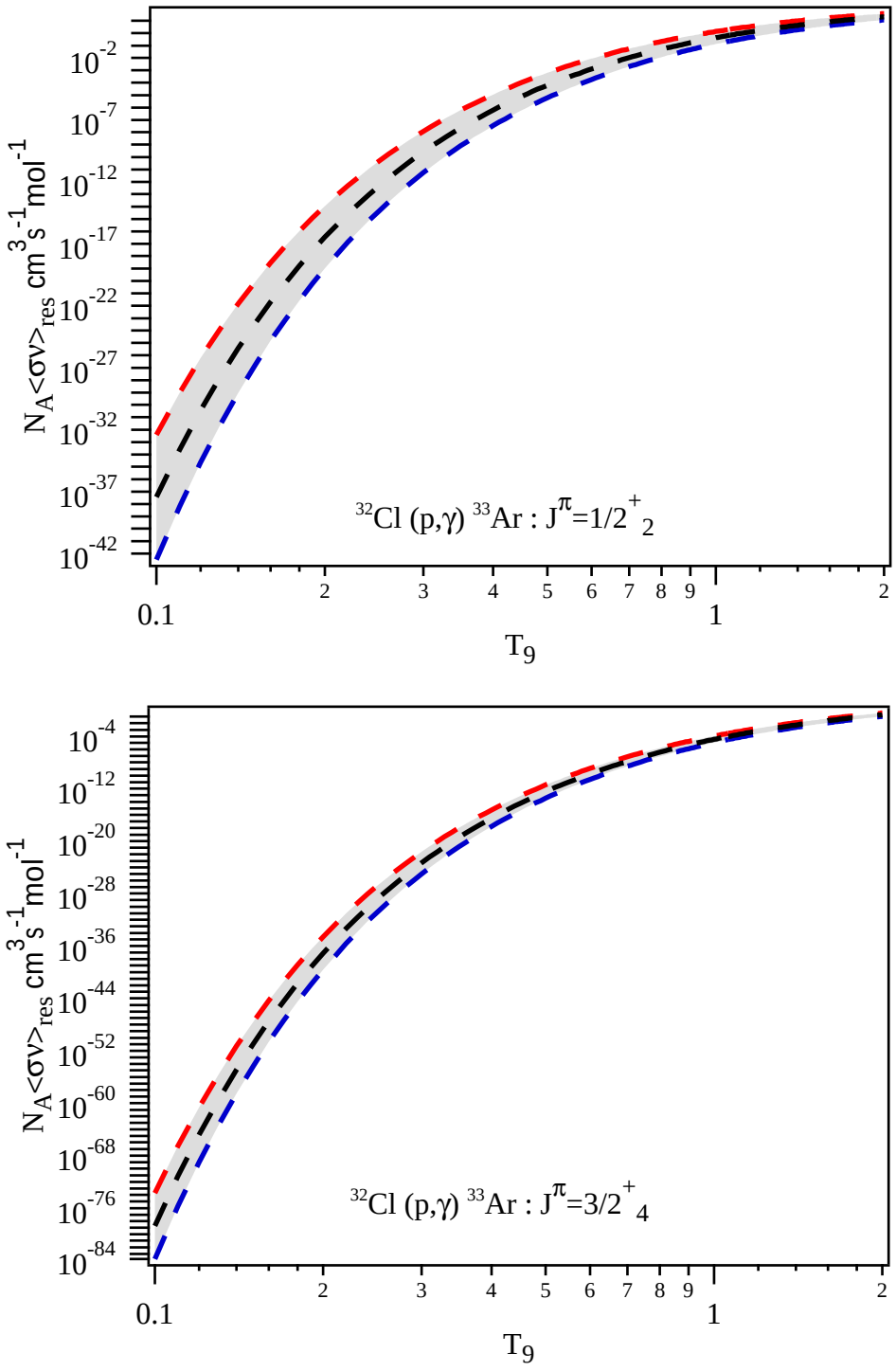

Figure 5.5: The dashed lines correspond to shell model calculation rates. The red lines show the maximum rate possible within uncertainties while the blue lines shows the minimum rate possible with uncertainties. The black line is the recommended rate.

In Fig. 5.6 the second $J^\pi = 1/2^+$ state was shown to dominate the rate at a temperature near 2 GigaKelvin and is the same order of magnitude of the second $J^\pi = 3/2^+$ at 1 GigaKelvin. A measurement of the second $J^\pi = 1/2^+$ could have a

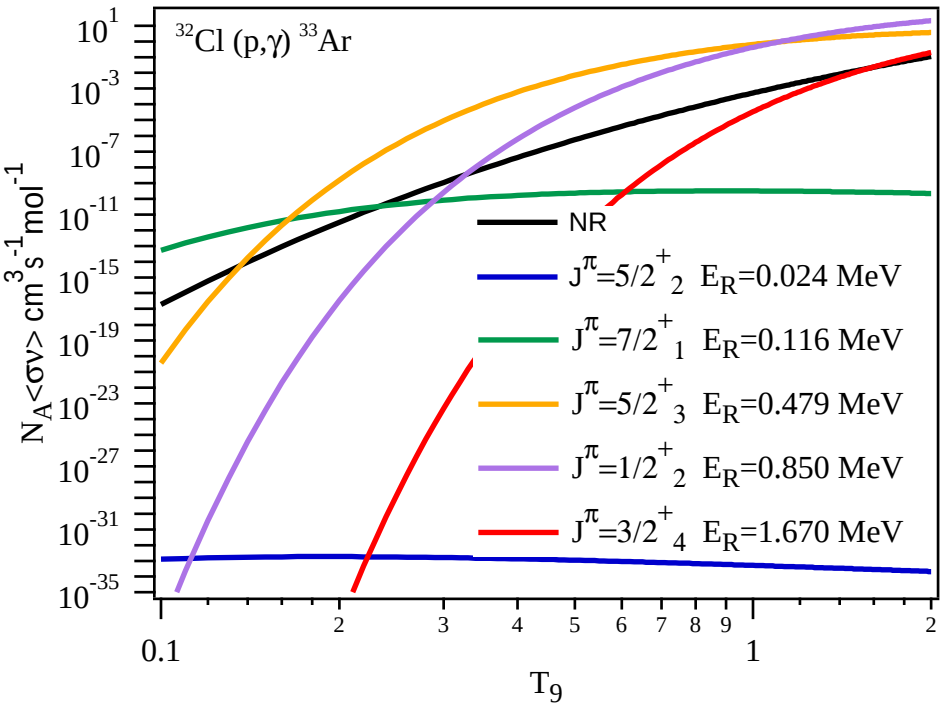

Figure 5.6: The six sets of rates that when summed comprise the total rate for this thesis's recommended values.

significant effect on the total rate.

Fig. 5.7 displays the changes in the total reaction rate based on the recommended, maximum and minimum excitation energies for the thesis and the shell model calculations.

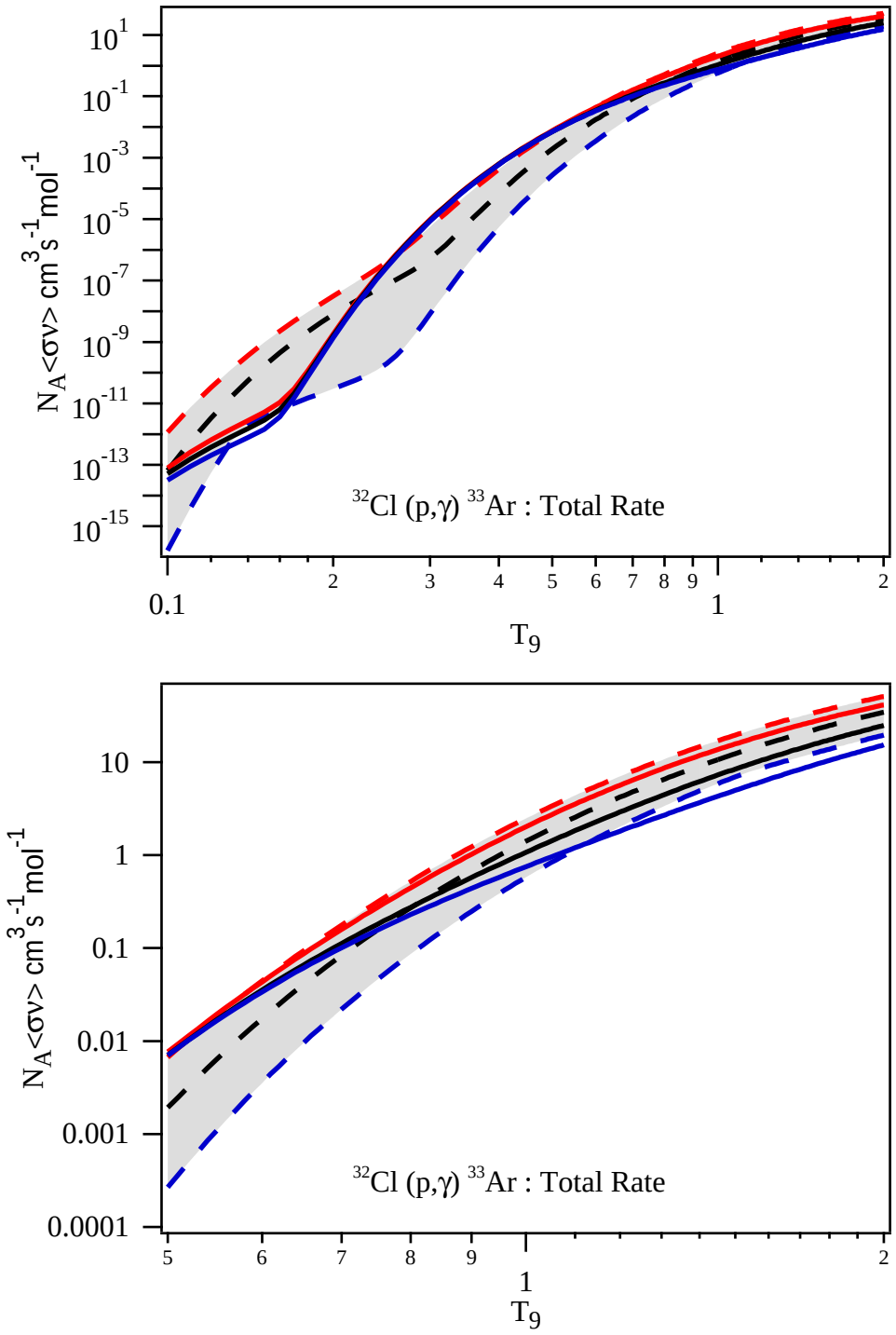

Figure 5.7: The upper figure demonstrates the total rate over the range of interest to the astrophysical environments relevant to this thesis. The lower figure shows the behavior of the rates above 1 GigaKelvin. The dashed lines correspond to shell model calculation rates and the solid lines to the rates based on this thesis. The red lines show the maximum rate possible within uncertainties while the blue lines shows the minimum rate possible with uncertainties.

It is informative to compare the new rate and the rate found in [61] based on shell model calculations of the level energies. In order to compare the change in the total rate based on this thesis and [61] the ratio of the two rates were plotted in Fig. 5.8. As can be seen in the figure the ratio between the two calculations, the black line,

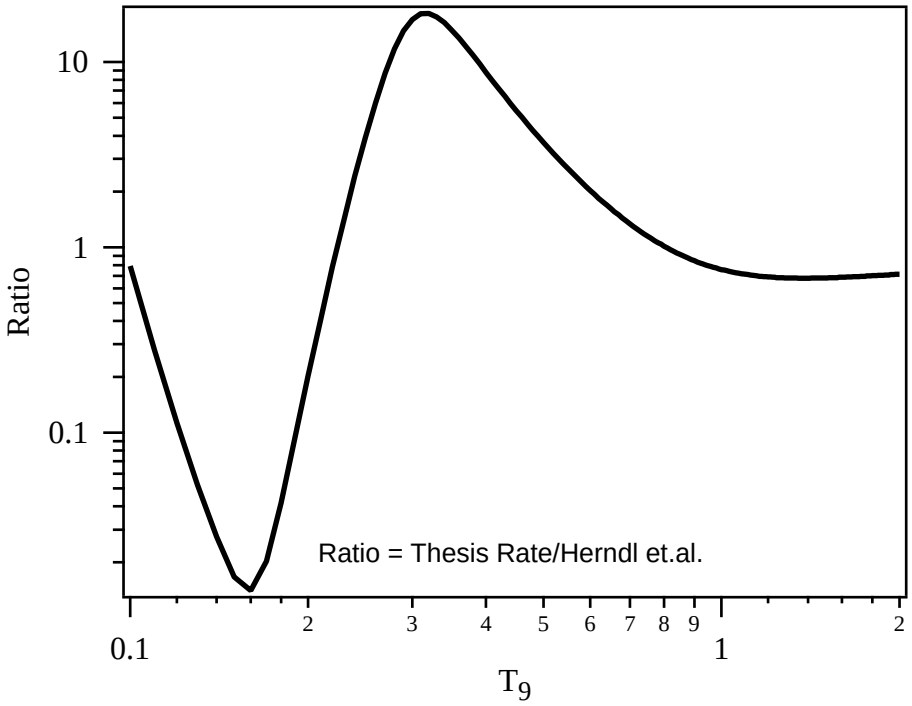

Figure 5.8: The black line is the ratio of the thesis rate and the Herndl *et.al.* shell model rate.

varies by almost two orders of magnitude. However, of import is the difference in the rates at $3 \times 10^8 K$. The rate based on this thesis is almost and order of magnitude larger than the previous rate, an effect that could have important consequences for break out of the SCl cycle. So that this effect can be studied by network calculations, as was done in chapter 2, a new recommended rate was calculated and is provided in Tab. 5.1.

Table 5.1: This thesis' recommended ^{32}Cl(p,γ)^{33}Ar rate.

T_9	$N_A < \sigma\nu >_{TotalRate}$ $cm^3 s^{-1} mol^{-1}$
0.1	5.22931×10^{-14}
0.15	2.82566×10^{-12}
0.2	1.58126×10^{-9}
0.3	9.04902×10^{-6}
0.4	0.000606841
0.5	0.00706596
0.6	0.0353019
0.7	0.112094
0.8	0.274652
0.9	0.5729
1	1.06841
1.5	8.43877
2	24.745
2.5	45.8912
3	67.7258
3.5	88.3837
4	107.637
4.5	126.087
5	144.682
6	186.555
7	241.415
8	316.276
9	416.773
10	547.28

Chapter 6

Conclusions and Outlook

6.1 Conclusions

Understanding *rp* process nucleogenesis is a significant challenge requiring a combination of observation, models and input data. In this thesis a combination of new theoretical predictions and experimental techniques were presented to help improve the accuracy of the *rp* process models and subsequently our understanding of the *rp* process. The results will allow a more meaningful comparison of models and observation.

A study of the effects of nuclear mass was carried out in the region A = 41 – 75 within the framework of a Type I X-ray burst model. The results indicated that without further improvement in theoretical or experimental nuclear inputs, in particular nuclear masses, tight constraints on ignition conditions in Type I X-ray bursts could not be made. However, the results do support previous predictions that the *rp* process in the A = 64 – 72 mass region slows down considerably leading to extended burst tails. It was also found, using a 0.35 - 0.45 hydrogen mass fraction, that even for the largest slow downs, which correspond to the lowest proton capture Q-values, that the *rp* process still reached the SnSbTe cycle. The result is model

dependent, of course, but shows that as the amount of available hydrogen increases, so does the length of the burst and, consequently, the length of the burst tail timescale. Therefore, it was concluded that long burst timescales are a result of large amounts of hydrogen and can, therefore, be interpreted as a signature of the *rp* process. The above *rp* process work was found to only be applicable in the model for hydrogen mass fractions greater than approximately 0.3, as the *rp* process path will not reach the A = 60 – 72 mass region for smaller hydrogen mass fractions.

In response to the need for improved nuclear physics inputs for *rp* process calculations, a new experimental technique was developed for precise measurement of the excited states of neutron deficient nuclei. The NSCL was recently upgraded by the coupling of the K500 and K1200 superconducting cyclotrons. This upgrade allowed for the production of the necessary energetic, intense primary beams needed to produce rare isotope beams of sufficient intensity for measurements of nuclei near the proton drip line. Further, the newly constructed SeGA detector [45] paired with the upgraded S800 spectrograph allowed for gamma ray spectroscopy of rare isotope beams. The (p,d) transfer reaction, in inverse kinematics, was chosen as a means for additional removal of one neutron from an already proton rich radioactive beam to reach the neutron deficient isotopes relevant to the *rp* process. The use of a polypropylene target further enhanced the available cross section for neutron removal by neutron knockout on the carbon in the target. With a secondary beam of ^{34}Ar, the ^{33}Ar nucleus was studied. Prior to this thesis, there was no information available on the excited states of astrophysical interest. As a result of this thesis most of the states relevant to the *rp* process were measured, see Fig. 3.17. With the ^{33}Ar measurement, the ^{32}Cl(p,γ)^{33}Ar astrophysical proton capture rate was calculated. The ^{32}Cl(p,γ)^{33}Ar rate is important to the *rp* process as it is one of three reactions that influence the breakout of the SCl cycle. The new rate was found to be approximately ten times larger than the previous [61] shell model based calculations. This finding may have notable consequences

for breakout of the SCl cycle. The new results were tabulated in Tab. 5.1.

^{33}Ar is a member of the A = 33 T=3/2 isospin quartet. Due to isospin symmetry, an isospin dependent functional form can empirically relate the masses of isospin quartets to each other. The functional form, first derived by Wigner in 1957 [58] is a quadratic function of T_z if isospin symmetry is valid. However, a recent article [7] provided evidence that the A=33 isospin quartet was not well described by a quadratic form. As two of the states measured in this thesis were included in the analysis in [7], a reanalysis of the data was performed. The results of the reanalysis show, in fact, that the quadratic form of the IMME is valid for the two quartets studied here. Here the $J^\pi = 3/2^+$ state in ^{33}Cl, was assumed to be incorrectly assigned, based on the IMME prediction and the recent remeasurement of the first T=3/2 state in ^{33}Cl [60]. A replacement candidate was found that gave good agreement with the IMME. Future experiments will have to resolve this assignment issue.

Finally, the experimental technique detailed in this thesis is limited to states that gamma decay on time scales of $\Delta t < 1ns$. Two of the states thought to contribute to the ^{32}Cl(p,γ)^{33}Ar rate were not observed. These states preferentially decay via particle emission and are, therefore, not amenable to a gamma ray spectroscopy experiment. Therefore, a complimentary technique is needed to measure the excitation energy of these states. In fact, the experiment that is the foundation of this thesis, was one part of two complimentary new techniques attempted. The other experiment performed used the same setup as the experiment detailed in this thesis, as well as the (p,d) transfer reaction, to populate states in ^{33}Ar. However, in the other experiment the S800 was used to measure the deuterons instead of the ^{33}Ar reaction partner. This technique is advantageous because the deuterons carry away the excitation energy information from the reaction independent of the means of de-excitation of the ^{33}Ar nucleus. It is hoped that the analysis of the deuteron data will yield information about the two remaining states of interest, as well as a cross check to the measured states

common to both techniques. A deuteron spectrum, the first ever measured in the S800 spectrograph, is shown in Fig. 6.1. The data were taken during a test experiment, several months prior to the experiment described in this thesis. In the test experiment a primary beam of 150 MeV/u ^{36}Ar was delivered to the target position of the S800. The resulting deuterons from the p(^{36}Ar,d)^{35}Ar reactions were detected in the focal plane of the S800. Unique particle identification for the deuterons was achieved by producing deuterons with the same energy, as in the reaction, in the A1900 fragment separator. The S800 analysis line was set to the deuteron rigidity and the deuterons were delivered to the S800 to characterize the detector response. The peaks shown in Fig. 6.1 correspond to states in ^{35}Ar. The FWHM of the first peak, marked G.S. in Fig. 6.1, was 130 keV and with the number of counts in the peak shown this gives a one sigma uncertainty of approximately 1 keV in the peak centroid determination. The deuteron background, that was originally a major concern for this technique, results from deuterons from carbon–argon fusion evaporation events. As can be seen in the plot, Fig. 6.1, the cross section for the fusion evaporation cross section is of the same order of magnitude as the transfer reaction. Lastly, the shape of the background is due to the acceptance of the S800.

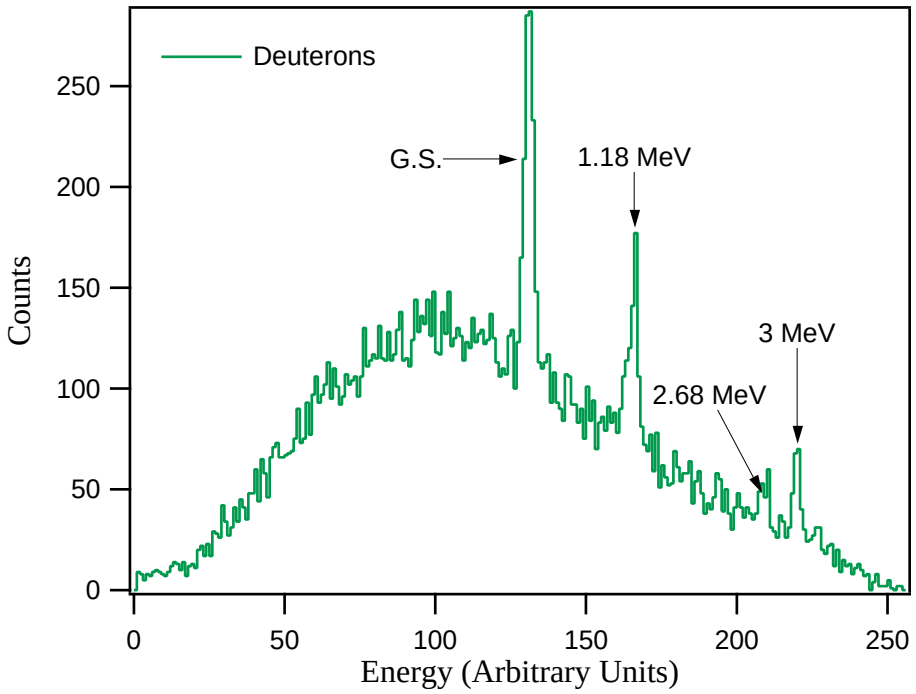

Figure 6.1: Results of a preliminary test run, performed prior to this thesis, where a technique to determine the validity of using relatively low energy, approximately 20 MeV, deuterons resulting from a p(^{36}Ar,d)^{35}Ar reaction @ 150 MeV/u to measure the mass of proton rich isotopes.

6.2 Outlook

The technique developed in this thesis proved to be a good method for measuring the energies of excited states in ^{33}Ar. Further, the capabilities of the technique coupled with the new capabilities of the NSCL's coupled cyclotrons indicate that the reach of the technique may be useful for studying *rp* process nuclei up to the A=80 range. This is an exciting prospect as this technique could help to address many of the nuclear physics input needs discussed in this thesis.

The power of the technique presented in this thesis is in measuring excited states for nuclei that preferentially gamma decay. However, if the ground state mass is unknown then the excitation energies will have the same uncertainty as the ground state mass. Therefore the complimentary technique of measuring the deuterons resulting from the (p,d) reaction is also essential to this process. In fact, this technique was also used to measure the excited states of ^{33}Ar during the experiment that yielded the results presented in this thesis. Further, several experiments in the A = 64 – 73 range are planned for the near future.

Appendix A

Focal Plane Gas Handling System

A.1 Introduction

The focal planes of the S800 Spectrograph [51] and the 4 T Sweeper Magnet [63] have three detectors that require high purity gas. These detectors consist of an Ion Chamber (IC) and two Cathode Readout Drift Chambers (CRDCs). The proper functioning and user operation of these detectors yields several system specifications:

Reliability The system must be able to maintain user specified pressures, flow rates and mixing without failure.

Stability The system must have a controllable, tolerable operational variance in the user specified gas parameters.

User Friendliness The system's control software (driver) must be as clear, intuitive and efficient as possible. The software should be useable by someone familiar with the physical system almost immediately upon inspection.

Fault Tolerance The system and its drivers must handle unforeseen problems as gracefully as possible.

Remote Operation The system must offer full feature remote control and monitoring functionality. Due to safety considerations, users cannot enter the experimental area when beam is present. Therefore, remote operation allows for monitoring and control of the system without loss of valuable beam time.

The initial design of the focal plane gas handling system (FPGHS) was performed by C.I. Freigang *et. al.* [63]. The final design, construction and remote system monitoring and control software was a part of this thesis work and is the most advanced configuration of the MKS hardware currently used. In fact, MKS has expressed interest in obtaining the *LabView* software driver. Since the system documentation is beyond the scope of this thesis (and >50 pages), the FPGHS manual will be produced as a separate document. Therefore, only a limited introduction to the hardware and software has been provided below.

As of January 24th, 2003, the S800 and Sweeper Magnet systems have been built, tested and used during experiments in compliment to the recent upgrade to the new coupled cyclotron facility at the NSCL.

A.2 FPGHS Hardware and Software

Physically, the FPGHS system, is comprised of 6 main components: Gas supply, control box, detectors, pumps, process controller, and software. Three gas cylinders containing research quality gases provide the gas supply. High purity gas regulators regulate the flow from the cylinders. The control box, shown in Fig. A.1, provides mechanical control of the gas flow properties to and from the detectors. Mechanical control of the gas is done by a specific combination of pneumatic valves, mass flow controllers [64] (MFC), pressure transducers [65] (PT), needle valves (fine adjustment), and a static tube mixer. Gas enters the control box from the gas supply (arrows on lower left of Fig. A.1) and is delivered to the detectors (arrows on top of Fig. A.1).

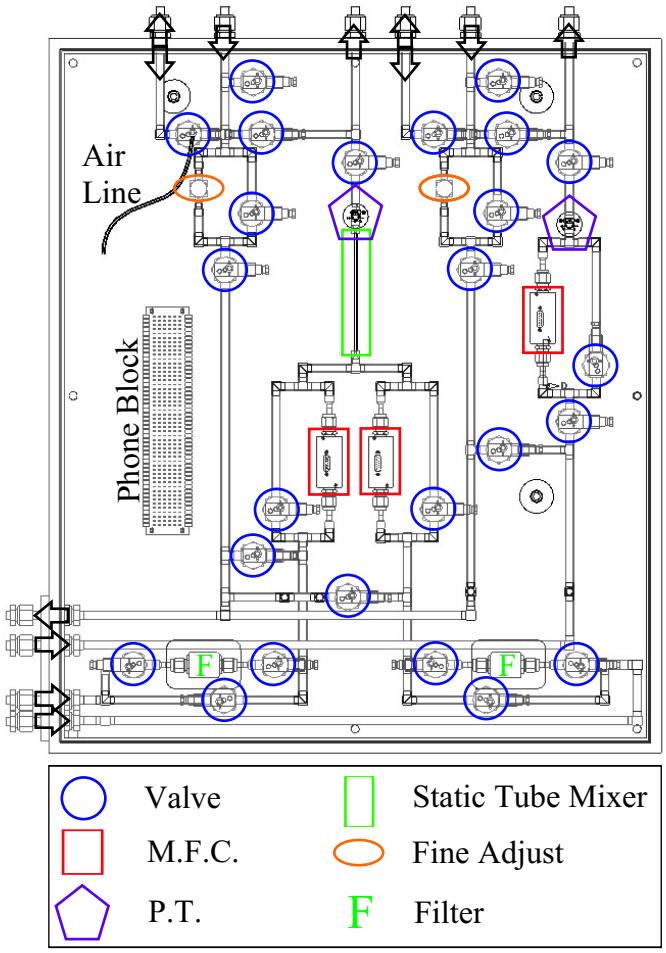

Figure A.1: Mechanical drawing of FPGHS gas handling components. Arrows indicate direction of gas flow.

The gases are removed from the system through the roughing pumps (left pointing arrow on bottom left of Fig. A.1). The control box MFC's and PT's are controlled by the process controller [66, 67].

The process controller settings/system status are controlled/monitored by the *LabView* [68–72] virtual instrument (software driver). An example of the software is shown in Fig. A.2. This particular example is the page an experimentalist would use to change or monitor settings for pressure transducer #1. The *LabView* code associated with this example page for pressure transducer #1 is shown in Fig. A.3.

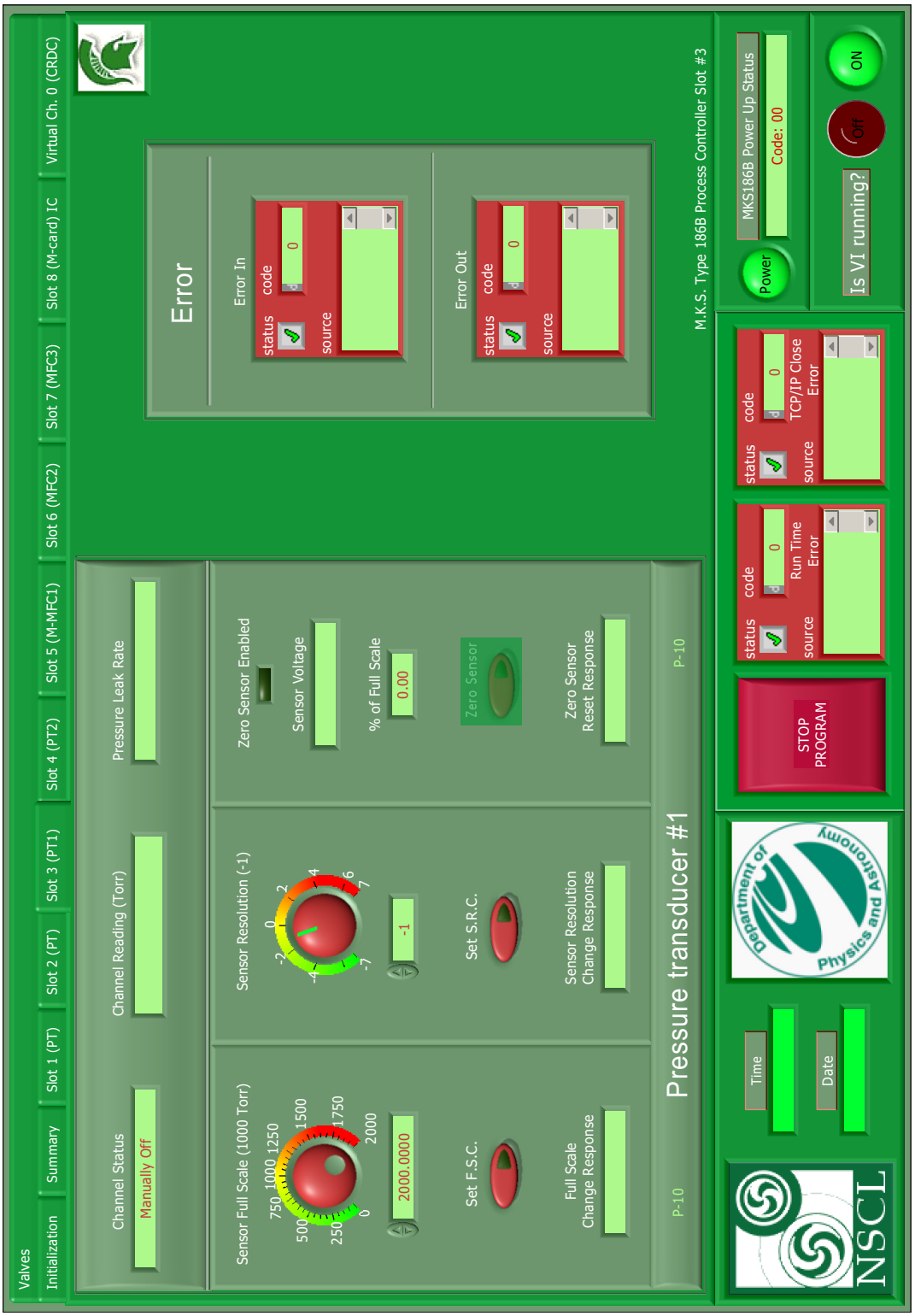

Figure A.2: Pressure transducer #1 page. This page is one of twelve pages an experimenter can use to monitor and control the FPGHS.

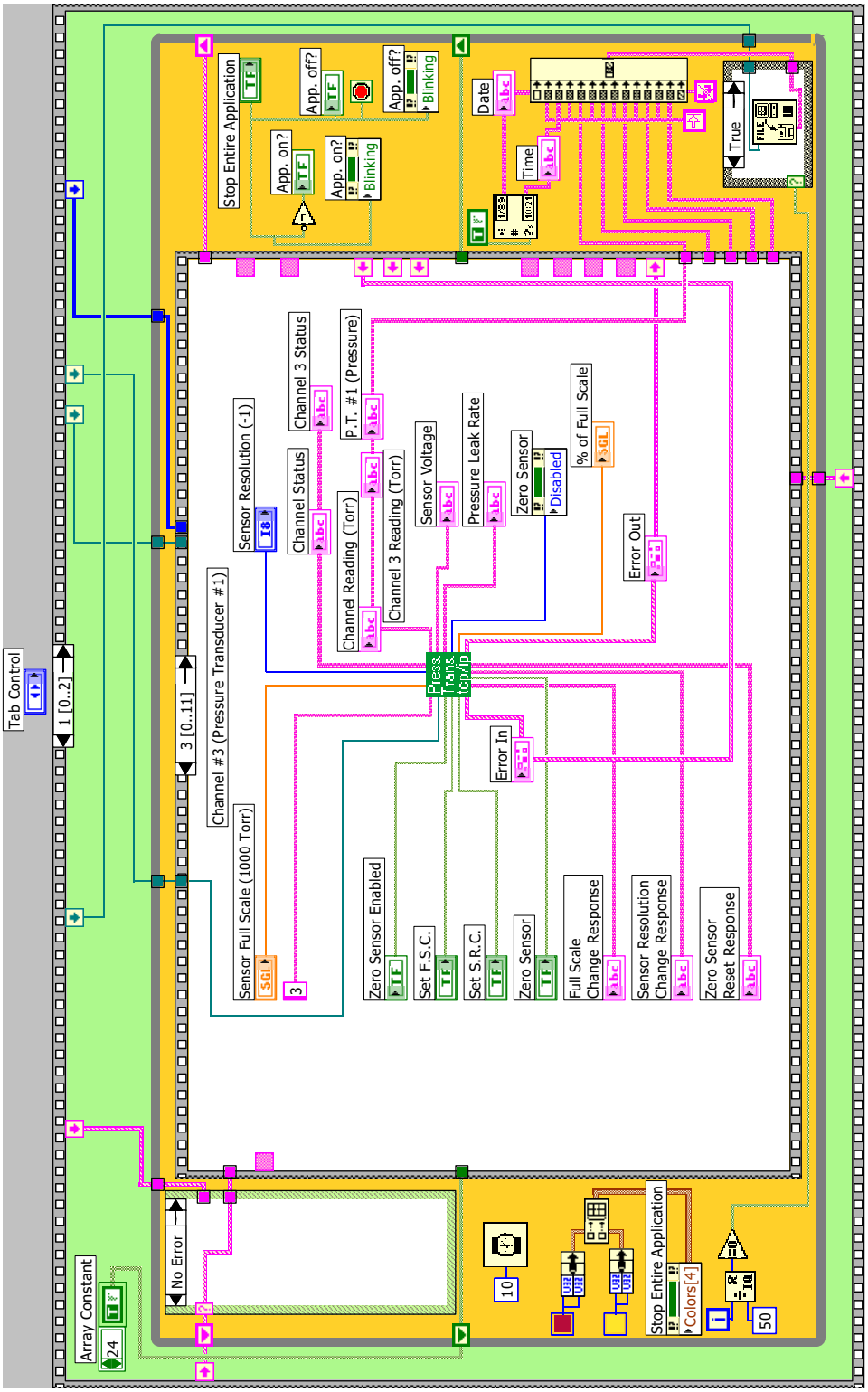

Figure A.3: An example of the unique LabView "G" graphical programming language. This is the code associated with Fig. A.2. The green box in the middle is the subroutine common to all of the pressure transducers.

Appendix B

Lab Frame 2-Body Relativistic Kinematics

B.1 Introduction

The purpose of this appendix is two fold. First, it is intended to document some of the necessary calculations that were made in support of the measurements detailed in the body of this thesis. Secondly, it was necessary to ensure proper calculation of the kinematics since many programs provide inconsistent results. The software package *Mathematica* was chosen as the computational medium due to its breadth, depth, graphics, accessibility and familiarity to those who may read this work in the future.

B.2 Kinematic Equations

The calculation of two-body kinematics, Fig. B.1, is a strait forward exercise in algebra. Therefore, only the equations solved and their solution will be shown. The equations describing a relativistic inelastic collision in the lab frame are:

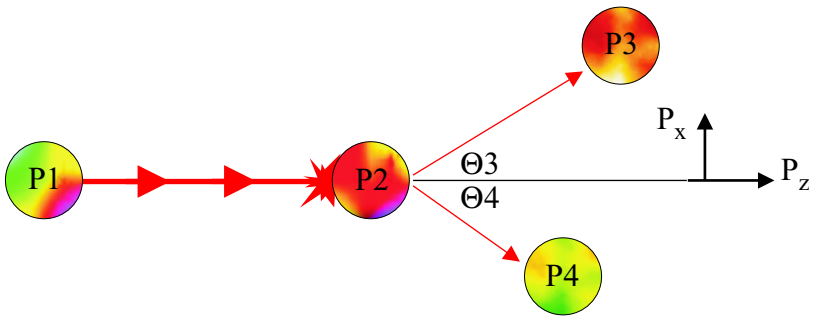

Figure B.1: Cartoon diagram of two-body collision. $P1$ represents incoming projectile, $P2$ is the target, whereas $P3$ and $P4$ are the resulting fragments after collision. $\Theta_{3,4}$ are the angles with respect to P_z of $P_{3,4}$ respectively.

Conservation of Energy:

$$E_{Total} = E1 + E2 = E3 + E4 \tag{B.1}$$

where

$$E_i{}^2 = P_i{}^2 + M_i{}^2 \text{ for } i = 1, 3, 4 \tag{B.2}$$

and

$$E_2 = m_2 \text{ (target at rest)} \tag{B.3}$$

Conservation of Momentum:

$$x : 0 = P_3 Sin(\Theta_3) - P_4 Sin(\Theta_4) \tag{B.4}$$

and

$$z : P_1 = P_3 Cos(\Theta_3) + P_4 Cos(\Theta_4) \tag{B.5}$$

Now, solving equations B.1, B.4 and B.5 for P_3 as a function of Θ_3 we find:

$$P_3^{\pm}(\Theta_3) = \frac{-\frac{B(\Theta_3)}{A(\Theta_3)} \pm \sqrt{(\frac{B(\Theta_3)}{A(\Theta_3)})^2 - \frac{4D}{A(\Theta_3)}}}{2} \tag{B.6}$$

Cell Style	Font Type	Font Size
Title	Arial	12 Point
Section	Arial	12 Point
Text	Times New Roman	12 Point
Input	Courier	12 Point
Output	Courier New	12 Point

Table B.1: *Mathematica* notebook cell style conventions.

where

$$A(\Theta_3) = 4(E^2 - P_1^2 Cos^2(\Theta_3) \tag{B.7}$$

$$B(\Theta_3) = -(4CP_1 Cos(\Theta_3)) \tag{B.8}$$

$$C = E^2 + M_3^2 - M_4^2 - P_1^2 \tag{B.9}$$

$$D = 4E^2 M_3^2 - C^2 \tag{B.10}$$

As P_3 is related to P_4 by equation B.1, we also know P_4 as a function of Θ_3. Alternatively, one may use equations B.4 and B.5 as we are given P_1.

B.3 Mathematic Notebook: Lab System 2-body Relativistic Kinematics & S800 Bρ Calculator

B.3.1 Introduction

The subsection B.3.2 that follows contains a *Mathematica* notebook that has only been altered from its original state so as to meet the formatting requirements of this document. Therefore, reproducing the notebook should be strait forward and relatively painless. Following standard *Mathematica* conventions the following Table B.1 shows the font conventions for the various kinds of cells used in the notebooks.

The notebook contains an example calculation of the p(^{34}Ar,d)^{33}Ar in inverse kinematics. In this example the target, a proton, is at rest and the projectile, ^{34}Ar

has a kinetic energy of approximately $84 MeV/u$.

B.3.2 Notebook

■ Lab System 2-body Relativistic Kinematics & S800 Bρ Calculator:

■ Lab Frame Quantities (Variable Definitions):

e1-projectile energy
e2-target energy (rest mass)
e3-reaction product energy
(Note: #3 -or- the "reaction product" will be the ion assumed to be measured in the focal plane)
e4-second reaction product energy
(Note:e#p stands for e#plus& e#m stands for e#minus)
etot-total energy
p1-projectile momentum
p2-target (p2=0; i.e. stationary target)
p3-reaction product momentum
p4-second reaction product momentum
m1-projectile mass
m2-target mass
m3-reaction product mass
m4-second reaction product mass
a3-reaction product scattering angle
a4-second reaction product scattering angle
z3-charge of reaction product
z4-charge of second reaction product
k1-projectile kinetic energy in MeV/u
q-"Q-value" in MeV
rho-central bend radius of S800 spectrometer
rhob-bend radius of bottom of D1
rho4-bend radius of second reaction product
r=rho4

(Note: all distances are in meters)

Units:[e]=MeV

[p]=MeV/c

[m]=amu

[a]=radians

[u]=MeV/c^2

[bd3]=T

- **Calculations:**

```
(* Clear Variables *)
ClearAll[e1, e2, e3p, e3m, e4p, e4m, bbeam]
ClearAll[p1, p2, p3, p4, p3p, p3m, p4p, p4m]
ClearAll[m1, m2, m3, m4, mbeam, pbeam, rhobeamm, rhobeamp]
ClearAll[a3, a4, z3, z4, zbeam, rho3m, rho4m, rhob, rhot]
ClearAll[k1, k3p, k3m, b3p, b3m, u, etot, q, rho]
ClearAll[a, b, c, d, bd3m, bd3p, rho3p, rho4p]
rho = 2.8028;
rhob = rho + 0.3524;
rhot = rho - 0.3524;
u  = 931.49432;
(* Constants for Momentum Calculation *)
a = etot^2 + (m3 * u)^2 - (m4 * u)^2 - p1^2;
b[a3_] = 4 * (etot^2 - p1^2 * Cos[a3]^2);
c[a3_] = -4 * a * p1 * Cos[a3];
d = 4 * etot^2 * (m3 * u)^2 - a^2;
(* Reaction Products Momentum Formulas *)
```

$$p3p[a3\_] = \frac{-c[a3]}{2 * b[a3]} + \sqrt{\left(\frac{c[a3]}{2 * b[a3]}\right)^2 - \frac{d}{b[a3]}};$$

$$p3m[a3\_] = \frac{-c[a3]}{2 * b[a3]} - \sqrt{\left(\frac{c[a3]}{2 * b[a3]}\right)^2 - \frac{d}{b[a3]}};$$

```
(* Initial Momentum and Energy *)
```

$$p1 = \sqrt{(k1 * m1)^2 + 2 * (k1 * m1) * (m1 * u)};$$

$$pbeam = \sqrt{((k1 * mbeam)^2 + 2 * (k1 * mbeam) * (mbeam * u))};$$

$$e1 = \sqrt{p1^2 + (m1 * u)^2};$$

$$etot = e1 + (m2 * u);$$

(* Energy and Momentum Calculations *)

$$e3p[a3\_] = \sqrt{p3p[a3]^2 + (m3 * u)^2};$$

$$e3m[a3\_] = \sqrt{p3m[a3]^2 + (m3 * u)^2};$$

$$e4p[a3\_] = etot - e3p[a3];$$

$$e4m[a3\_] = etot - e3m[a3];$$

$$k3p[a3\_] = e3p[a3] - (m3 * u);$$

$$k3m[a3\_] = e3m[a3] - (m3 * u);$$

$$k4p[a3\_] = e4p[a3] - (m4 * u);$$

$$k4m[a3\_] = e4m[a3] - (m4 * u);$$

$$p4p[a3\_] = \sqrt{(k4p[a3])^2 + 2 * (k4p[a3]) * (m4 * u)};$$

$$p4m[a3\_] = \sqrt{(k4m[a3])^2 + 2 * (k4m[a3]) * (m4 * u)};$$

(* β' s *)

$$bbeam = \sqrt{1 - \left(\frac{m1 * u}{e1}\right)^2};$$

$$b3m[a3\_] = p3m[a3] / e3m[a3];$$

$$b3p[a3\_] = p3p[a3] / e3p[a3];$$

$$b4m[a3\_] = \sqrt{1 - ((m4 * u) / e4m[a3])^2};$$

$$b4p[a3\_] = \sqrt{1 - ((m4 * u) / e4p[a3])^2};$$

(* Q-value *)

$$q = (m1 + m2 - m3 - m4) * u;$$

(* Magnetic Field and Bend Radius *)

$$bd3m[a3\_] = 3.3356 \frac{(p3m[a3] * 0.001)}{z3 * rho};$$

$$bd4m[a3\_] = 3.3356 \frac{(p4m[a3] * 0.001)}{z4 * rho};$$

$$\text{rhobeamm}[a3\_] = 3.3356 * \frac{\text{pbeam} * 0.001}{\text{bd3m}[a3] * \text{zbeam}};$$

$$\text{rho4m}[a3\_] = 3.3356 * \frac{\text{p4m}[a3] * 0.001}{\text{bd3m}[a3] * z4};$$

$$\text{rho3m}[a3\_] = 3.3356 * \frac{\text{p3m}[a3] * 0.001}{\text{bd3m}[a3] * z3};$$

$$\text{bd3p}[a3\_] = 3.3356 \frac{(\text{p3p}[a3] * 0.001)}{z3 * \text{rho}};$$

$$\text{bd4p}[a3\_] = 3.3356 \frac{(\text{p4p}[a3] * 0.001)}{z4 * \text{rho}};$$

$$\text{rhobeamp}[a3\_] = 3.3356 * \frac{\text{pbeam} * 0.001}{\text{bd3p}[a3] * \text{zbeam}};$$

$$\text{rho4p}[a3\_] = 3.3356 * \frac{\text{p4p}[a3] * 0.001}{\text{bd3p}[a3] * z4};$$

$$\text{rho3p}[a3\_] = 3.3356 * \frac{\text{p3p}[a3] * 0.001}{\text{bd3p}[a3] * z3};$$

- **Ar34 + p -> d + Ar33 (Ar33 in Focal Plane):**

```
(* Set Initial Conditions *)
ClearAll[k1, m1, m2, m3, m4, z3, z4, r, zbeam, mbeam, exen4]
exen3 = 0.0;
(* Excitation energy of reaction product 2 in MeV*)
k1 = 83.7547;
m1 = 33.980270118; (* Ar34 *)
```

```
mbeam = m1;
m2 = 1.007825032; (* H1 *)
m3 = 32.989928719; (* Ar33 *)
m3 = m3 + exen3 / u;
z3 = 18;
m4 = 2.014101778; (* H2 *)
z4 = 1;
zbeam = z3;
rm = rho4m[0];
rp = rho4p[0];
Print["Reaction Q-value: ", q, " MeV"]
Print["Beam Energy: ", k1, " MeV/u"]
Print["Solution 1 Bend Radius of Beam: ",
 rhobeamp[0], " m"]
Print["Solution 2 Bend Radius of Beam: ",
 rhobeamm[0], " m"]
Print["Beta of Beam: ", bbeam, " v/c"]
Print["Solution 1:"]
Print["     Kinetic Energy of Reaction
   Product @ Lab Angle = 0: ", k3p[0] / m3, " MeV/u"]
Print["     Magnetic Field Setting of S800: ",
 bd3p[0], " Tesla"]
Print["     Bρ = ", bd3p[0] * rho, " Tm"]
Print["     β[0] = ", b3p[0], " v/c"]
Print[
 "     Momentum of Reaction Product @ Lab Angle = 0: ",
 p3p[0] * 0.001, " GeV/c"]
Print["     Kinetic Energy of Reaction Product 2: ",
 k4p[0], " MeV"]
Print["     Bend Radius of Reaction Product 2: ρRP #2 = ",
 rp, " m"]
Print["     β[0] = ", b4p[0], " v/c"]
Print["     Momentum of Reaction Product 2: ",
 p4p[0] * 0.001, " GeV/c"]
TableForm[Table[{i, k3p[i (π/180)] / m3}, {i, 0, 2}],
```

```
 TableHeadings → {None,
   {"Lab Angle", "Kinetic Energy of Reaction Product"}}]
Print["Solution 2:"]
Print["     Kinetic Energy of Reaction
   Product @ Lab Angle = 0: ", k3m[0] / m3, " MeV/u"]
Print["     Magnetic Field Setting of S800: ",
 bd3m[0], " Tesla"]
Print["     Bρ = ", bd3m[0] * rho, " Tm"]
Print["     β[0] = ", b3m[0], " v/c"]
Print[
 "     Momentum of Reaction Product @ Lab Angle = 0: ",
 p3m[0] * 0.001, " GeV/c"]
Print["     Kinetic Energy of Reaction Product 2: ",
 k4m[0], " MeV"]
Print["     Bend Radius of Reaction Product 2: ρRP#2 = ",
 rm, " m"]
Print["     β[0] = ", b4m[0], " v/c"]
Print["     Momentum of Reaction Product 2: ",
 p4m[0] * 0.001, " GeV/c"]
TableForm[Table[{i, k3m[i (π/180)] / m3}, {i, 0, 2}],
 TableHeadings → {None,
   {"Lab Angle", "Kinetic Energy of Reaction Product"}}]
```

```
Reaction Q-value: -14.8437 MeV

Beam Energy: 83.7547 MeV/u

Solution 1 Bend Radius of Beam: 2.86164 m

Solution 2 Bend Radius of Beam: 3.10781 m

Beta of Beam: 0.397728 v/c

Solution 1:

     Kinetic Energy of Reaction Product @ Lab Angle = 0:
 85.1795 MeV/u

     Magnetic Field Setting of S800: 0.888529 Tesla
```

Bρ = 2.49037 Tm

β[0] = 0.400681 v/c

Momentum of Reaction Product @ Lab Angle = 0: 13.4389 GeV/c

Kinetic Energy of Reaction Product 2: 21.0972 MeV

Bend Radius of Reaction Product 2: $\rho_{RP\#2}$ = 1.0592 m

β[0] = 0.148716 v/c

Momentum of Reaction Product 2: 0.282147 GeV/c

Lab Angle	Kinetic Energy of Reaction Product
0	85.1795
1	84.4273
2	81.1941

Solution 2:

Kinetic Energy of Reaction Product @ Lab Angle = 0: 72.6863 MeV/u

Magnetic Field Setting of S800: 0.81815 Tesla

Bρ = 2.29311 Tm

β[0] = 0.373534 v/c

Momentum of Reaction Product @ Lab Angle = 0: 12.3744 GeV/c

Kinetic Energy of Reaction Product 2: 433.249 MeV

Bend Radius of Reaction Product 2: $\rho_{RP\#2}$ = 5.49014 m

β[0] = 0.583107 v/c

Momentum of Reaction Product 2: 1.34661 GeV/c

Lab Angle	Kinetic Energy of Reaction Product
0	72.6863
1	73.3299
2	76.2377

Appendix C

Glossary

Alfven radius The radial distance from a star where the magnetic field energy density becomes comparable to the kinetic energy density of infalling matter.

α-process These processes include the reactions in which α particles are successively added to ^{20}Ne. The source of α particles is different for this process than for Helium burning [10].

AGB Asymptotic Giant Branch. A late stage, post main sequence, of stellar evolution characterized by periodic helium shell flashes.

Baryons Baryons are half integer spin particles comprised of quarks. The lightest two baryons in order of increasing mass are the proton and neutron [73].

Core Center region of a star. There are several types:

[Convective Core] Convection dominated energy transport.

[Radiative Core] Radiation dominated energy transport.

Cosmic Ray High energy radiation of astrophysical origin. Charged particle energies can exceed 10^{20} eV [74]. Cosmic rays are frequently positively charged light nuclei. However, nuclei as heavy as Uranium have been detected.

CRDC The Cathode Readout Drift Chamber or CRDC is a gas filled charged particle detector. The CRDC is a member of a more general class of gas detectors known as drift chambers. In the focal planes of the S800 Spectrometer and Sweeper Magnet the CRDCs are filled with a mixture of 20% CF_4 and 80% iC_4H_{10} and are operated at a pressure of approximately 50 Torr.

Dark Matter Unseen, i.e. dark, mass, in the sense of gravitation, responsible for observed otherwise unexplainable galactic properties.

GK GigaKelvin. This unit is frequently denoted by T_9.

Hot CNO Cycle The hot carbon nitrogen oxygen cycle [3] (HCNO):

$$^{14}O(e^+,\nu)^{14}N(p,\gamma)^{15}O(e^+,\nu)^{15}N(p,\alpha)^{12}C(p,\gamma)^{13}N(p,\gamma)^{14}O. \tag{C.1}$$

The HCNO cycle is also known as the β-limited, due to the e^+ decay lifetimes of $^{14,15}O$, cycle. Temperatures range $0.2 \leq T_9 \leq 0.5\ GK$.

Ion Chamber The Ion Chamber or IC is a gas filled charged particle detector. The IC is a member of a more general class of gas detectors known as proportional counters (see CRDC). The purpose of the IC is to measure the energy loss of the particle as it streams through the gas. This energy loss is frequently used for particle identification. In the focal planes of the S800 Spectrometer and Sweeper Magnet at the NSCL the IC is filled with a premixed gas known as P10, a mixture of 10% CH_4 and 90% Ar, at pressures in the 100 to 300 Torr range.

Neutron Capture The general category of nucleosynthesis by neutron capture. Neutron capture has two dominant stellar processes associated with it:

[r process] Process of neutron capture on a relatively short timescale [10]. The timescale is measured relative to the β decay rate because the neutron

captures must happen faster than the competing β decays. Typical timescales for r process neutron capture reactions are: $lower \leq t \leq upper$.

[s process] The slow neutron capture process. This neutron capture process is slow relative to β decay. Typical timescales for neutron captures range from 100 years to 10^5 years.

Neutron Star The neutron rich remnants of a massive star that has exploded. Typical mass and radius for a neutron star are 1.3 Solar Mass and 10 km respectively. As neutron stars exist as macroscopic nuclear matter they are very interesting natural laboratories for nuclear physics studies. [75]

Nuclear Electronics The physical electronic devices used for nuclear physics experiments needed to process inputs from detectors and other equipment.

Nucleogenesis See *Nucleosynthesis*

Nucleosynthesis The creation of larger mass nuclei by reactions with other nuclei and particles in an astrophysical environment.

pp-chain The sequence of reactions that is the dominant source of energy in stellar burning. This process of is composed of three cycles [1].

p-process A candidate for the origin of neutron-deficient stable isotopes of the elements heavier than ^{74}Se and lighter than ^{196}Hg [76].

rp **process** The rapid proton capture process. This process is characterized by explosive hydrogen burning at temperatures in excess of 10^8 K. This process is responsible for the production of many neutron deficient nuclei between ^{19}Ne, the break out of the HCNO cycle [3] and ^{107}Te, the endpoint of the *rp* process in the Sn-Sb-Te cycle [15].

Spallation The ejection of a series of individual nucleons or small groups of nucleons during a nuclear reaction with typical bombarding energies greater than 100 MeV/u [77].

Supernovae A very energetic stellar explosion. Supernovae come in several varieties. There are two main types: Type I and Type II. Type I supernovae are characterized by a lack of prominent Hydrogen lines in their spectra, whereas Type II supernovae do have Hydrogen lines in their spectra [11].

[Type Ia] Spectra show a strong Si II line at 6150 Å.

[Type Ib] Spectra show strong presence of Helium lines.

[Type Ic] Spectra have an absence of Helium lines.

[Type IIL (linear) or P (plateau)] Spectra show strong Hydrogen lines. The linear, L, and plateau, P, classification describe the shape of their corresponding light curves.

Bibliography

[1] C.E. Rolfs and W.S. Rodney. *Cauldrons in the Cosmos*. University of Chicago Press, 1988.

[2] A. Kong et al. *Mon. Not. Royal Astronomy Society*, 311:405, 2000.

[3] R.K. Wallace and S.E. Woosley. Explosive hydrogen burning. *The Astrophysical Journal Supplement Series*, 45:389–420, 1980.

[4] G. Audi and A.H. Wapstra. *Nuclear Physics A*, 595:409, 1995.

[5] B.E. Tomlin et al. *Physical Review C*, 63(034314), 2001.

[6] B.A. Brown. Private communication, 2003.

[7] F. Herfurth, J. Dilling, A. Kellerbauer, G. Audi, D. Beck, G. Bollen, H.-J. Kluge, D. Lunney, R.B. Moore, C. Scheidenberger, S. Schwarz, G. Sikler, J. Szerypo, and ISOLDE Collaboration. Breakdown of the isobaric multiplet mass equation at A = 33, T = $\frac{3}{2}$. *Physical Review Letters*, 87(14):1–4, 2001.

[8] D.N. Schramm and M.S. Turner. Big-bang nucleosynthesis enters the precision era. *Reviews of Modern Physics*, pages 303–318, January 1998.

[9] D.N. Spergel *et. al.* Determination of cosmological parameters. 2003. Submitted.

[10] E.M. Burbidge, G.R. Burbidge, W.A. Fowler, and F. Hoyle. Synthesis of the elements in stars. *Reviews of Modern Physics*, 29(4):547–650, October 1957.

[11] B.W Carroll and D.A. Ostlie. *An Introduction To Modern Astrophysics*. Addison-Wesley Publishing Company, Inc., 1st edition, 1996.

[12] J.J. Cowan, F.K. Thilemann, and J.W. Truran. The r-process and nucleochronology. *Physics Reports*, (4 & 5):269–388, November 1991.

[13] H. Schatz, A. Aprahamian, J. Gorres, M. Wiescher, T. Rauscher, J.F. Rembges, F.K. Thielemann, B. Pfeiffer, P. Moller, K.L. Kratz, H. Herndl, B.A. Brown, and H. Rebel. rp-process nucleosynthesis at extreme temperature and density conditions. *Physics Reports*, 294:167–263, 1998.

[14] B.Davids, A.M. van den Berg, P. Dendooven, F. Fleurot, M. Hunyadi, M.A. de Huu, K.E. Rehm, R.E. Segal, R.H. Siemssen, H.W. Wilschut, H.J. Wortche, and A.H. Wuosmaa. α-decay branching ratios of near-threshold states in ^{19}ne and the astrophysical rate of $^{15}o(\alpha,\gamma)^{19}ne$. *Physical Review C*, 67(012801):1–4, 2003.

[15] H. Schatz, A. Aprahamian, V. Barnard, L. Bildsten, A. Cumming, M. Ouellette, T. Rauscher, F.K. Thieleman, and M. Wiescher. End point of the *rp* process on accreting neutron stars. *Physical Review Letters*, 86(16):3471–3474, 2001.

[16] B.A. Brown, R.R.C. Clement, H. Schatz, W.A. Richter, and A. Volya. Proton drip-line calculations and the *rp* process. *Physical Review C*, 65(045802):1–12, 2002.

[17] L. Van Wormer et al. *The Astrophysical Journal*, 432:326, 1994.

[18] H. Schatz, L. Bildsten, A. Cumming, and M. Wiescher. *The Astrophysical Journal*, 524:1014, 1999.

[19] O. Koike, M. Hashimoto, K. Arai, and S. Wanojo. *Astronomy and Astrophysics*, 324:464, 1999.

[20] B.A. Brown. *Physical Review C*, 42(R1513), 1993.

[21] W.E. Ormand. *Physical Review C*, 53:214, 1996.

[22] W.E. Ormand. *Physical Review C*, 55:2407, 1997.

[23] B.J. Cole. *Physical Review C*, 54:1240, 1996.

[24] B.A. Brown. *Physical Review*, 58:220, 1998.

[25] B.A. Brown, W.A. Richter, and R. Lindsay. *Phys. Lett. B*, 483:49, 2000.

[26] A. Volya, B.A. Brown, and V. Zelvinsky. *Phys. Lett. B*, 509:37, 2001.

[27] W.A. Richter, M.G. van der Merwe, R.E. Julies, and B.A. Brown. *Nuclear Physics A*, 523:325, 1991.

[28] M. Hjorth-Jensen, T.T.S. Kuo, and E. Osnes. *Physics Reports*, 261:125, 1995.

[29] S. Raman, C.W. Nestor, and P. Tikkanen. *At. Data and Nucl. Data Tables*, 2001.

[30] B. Blank et al. *Physical Review Letters*, 74:4611, 1995.

[31] J. Winger et al. *Phys. Lett. B*, 299:214, 1993.

[32] J. D. Robertson et al. *Physical Review C*, 42(4611), 1990.

[33] R. Pfaff et al. *Physical Review C*, 53(1753), 1996.

[34] M. F. Mohar et al. *Physical Review Letters*, 66(1571), 1991.

[35] A. Jokinen et al. *Z. Phys. A*, 355:227, 1996.

[36] Z. Janas et al. *Physical Review Letters*, 82:295, 1999.

[37] L. Bildsten. *The Many Faces of Neutron Stars*. A. Alpar and L. Bucceri and J. Van Paradijs, 1997.

[38] P. Möller, W.D. Myers, and J.R. Nic. *At. Data and Nucl. Data Tables*, 59, 1995.

[39] E. Kuulkers et al. *Astronomy and Astrophysics*, 2001.

[40] L. Bildsten. Rossi 2000: Astrophysics with the rossi x-ray timing explorer. Technical report, NASA's Goddard Space Flight Center, 2000.

[41] M. Rayet et al. *Astronomy and Astrophysics*, 298:517, 1995.

[42] V. Costa et al. *Astronomy and Astrophysics*, 358:L67, 2000.

[43] M. Jaeger et al. *Physical Review Letters*, 87(202501), 2001.

[44] P.G. Hansen and J.A. Tostevin. Direct reactions with exotic nuclei. *Annual Review of Nuclear and Particle Science*, 53, 2003. MSUCL-1258.

[45] W.F. Mueller, J.A. Church, T. Glasmacher, D. Gutknecht, G. Hackman, P.G. Hansen, Z. Hu, K.L. Miller, and P. Quirin. Thirty-two-fold segmented germanium detectors to identify γ rays from intermediate-energy exotic beams. *NIMA*, 466:492–498, July 2001.

[46] K.L. Miller, T. Glasmacher, C. Campbell, L. Morris, W.F. Mueller, and E. Strahler. Automated determination of segment positions in a high-purity 32-fold segmented germanium detector. *NIMA*, 490:140–145, May 2002.

[47] Z. Hu, T. Glasmacher, W.F. Mueller, and I. Wiedenhöver. An automatic energy-calibration method for segmented germanium detectors. *NIMA*, 482:715–719, April 2002.

[48] D. Radford *et. al.* *GF3: Interactive graphical analysis of gamma-ray coincidence data.* Physics Division at Oak Ridge National Laboratory. http://radware.phy.ornl.gov/main.html.

[49] W. Meuller. Private communication, 2003.

[50] H. Olliver. Private communication, 2003.

[51] J. Yurkon, D. Bazin, W. Benenson, D.J. Morrissey, B.M. Sherrill, D. Swan, and R. Swanson. Focal plane detector for the s800 high-resolution spectrometer. *Nuc. Inst. & Meth. in Phys. Res.*, 422:291–295, 1999.

[52] J.A. Caggiano. *SPECTROSCOPY OF EXOTIC NUCLEI WITH THE S800 SPECTROGRAPH*. Experimental nuclear physics, Michigan State University, 1995.

[53] M. Berz *et. al.* Cosy infinity users guide and reference manual, version 7. Technical report, Michigan State University National Superconducting Cyclotron Laboratory, 1995. MSUCL-977.

[54] M Berz, K. Joh, J.A. Nolen, B.M. Sherrill, and A.F. Zeller. Reconstructive correction of aberrations in nuclear particle spectrographs. *Phys. Rev. C*, 47:537–544, 1993.

[55] R. Fox *et. al.*, editor. *Real-Time results without Real-Time Systems*, Montreal, Canada, May 2003. Michigan State University's National Superconducting Cyclotron Laborator. 2003 IEEE Conference on Real-Time Computer Applications in Nuclear, Particle and Plasma Physics.

[56] Ousterhout. *The Tcl and Tk Toolkit*. Addison-Wesley Publishing Company, 1st edition, 1994.

[57] H. Nann, W. Benenson, E. Kashy, and P. Turek. Isobaric mass quartets in A = 33 nuclei. *Physical Review C*, 9(5):1848–1850, 1974.

[58] W. Benenson and E. Kashy. Isobaric quartets in nuclei. *Reviews of Modern Physics*, 51(3):527–539, 1979.

[59] Evaluated nuclear structure data file. http://www.nndc.bnl.gov/nndc/ensdf.

[60] M.C. Pyle, A. Garcia, E. Tatar, J. Cox, B.K. Nayak, S. Triambak, B. Laughman, A. Komives, L.O. Lamm, J.E. Rolon, T. Finnessy, L.D. Knutson, and P.A. Voytas. Revalidation of the isobaric multiplet mass equation. *Physical Review Letters*, 88(12):122501:1–4, 2002.

[61] H. Herndl, B. Brown, J. Görres, M. Wieschrer, and L. Van Wormer. Proton capture reaction rates in the *rp* process. *Physical Review C*, 52(2), August 1995.

[62] D. Arnett. *Supernovae and Nucleosynthesis*. Princeton University Press, 1996.

[63] C.I. Freigang. Building the sweeper magnet focal plane detector. Master's thesis, Michigan State University, August 2001.

[64] MKS Instruments. *MKS Type 1179A and 2179A Mass-Flo Controller and Type 179A Mass-Flo Meter*, rev e, 3/99 edition, March 1999. Instruction Manual 116527-P1.

[65] MKS Instruments. *MKS Type 740B/750B/742B/752B, Ultraclean 840B/850B/842B/852B, Baratron Pressure Transducers and R700/R800 Series Relay Systems*, rev d, 11/98 edition, November 1998. Instruction Manual 117802-P1.

[66] MKS Instruments. *MKS Type 186B Process Controller*, rev a, 1/99 edition, January 1999. Instruction Manual 121406-P1.

[67] MKS Instruments. *MKS Type 260 PS-3B Power Supply*, rev c, 11/99 edition, November 1999. Instruction Manual 108196-P1.

[68] National Instruments. *Getting Started with LabVIEW*, July 2000. Part Number 321527D-01.

[69] National Instruments. *User Manual*, July 2000. Part Number 320999C-01.

[70] National Instruments. *Measurement Manual*, July 2000. Part Number 322661A-01.

[71] G.W. Johnson and R. Jennings. *LabVIEW Graphical Programming*. McGraw-Hill, 3rd edition, 2001.

[72] B. Mihura. *LabVIEW FOR DATA ACQUISITION*. Prentice Hall PTR (National Instruments virtual instrumentation series), 1st edition, 2001.

[73] S.S.M. Wong. *INTRODUCTORY Nuclear Physics*. JOHN WILEY & SONS, INC., 2nd edition, 1998.

[74] D.J. Bird, S.C. Corbato, H.Y. Dai, J.W. Elbert, K.D. Green, M.A. Huang, D.B. Kieda, S. Ko, E.C. Loh C.G. Larsen, M.Z. Luo, M.H. Salamon, J.D. Smith, P. Sokolsky, P. Sommers, J.K.K. Tang, and S.B. Thomas. Detection of a cosmic ray with measured energy well beyond the expected spectral cutoff due to cosmic micrwave radiation. *The Astrophysical Journal*, 441:144–150, 1994.

[75] Opportunities in nuclear astrophysics. Technical report, Joint Insititute for Nuclear Astrophysics and Michigan State University and University of Notre Dame, 1999.

[76] R.D. Hoffman, S.E. Woosley, G.M. Fuller, and B.S. Meyer. Production of the light p-process nuclei in neutrino-driven winds. *The Astrophysical Journal*, 460:478–488, March 1996.

[77] G.R. Satchler. *Introduction to Nuclear Reactions*. Oxford University Press, 2nd edition, 1990.